POLITECNICO
MILANO 1863

SCUOLA DI INGEGNERIA INDUSTRIALE
E DELL'INFORMAZIONE

Executive Summary of the Thesis

Kinetic modeling of the pyrolysis and oxidation of oxymethylene ethers

Laurea Magistrale in Chemical Engineering - Ingegneria Chimica

Author: Alessandro Pegurri

Advisor: Prof. Alessandro Stagni

Co-advisor: Prof. Tiziano Faravelli

Academic year: 2020-2021

1. Introduction

Climate change is one of the biggest challenges that humanity has to face today and, in order to keep the global warming below 1.5°C and limit the environmental damage, reaching net zero carbon emissions by 2050 is crucial. To accomplish this goal and reduce the dependence on fossil fuels, the adoption of renewable energies must be intensified, but carbon-free energy sources are intermittent by nature and hence not completely reliable. A solution would be the use of synthetic fuels, or e-fuels, which could act as storage for excess energy to be released at need.

Oxymethylene ethers (OMEs), a class of synthetic oxygenated fuels with molecular structure $CH_3O[CH_2O]_nCH_3$, have been identified as suitable additives or surrogates for traditional diesel fuels and are becoming a relevant research topic. The main reasons for this appeal are:

- their physico-chemical properties are similar to the ones of diesel fuels;
- their synthesis processes are well established;
- their content of oxygen leads to the reduction of NO_x and soot formation.

As a consequence, the interest for the chemical kinetics of the OMEs has been rapidly growing, and more detailed models are becoming available. Dimethyl ether (DME, OME_0) and dimethoxymethane (DMM, OME_1) are small enough to allow theoretical calculations for their rate constants estimation, while for heavier homologues the mechanisms rely on analogies with alkanes or smaller ethers, or are based on optimizations on experimental datasets. A comprehensive mechanism for $OME_{0–4}$ has been recently developed by Cai et al. [1], adopting the DMM mechanism by Jacobs et al. [2] as reference for a reaction-class based methodology, and subsequently optimizing some pre-exponential factors to refine the agreement with the experimental data.

The major drawback of adopting a detailed mechanism to describe the combustion of OMEs is the high numbers of species and reactions involved, which increase more than linearly with the fuel chain length. Therefore, detailed kinetic models cannot be applied to heavy large-scale simulations without the computational times to become unsustainable, and reduction techniques need to be applied. Fortunately the regular structure and hierarchical nature of OMEs make them very suitable for a lumped formulation of their kinetics and, moreover, an eventual downstream optimization of the reaction parameters is easier to perform on a reduced mechanism than on a full sized one.

In this Thesis, a kinetic mechanism of the pyrolysis and oxidation of $OME_{0–4}$ has been obtained combining a novel automatic lumping procedure and a data-driven mechanism optimization. The intermediate isomers in the OMEs decomposition paths are grouped together in order to lump a detailed model built from state-of-the-art sub-mechanisms available in literature. The intermediate lumped kinetics is then optimized, minimizing the objective function that quantifies the differences between the simulations and the experiments, and the final mechanism is validated against the other models and the experimental data.

2. Methodology

2.1. Model construction

The model describing the $OME_{0–4}$ pyrolysis and oxidation was assembled applying a hierarchical and modular procedure, progressively adding sub-mechanisms to the CRECK kinetic framework, adopted as core. Ethers chemistry was included starting from a DME low-to-high temperature kinetics, on top of which the DMM sub-mechanism by Jacobs et al. [2] and the $OME_{2–4}$ sub-mechanisms by Cai et al. [1] were integrated. The final detailed mechanism counts 282 species and 2657 reactions.

2.2. Chemical lumping

The chemical lumping procedure was separately performed on each OME sub-mechanism, adopting a Master Equation Lumping (MEL, available at `https://github.com/lpratalimaffei/MEL`) methodology [3] and adjusting it for the purpose of this Thesis. MEL was initially conceived to simplify the complexity of the output of multi-well master equation simulations, grouping species with similar chemical behaviour and treating implicitly the reactivity of unstable intermediates. The methodology was therefore adapted and, for the first time, successfully applied to the chemical lumping of a detailed kinetic model. The developed procedure is the following:

1. once identified the structural isomers, the pseudospecies that group them are defined;
2. the complete detailed mechanism is divided into blocks characterized by reactions with the same global stoichiometry;
3. the equilibrium reactions of the detailed model are split into forward and backward ones;
4. zero-dimensional isothermal and isobaric simulations are performed to evaluate the compositions of each pseudospecies;
5. the reactions parameters for each block are calculated and the lumped OME sub-mechanism is assembled.

The zero-dimensional isothermal and isobaric simulations were carried out in order to account for the intrinsic interconnections between blocks, and evaluate the Branching Fractions (BFs) of the isomers in a consistent way. The chosen temperature interval (T = 500–2000 K) is wide enough to ensure reliability in most conditions of interest, while $\Phi = 0.5$ was selected to emphasize low-temperature oxidation kinetics, and $P = 20$ bar as a good representative value for the experimental range (P = 1–40 bar).

The average, temperature-dependent BFs were then calculated from the simulation results. In particular, BF_i of each i^{th} isomer in a pseudospecies was determined according to Equation (1):

$$BF_i = \frac{\int_0^{t_{max}} X_i(t)dt}{t_{max}} \tag{1}$$

in which X_i is the i^{th} isomer fraction in the total isomers pool, defined in Equation (2):

$$X_i(t) = \frac{x_i(t)}{\sum_i^{N_S} x_i(t)} \tag{2}$$

where x_i is the mole fraction of the i^{th} isomer and N_S the total number of species in the pool. In Equation (1), t_{max} is the time of the simulation when the maximum mole fraction of total isomers is reached, after which it rapidly drops to zero because of the oxidation ending.

The lumped reaction parameters were calculated with MEL, treating separately each mechanism block. The procedure consists in reducing an ODE system that describes the evolution of the initial set of species to an equivalent lumped system, and is extensively discussed in [3]. The BFs previously evaluated are used as initial conditions to solve the initial system and find the concentration profiles produced by each pseudospecies.

The only reactions whose lumped parameters were evaluated manually were the ones

yielding more than two products. The lumped rate constants in these cases were derived as in Equation (3):

$$k(T)_{L\to P} = \sum_i BF(T)_i \cdot k(T)_{i\to P} \qquad (3)$$

where $i \to P$ represents the reaction of the i^{th} isomer to the set of products P, whereas $L \to P$ indicates the lumped reaction. The obtained values of $k(T)_{L\to P}$ were finally fitted in a modified Arrhenius expression.

2.3. Data-driven optimization

As final step, the lumped model underwent an optimization procedure in order to improve the simulations-experiments agreement. The methodology proposed by Bertolino et al. [4] was implemented using the `OptiSMOKE++` toolbox and applied for the first time to a lumped mechanism. The modified Arrhenius parameters of the rates of the most relevant reaction, identified via sensitivity analysis, are optimized by exploiting an evolutionary algorithm. One of the major advantages of the approach is the possibility to optimize pressure-dependent reactions (in PLOG format) without losing their physical consistency. This was particularly useful for the DMM sub-mechanism, in which various pressure-dependent rates are present [2].

For each of the selected reactions, an uncertainty factor $f = 0.3$ was assumed; this was a conservative choice since it is the lowest value among those reviewed by Bertolino et al. [4]. The corresponding maximum variation of the optimized reaction rates is of a factor ∼2 with respect to their nominal values. For the purpose of this Thesis, all the considered reactions were independently optimized, regardless of their reaction class.

The objective function to minimize is based on a Curve Matching (CM) index [5] that assesses the differences between the simulations and the experiments: after converting both into functional data, the shapes of their curves and those of their first derivatives are compared using an extended L^2-norm and the Pearson coefficients. This way, the model-experiments agreement is clearly quantified and the CM indices can be employed to evaluate the performances of the mechanisms in the several cases analyzed.

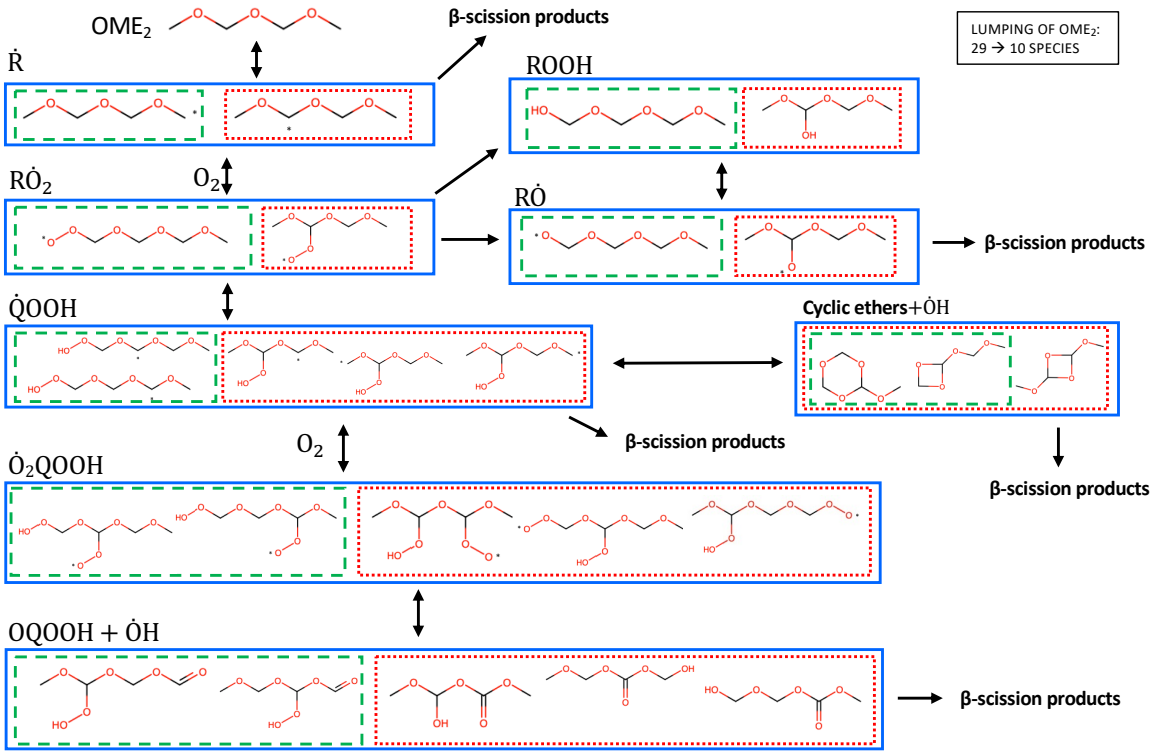

Figure 1: Schematic representation of OME_2 kinetics. Green/dashed and red/dotted lines highlight intermediate species originated respectively by primary and secondary radicals. Lumped isomers are grouped by blue rectangles.

3. Results and discussion

3.1. Mechanism lumping

The lumping procedure performed on OME_2, starting from the detailed kinetic mechanism of Cai et al. [1], is reported in Figure 1 as example for the method adopted for all OMEs. All the species involved in the low-temperature oxidation can be identified, already grouped into pseudospecies: OME_2 alkyl ($\dot{R}$), alkoxy ($R\dot{O}$), peroxy ($R\dot{O}_2$), hydroperoxy-alkyl ($\dot{Q}OOH$), and hydroperoxy-alkyl-peroxy ($\dot{O}_2QOOH$) radicals, hydroperoxides (ROOH), cyclic ethers and keto-hydroperoxides (OQOOH). The advantage of using a lumped scheme in terms of number of species and reactions is clear: not only the initial 29 isomers have been grouped into 10 pseudospecies, but also the multi-branched chemistry is now described by more linear pathways.

Reaction type	N. of blocks	Species before/ after lumping	Reactions before/ after lumping
H-abstraction	11	3/2	4/2
$\dot{R}$ decomposition	1	5/4	8/6
$R\dot{O}$ formation	2	4/2	2/1
$\dot{R}+O_2$	1	12/4	24/6
ROOH formation	3	4/2	4/2
$R\dot{O}$ decomposition	1	6/6	5/4
$\dot{Q}OOH+O_2$	1	20/4	15/3

Table 1: OME_2 blocks of reactions with the same global stoichiometry, grouped by reaction type.

Table 1 summarizes the mechanism blocks identified for OME_2, divided by reaction type. Within the same reaction type the blocks differ in the starting reactants, such as the abstractors in the H-abstraction type. The lumping procedure was performed on each block, according to the BFs derived from Equation (1).

The overall process resulted in a significant reduction of the mechanism size in terms of both reactions and species, as depicted in Figure 2. Starting from the DME sub-mechanism, the detailed description of the combustion of the OME_{1-4} requires 156 species, while the lumped formulation only needs 50. The lumped OME_{1-4} mechanism counts a total of 176 species and 2486 reactions.

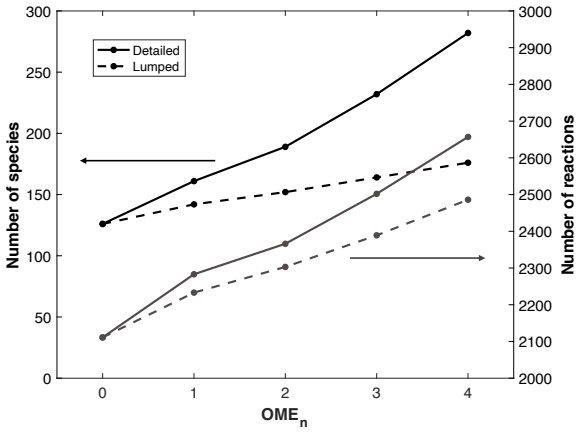

Figure 2: Comparison between detailed and lumped mechanisms number of species (black/left) and reactions (grey/right).

3.2. Reactions selection

The selection of the reactions to be optimized was performed evaluating their local sensitivity coefficients, normalized with respect to their maximum, along the whole range of operating conditions. The coefficients were calculated from the lumped mechanism for each dataset, according to the variable of interest.

For the Ignition Delay Time (IDT) zero-dimensional simulations, the sensitivity analyses were performed on the $\dot{O}H$ molar fraction, at the temperature corresponding to the inflection point of the ignition curve. Three different characteristic times were selected for each temperature, in order to cover for low-, intermediate- and high-temperature kinetics. An example for OME_2 can be seen in Figure 3a; the sensitivity coefficients, shown in Figure 3b, highlight the promoting role of the OME_2 radicals and the inhibiting effect of the decomposition of OME_2 $\dot{Q}OOH$ to the more stable DMM ketones.

Jet Stirred Reactor (JSR) speciation was investigated via sensitivity analyses carried out on the fuel concentration at lean ($\Phi = 0.25$), stoichiometric ($\Phi = 1$) and rich ($\Phi = 2$) conditions. For each, three temperatures were chosen, corresponding to local minimum, maximum and inflection point after the negative temperature coefficient region.

Finally, the Laminar Flame Speed (LFS) controlling reactions were identified with a mass flow sensitivity analysis at three representative equivalence ratios: one corresponding to the maximum burning velocity ($\Phi \simeq 1.2$), one

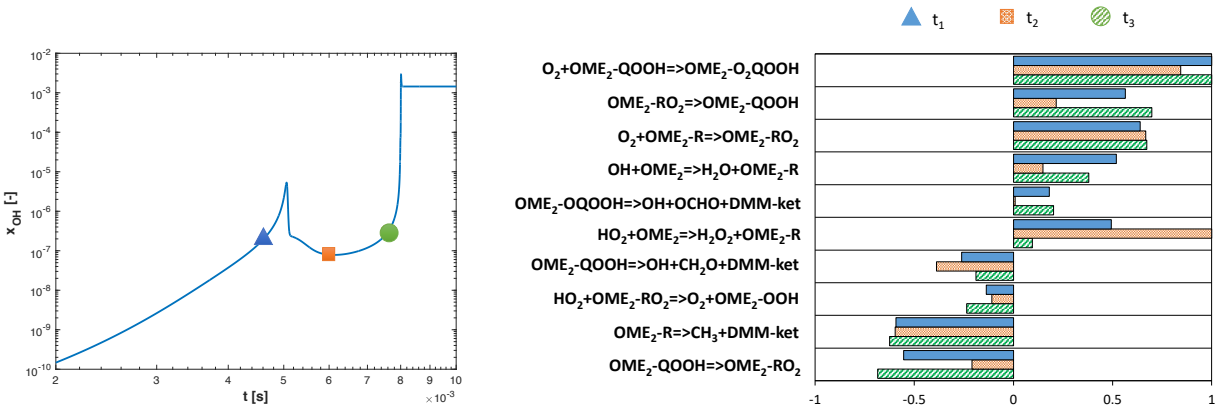

(a) ȮH molar fraction profile and selected characteristic times.

(b) Normalized sensitivity coefficients to ȮH mass fraction of the 10 most sensitive reactions for the selected times.

Figure 3: ȮH molar fraction profile in a zero-dimensional IDT simulation for OME_2 at $P = 9$ bar and $T = 660$ K with characteristic times. Also the 10 most sensitive reactions of the OME_2 sub-mechanism and their normalized sensitivity coefficients are reported.

higher ($\Phi \simeq 1.6$) and one lower ($\Phi \simeq 0.9$).

After the analyses were completed, from the resulting reactions those belonging to the DME and C_1-C_3 sub-mechanisms were excluded. Since their parameters had not been modified in the lumping operation, avoiding to optimize them ensures that the original consistency of these sub-mechanism is preserved. From the remaining reactions, all belonging to the $OME_{1–4}$ sub-mechanisms, the first ten from each simulation, for a total of 57, were selected to be optimized.

3.3. Mechanism validation

All mechanisms were finally validated against a wide range of experiments, including IDTs in STs, speciations in JSRs and Plug Flow Reactors, and LFSs. The capabilities of detailed, lumped and optimized mechanisms in predicting $OME_{2–4}$/air stoichiometric IDTs are compared in Figure 4 for the data measured by Cai et al. [1] at $P = 10 - 20$ bar. The detailed model reasonably agrees with the experiments in all cases, with the best results for OME_4. The lumping process brought about a general increase of the mechanism reactivity, with a maximum deviation from the detailed model of a factor ∼3; for this, the predictions of the lumped model for the reported cases improved for OME_2 while worsened for $OME_{3–4}$. The optimization of the lumped model resulted in a significant enhancement of the results for all OMEs: the experimental data are reproduced similarly to, or even better than, the detailed mechanism.

Fuel	Average Curve Matching index		
	Detailed	Lumped	Optimized
DMM	0.906	0.894	0.911
OME_2	0.893	0.913	0.908
OME_3	0.843	0.818	0.848
OME_4	0.907	0.823	0.929
$OME_{1–4}$	0.892	0.881	0.902

Table 2: Average Curve Matching indices of the adopted mechanisms for each OME.

Table 2 collects the average CM scores [5] of the mechanisms for each OME, considering the experimental database available. This index allows to precisely quantify the model-experiment agreement, providing for each comparison a univocal score between 0 (complete disagrement) and 1 (maximum agreement). The optimized kinetics outperforms in every case the detailed model and the lumped mechanism, with the only exception of OME_2.

4. Conclusions

In this Thesis a new methodology has been developed, successfully coupling the lumping of structural isomers with a data-driven optimization procedure, to obtain a reliable reduced kinetic model for $OME_{0–4}$. To build the de-

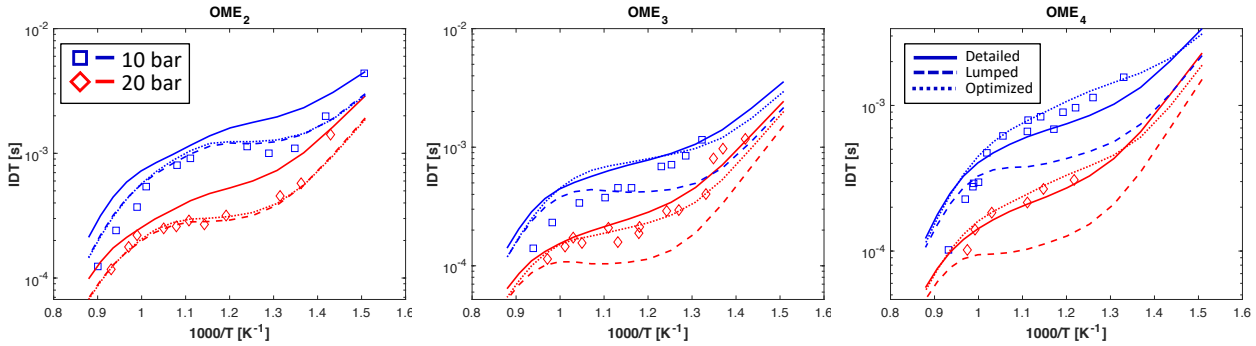

Figure 4: IDTs measured in a ST by Cai et al. [1] for $OME_{2–4}$, together with modeling predictions.

tailed kinetics, the hierarchical approach was exploited, meaning that each new sub-mechanism was added to the others in a modular way.

The detailed model was lumped adopting and adjusting a recent procedure (MEL) [3] based on the Master Equation, which was applied on each $OME_{1–4}$ sub-mechanism separately, in line with the hierarchy principle. The species were grouped into pseudospecies according to structural isomerism, greatly reducing their final number from 282 to 176.

As a final step, an optimization procedure that exploits evolutionary algorithms [4] was performed on the lumped mechanism. The optimization targets were selected from a large database of experimental results and, via sensitivity analysis, a total of 57 reactions to optimize was identified.

All the mechanisms were validated against 84 experimental datasets, covering a wide range of reactors and operating conditions. The CM indices [5] quantitatively confirm that the developed workflow was successful: the optimized model recovered most of the accuracy lost in the chemical lumping, while saving 106 species with respect to the detailed mechanism.

After this first application of the lumping-optimization coupling on the OME chemistry, the next step is a more systematic and efficient modeling of long-chain fuels. Future research will involve the implementation of methodologies for hierarchical lumping and optimization procedures based on reaction classes.

References

[1] Liming Cai, Sascha Jacobs, Raymond Langer, Florian vom Lehn, Karl Alexander Heufer, and Heinz Pitsch. Auto-ignition of oxymethylene ethers (omen, n= 2–4) as promising synthetic e-fuels from renewable electricity: shock tube experiments and automatic mechanism generation. *Fuel*, 264:116711, 2020.

[2] Sascha Jacobs, Malte Döntgen, Awad BS Alquaity, Wassja A Kopp, Leif C Kröger, Ultan Burke, Heinz Pitsch, Kai Leonhard, Henry J Curran, and K Alexander Heufer. Detailed kinetic modeling of dimethoxymethane. part ii: Experimental and theoretical study of the kinetics and reaction mechanism. *Combustion and Flame*, 205:522–533, 2019.

[3] Luna Pratali Maffei, Matteo Pelucchi, Carlo Cavallotti, Andrea Bertolino, and Tiziano Faravelli. Master equation lumping for multi-well potential energy surfaces: a bridge between ab initio based rate constant calculations and large kinetic mechanisms. *Chemical Engineering Journal*, 422:129954, 2021.

[4] Andrea Bertolino, Magnus Fürst, Alessandro Stagni, Alessio Frassoldati, Matteo Pelucchi, C Cavallotti, T Faravelli, and Alessandro Parente. An evolutionary, data-driven approach for mechanism optimization: theory and application to ammonia combustion. *Combustion and Flame*, 229:111366, 2021.

[5] Matteo Pelucchi, Alessandro Stagni, and Tiziano Faravelli. Addressing the complexity of combustion kinetics: Data management and automatic model validation. In *Computer Aided Chemical Engineering*, volume 45, pages 763–798. Elsevier, 2019.

POLITECNICO
MILANO 1863

SCUOLA DI INGEGNERIA INDUSTRIALE
E DELL'INFORMAZIONE

Kinetic modeling of the pyrolysis and oxidation of oxymethylene ethers

Tesi di Laurea Magistrale in
Chemical Engineering - Ingegneria Chimica

Author: **Alessandro Pegurri**

Student ID: 944665
Advisor: Prof. Alessandro Stagni
Co-advisor: Prof. Tiziano Faravelli
Academic Year: 2020-2021

Ai miei nonni, a mio padre,
soprattutto a mia madre

"It's the job that's never started as takes longest to finish."
-Samwise Gamgee

(J. R. R. Tolkien, *The Lord of the Rings - The Fellowship of the Ring*, 1954)

Ringraziamenti

Per prima cosa tengo a ringraziare il prof. Stagni, che in qualità di relatore mi ha seguito dai primi passi nel mondo della ricerca fino alla stesura di questa Tesi; ogni consiglio è stato prezioso e le opportunità che mi sono state date hanno contribuito in maniera decisiva alla mia crescita. Vorrei ringraziare anche tutti i membri del gruppo CRECK per il tempo che mi hanno dedicato. Tra loro soprattutto l'ing. Pratali Maffei per le dritte fondamentali e il prof. Faravelli per la fiducia data e la determinazione trasmessa. Sono infinitamente grato anche al prof. Hasse che mi ha ospitato presso il gruppo di ricerca STFS a Darmstadt. Grazie all'ing. Ferraro e a tutte le persone con cui ho collaborato durante la mia permanenza in Germania, che hanno contribuito a trasmettermi la passione e l'interesse fondamentali per proseguire.

Un enorme grazie va alla mia famiglia. Grazie papà per avermi permesso di essere qui oggi, appoggiando ogni mia scelta e credendo in me; mi hai sempre dato tutto senza chiedere nulla e spero di poterti restituire tanto, iniziando con questo risultato. Grazie nonni per avermi incoraggiato ogni giorno: nei vostri occhi ho visto sempre e solo orgoglio, e non ho mai potuto fare altro che impegnarmi al massimo per continuare a meritarlo. E grazie mamma, questa soddisfazione è anche tua.

Grazie a tutti gli amici che mi hanno regalato parte del loro tempo in questi anni universitari, di cui questo giorno è il culmine. Grazie Fil per tutti i bei momenti di studio e quelli bellissimi di non studio: senza di te avrei faticato il doppio e ora mi mancherebbe un grande amico. Grazie Luc, amico e coinquilino, e grazie a chiunque abbia intrecciato il proprio percorso con il mio: c'é un po' anche di voi in questo lavoro. E un grandissimo grazie va ovviamente ai Panini; ogni serata che abbiamo condiviso mi ha sempre permesso di tornare a lavorare con più carica. Sono sicuro che la vostra amicizia continuerà ad essere parte della mia vita come in questi bellissimi anni.

Infine vorrei ringraziare la mia ragazza Alessia, che mi sta accanto ogni giorno, ispirandomi e supportando ogni mia decisione con il sorriso. Hai sempre la parola giusta al momento giusto per farmi proseguire, anche quando non ne vedo nessuna ragione. Questo non sarebbe stato possibile senza di te, e tutto sarebbe un po' più noioso. Grazie.

Publications and Conferences

Publications

- Alessandro Pegurri, Andrea Bertolino, Luna Pratali Maffei, Alessandro Parente, Tiziano Faravelli, and Alessandro Stagni. Coupling chemical lumping to data-driven optimization for the kinetic modeling of oxymethylene ethers ($OME_{1–4}$) combustion. *Proceedings of the Combustion Institute,* 2022, under review.

Conferences

- Alessandro Pegurri, and Alessandro Stagni. Oxymethylene ethers as the next-generation energy carriers: kinetic model development. In *Convegno GRICU 2022,* Ischia, Italy, 03 July - 06 July 2022.
- Timoteo Dinelli, Edoardo Ramalli, Alessandro Pegurri, Barbara Pernici, Tiziano Faravelli, and Alessandro Stagni. From detailed kinetics to large-scale simulations: integrating data ecosystems in the skeletal reduction framework. In *18^{th} International Conference on Numerical Combustion,* San Diego, CA United States of America, 08 May - 11 May 2022.

Abstract

Oxymethylene ethers (OMEs) are a class of oxygenated synthetic fuels, which are recently gaining interest because of their applications as diesel additives. As a matter of fact, it has been observed that, adopting a proper blend of diesel and OMEs, the soot and NO_x emissions are noticeably reduced while the performances are maintained, without major modifications to the engines needed. In order to further study the possible future applications of OMEs in the transportation sector, a kinetic model of their combustion is necessary. The high number of species included in its oxidation and decomposition paths, though, makes unfeasible to use a detailed mechanism for demanding tasks, such as Computational Fluid Dynamics simulations. In this Thesis, a kinetic mechanism describing the combustion of OMEs has been obtained through a new methodology, and subsequently optimized to better represent the experimental data available.

An automatic chemical lumping procedure has been developed and successfully applied to the $OME_{0–4}$ detailed chemistry, obtained by merging different sub-mechanisms available in the literature. The approach consists in grouping structural isomers into pseudospecies, and considering their relative reactivity in order to lump their reaction paths accordingly. In this way, the number of species only increases linearly with the fuel chain length, at the cost of minor accuracy losses. The lumped model was then optimized by minimizing the differences between its predictions and the experimental results, quantitatively expressed by a Curve Matching objective function. The optimization was performed on the parameters of the modified Arrhenius expressions of the controlling reactions, identified via sensitivity analyses carried out over the whole range of operating conditions and reactors. An uncertainty factor of about 2 was accounted for all the reaction rates optimized.

The described approach proved remarkably effective in treating the OME initial mechanism of 282 species, producing a reduced model counting 176 species. Not only the final kinetics is more compact saving more than 100 species, but behaves similarly to, and frequently even better than, the detailed model in the majority of the cases studied. The properties considered are Ignition Delay Times in Shock Tubes, speciations in Jet Stirred and Plug Flow Reactors, and Laminar Flame Speeds, evaluated in a wide range

of temperatures, pressures and equivalence ratios. After this first successful result, the methodology here developed could be applied to heavier fuels, with even higher computational advantages expected.

Keywords: Oxymethilene ethers, OME, energy carriers, detailed kinetics, chemical lumping, data-driven optimization.

Sommario

Gli eteri ossimetilenici (OME) sono una classe di carburanti ossigenati sintetici, che stanno recentemente guadagnando interesse per via delle loro applicazioni come additivi per il diesel. È stato infatti osservato che, utilizzando la corretta miscela di diesel e OME, le emissioni di particolato e NO_x vengono notevolmente ridotte mentre le prestazioni rimangono invariate, senza bisogno di modificare eccessivamente il motore. Per studiare ulteriormente le possibili future applicazioni degli OME nel settore dei trasporti, è necessario un modello cinetico della loro combusione. L'elevato numero di specie coinvolte nei loro cammini di decomposizione e ossidazione, tuttavia, rende impossibile l'utilizzo di un meccanismo dettagliato per lavori pesanti, come simulazioni di Fluidodinamica Computazionale. In questa Tesi, attraverso una nuova metodologia, è stato ottenuto un meccanismo cinetico che descrive la combustione degli OME, e successivamente ottimizzato per rappresentare meglio i dati sperimentali disponibili.

Una procedura automatica di lumping chimico è stata sviluppata e applicata con successo alla chimica dettagliata degli $OME_{0–4}$, ottenuta unendo diversi sub-meccanismi disponibili in letteratura. L'approccio consiste nel raggruppare gli isomeri strutturali in pseudospecie, e considerare la loro reattività relativa per lumpare di conseguenza i loro percorsi di reazione. In questo modo il numero di specie cresce solo linearmente con la lunghezza della catena del combustibile, al costo di minori perdite in accuratezza. Il modello lumpato è stato quindi ottimizzato minimizzando le differenze tra le sue previsioni e i risultati sperimentali, espresse quantitativamente da una funzione obiettivo Curve Matching. L'ottimizzazione è stata eseguita sui parametri delle espressioni Arrhenius modificate delle reazioni controllanti, individuate da analisi di sensitività svolte sull'intero spettro di condizioni operative e reattori. È stato considerato un fattore di incertezza di circa 2 per ogni velocità di reazione ottimizzata.

L'approccio descritto si è rivelato particolarmente efficace nel trattare il meccanismo iniziale OME di 282 specie, producendo un modello ridotto che ne conta 176. Non solo la cinetica finale è più compatta risparmiando più di 100 specie, ma si comporta in maniera simile, e spesso anche migliore, del modello dettagliato nella maggioranza dei casi studiati. Le proprietà considerate sono Tempi di Ignizione in Shock Tubes, speciazioni in reattori

Jet Stirred e Plug Flow, e Velocità di Fiamma Laminari in un ampio intervallo di temperature, pressioni e rapporti di equivalenza. Dopo questo primo risultato di successo, la metodologia qui sviluppata potrà essere applicata a carburanti più pesanti, con vantaggi computazionali attesi ancora maggiori.

Parole chiave: Eteri ossimetilenici, OME, vettori energetici, cinetica dettagliata, lumping chimico, ottimizzazione.

Contents

List of Figures

List of Tables

List of Symbols and Acronyms

Symbols

Variable	Description	SI unit
A	Pre-exponential factor	$\mathrm{mol/m^3/s}$
$\boldsymbol{c}$	Concentrations vector	$\mathrm{mol/m^3}$
E_a	Activation energy	J/mol
f	Uncertainty factor	-
$\tilde{H}_i$	Specific enthalpy	J/mol
$\boldsymbol{K}$	Kinetic constants matrix	$(\mathrm{mol/m^3})^{(1-n)}/\mathrm{s}$
K^e	Equilibrium constant	-
k	Kinetic constant	$(\mathrm{mol/m^3})^{(1-n)}/\mathrm{s}$
P	Pressure	Pa
R	Universal gas constant	J/mol/K
$\tilde{S}_i^{\,0}$	Specific entropy	J/mol/K
s	Sensitivity coefficient	-
T	Temperature	K
t	Time	s
X	Isomer fraction	-
x	Mole fraction	-
β	Exponential factor	-
$\Delta\tilde{H}$	Reaction enthalpy	J/mol
$\Delta\tilde{S}^0$	Reaction entropy	J/mol/K
λ	Air-fuel equivalence ratio	-
ν	Stoichiometric coefficient	-
σ	Standard deviation	-
Φ	Fuel-air equivalence ratio	-

Acronyms

Acronym	Full form
BF	Branching Fraction
CM	Curve Matching
CFD	Computational Fluyd Dynamics
PAH	Polyaromatic Hydrocarbons
DME	Dimethil Ether
DMM	Dimethoxymethane
GHG	Greenhouse Gases
ICE	Internal Combustion Engine
IDT	Ignition Delay Time
JSR	Jet Stirred Reactor
MEL	Master Equation Lumping
NTC	Negative Temperature Coefficient
OME	Oxymethylene Ether
PFR	Plug Flow Reactor
RCM	Rapid Compression Machine
ST	Shock Tube

1 | Introduction

Today, climate change is one of the most pressing issues that humanity has to face [1], as it has recently been reminded by the 2021 United Nations Climate Change Conference (commonly referred to as COP26). At the conference, which took place in Glasgow (Scotland) from 31^{th} October to 12^{th} November 2021, it was stressed that every country should reach net zero carbon emissions by 2050 in order to keep global worming under 1.5°C and limit the environmental damage [2]. Scientific research, together with regulation policies and changes of individual behaviours, inevitably plays a fundamental role in this difficult challenge.

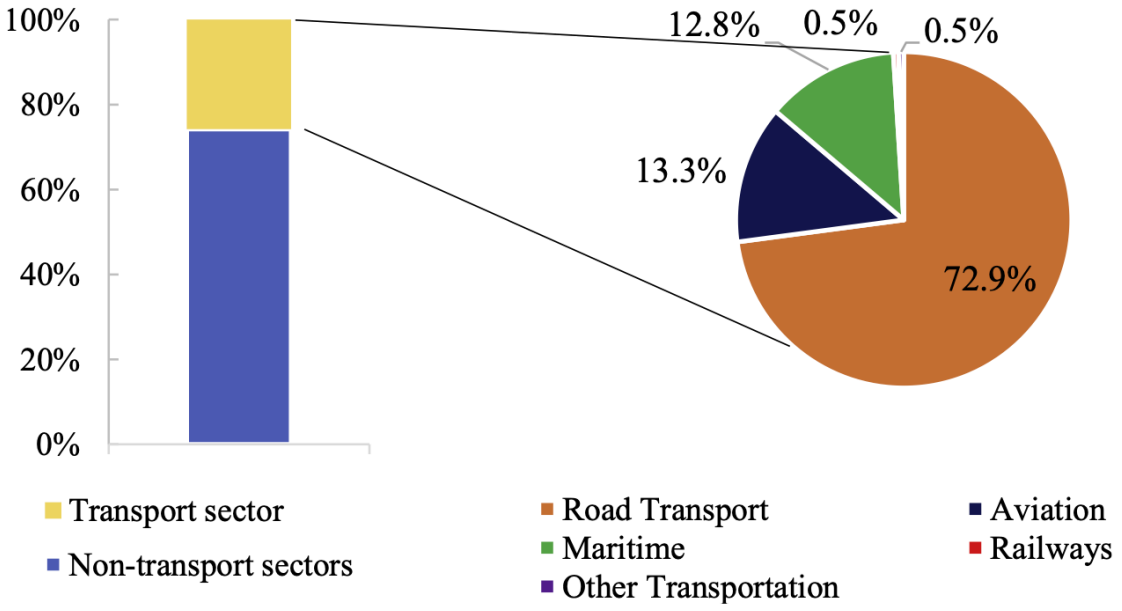

Figure 1.1: GHG emissions in Europe in 2017, from transportation and non-transportation sector by sources [3].

The transportation sector is among the most impactful, not only contributing to global warming with greenhouse gases (GHGs) emissions (Figure 1.1), but also being a major source of local pollutants, such as nitrogen oxides (NO_x) and particulate (soot) [3, 4]. In Europe, the transportation sector produces about 23% of GHGs and 46% of

NO_x [5], and the reduction of these emissions is at the moment an important research topic. The current trend seems to be completely oriented towards electric vehicles which, despite being a promising long term solution, still present important open problems. For example, the lithium battery disposal is an issue that needs to be carefully addressed [6], and the increased load on the electric infrastructures cannot be ignored. Moreover, as shown in Figure 1.2, about 63% of electricity produced globally in 2019 came from fuel combustion [7], thus making it an energy source still far from being completely green.

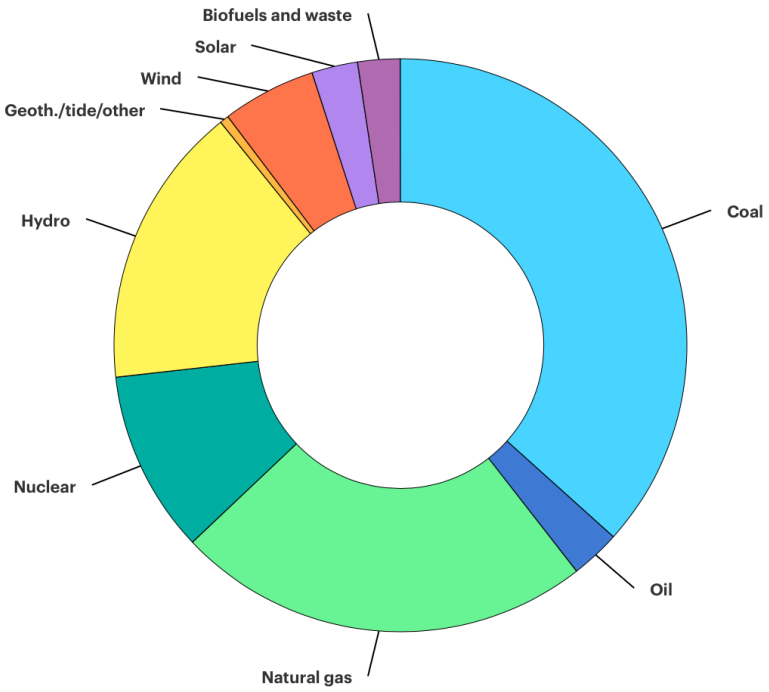

Figure 1.2: Global electricity sources in 2019 [7].

It is then inevitable that for the most part of the 21^{st} century combustion will still cover an important role both as a direct fuel and as an electricity source (Figure 1.3). Despite the efforts and impressive results, renewable energy will not be able to cover even 50% of the total demand [7], which is expected to rise also because of the demographic and economical growth of the new global powers. During this period of transition, it is crucial to find ways to limit the impact that combustion has on the environment, both improving the efficiency of Internal Combustion Engines (ICEs) and reducing emissions with better fuels.

One of the investigated paths is the use of alternative fuels, which, especially in the transportation sector, would substitute or integrate the traditional ones derived from oil,

such as gasoline and diesel. The main advantage of these fuels would be reduced emissions, but it is worth to mention also that some could be synthesized indirectly from the CO_2 captured from air, further decreasing their overall carbon impact. Moreover, synthetic fuels (e-fuels), could act as storage for renewable energy, which is by nature intermittent and not continuous. It is the case of the fuel class known as oxymethylene ethers (OMEs), which shows good combustion properties; for this reasons a lot of research is being done in order to use them in ICEs as diesel surrogates or additives [8].

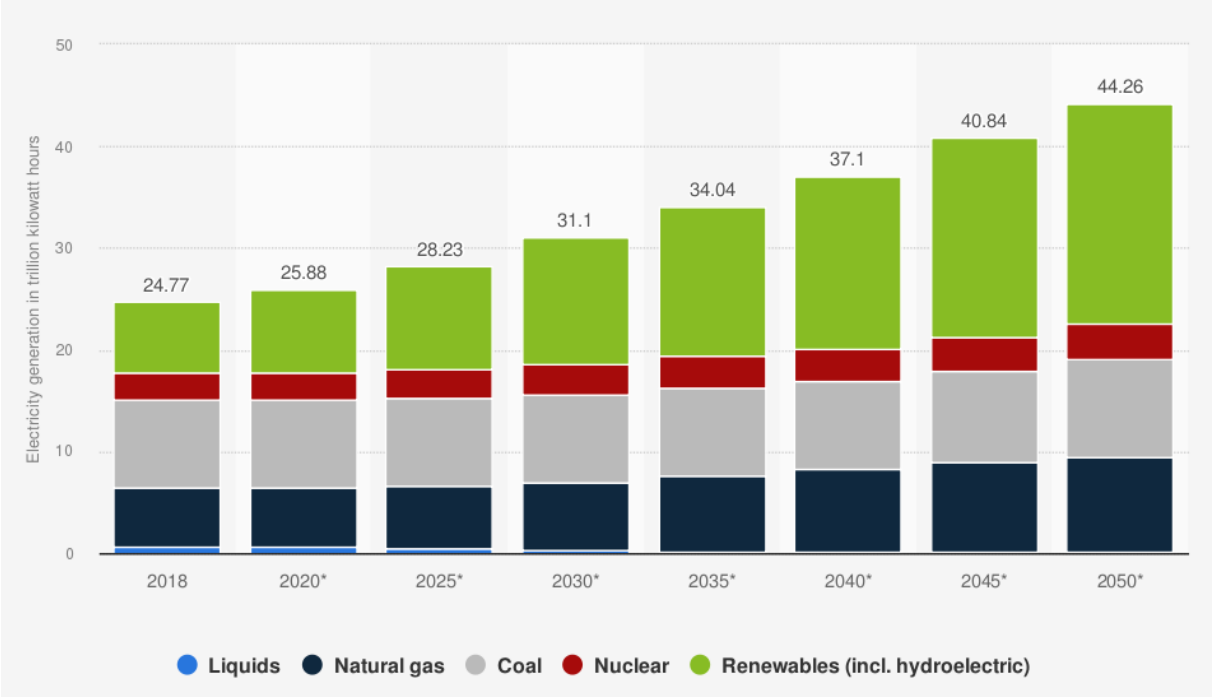

Figure 1.3: Expected sources of electricity in the first half of the 21^{st} century [9].

1.1. Oxymethilene ethers

OMEs are a class of oxygenated fuels with general structure $CH_3O[CH_2O]_nCH_3$. The subscript n indicates the number of CH_2O groups present and the corresponding molecule is referred to as OME_n. The simplest is dimethyl ether (DME, OME_0) with $n = 0$, followed by dimethoxymethane (DMM, OME_1) with $n = 1$, and higher OMEs, as shown in Figure 1.4. They have gained a lot of interest from the scientific community over the past years for different reasons, such as:

- their physico-chemical properties are similar to the ones of diesel fuels, allowing them to be burned in standard, or slightly modified, diesel engines [10];
- their synthesis processes are well established and use common and low cost reactants;

in addition, some routes involve captured CO_2 and renewable electricity, increasing the overall sustainability;

- their content of oxygen leads to NO_x and particulate formation reduction, as shown by several experimental [8, 11, 12] and numerical [13–15] studies.

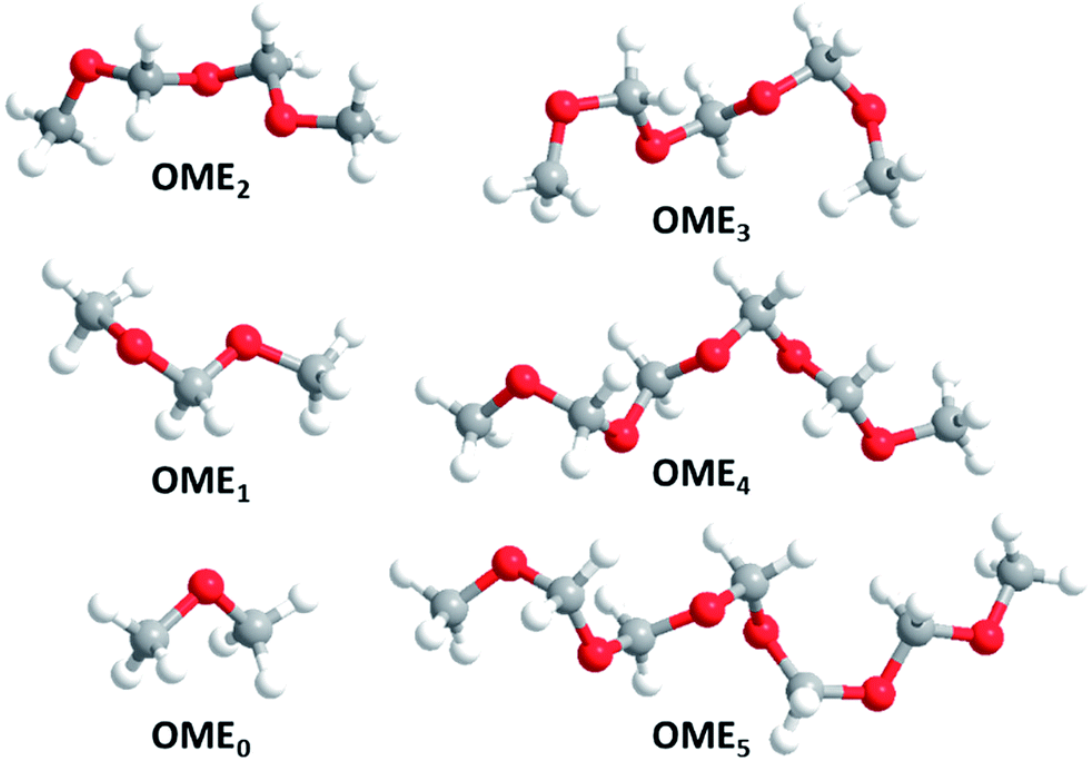

Figure 1.4: Graphical representation of $OME_{0–5}$. Carbon is grey, oxygen red and hydrogen white [16].

The addition of DME in diesel fuel is known to reduce soot and NO_x formation [17], but it also lowers the viscosity, increases the vapor pressure and may reduce solubility at low temperatures [18, 19]. This would require some modifications to the traditional diesel engines. DMM also has good potential as additive, but experiments show that engines still require some adjustments [20]. Higher OMEs ($n = 2–5$), if the correct blend is chosen, can be instead added to diesel without modifying the engine infrastructure [21] and they are hence the main research target.

1.1.1. Properties

Table 1.1 summarizes the key physico-chemical properties of OMEs and conventional diesel fuel. As already said, DME and DMM cannot be used in current diesel engines as they are but, because of their lower viscosities and boiling point, they require alterations

to the fuel supply system. On the other hand, heavier OMEs seem suitable to be used with the current configuration. Furthermore, contrary to DME, they do not present a miscibility gap with diesel at temperatures below 0°C [18]. Finally, because of their lower vapor pressures, they do not need to be stored in pressurized tanks, which makes a great advantage in terms of handling and safety.

	CDF	DME	DMM	OME_2	OME_3	OME_4
Melting point [°C]	/	-141	-105	-70	-43	-10
Boiling point [°C]	170-390	-25	42	105	156	201
Viscosity (25°C)[mPa s]	2.71	/	0.58	0.64	1.05	1.75
Density liquid (25°C)[kg/L]	0.83	/	0.860	0.960	1.024	1.067
Cetane number [-]	55	55	29	63	70	90
Oxygen content [wt%]	/	34.7	42.1	45.3	47.1	48.2

Table 1.1: Properties of conventional diesel fuel (CDF), dimethyl ether (DME), dymethoxymethane (DMM) and higher OMEs [22].

OMEs with $n > 3$ have a cetane number between 70 and 100, which makes them excellent fuels. Also, their high density ensures to reach the desired oxygen content (42-53 wt%) with a small addition in terms of volume. Since OME_2 has a small flash point, which is important for safety, and heavy OMEs could precipitate and clog filters, the best compromise would be using OMEs with $n = 3$–4.

The most interesting property of OMEs, though, is their reduction potential of NO_x [23] and soot formation. This is due to the activated methylene groups next to the oxygen atoms (-O-CH_2-), which form hydroperoxides in the early stages of combustion: these decompose into $\dot{O}H$ radicals which oxidize and degrade soot precursors [24]. The presence of polyaromatic hydrocarbons (PAHs) is also known to favor soot formation, and OMEs, being synthetic fuels, do not contain the PAHs naturally occurring in crude oil [25]; combustion of pure OME_1, for example, shows no soot formation at all [26]. As a downside, high CO emissions are reported [27, 28], which could suggest incomplete combustion: this would cause a deterioration in engine efficiency and it is a problem that needs to be properly addressed.

1.1.2. Synthesis

Figure 1.5 illustrates the two main processes to produce OMEs from methanol. Pathway A has been studied in detail and optimized [22, 29–31]; the intermediates are in this case trioxane and DMM, both derived from formaldehyde, which comes from dehydrogenation of methanol. Also DME can be used instead of DMM to react with trioxane, allowing a single integrated process [22, 32]. This process results in a higher selectivity of OME compared to others. Pathway B, using methanol and formaldehyde, takes advantage of low-cost reactants but it is less consolidated and offers a lower selectivity because of by-products such as water and glycols.

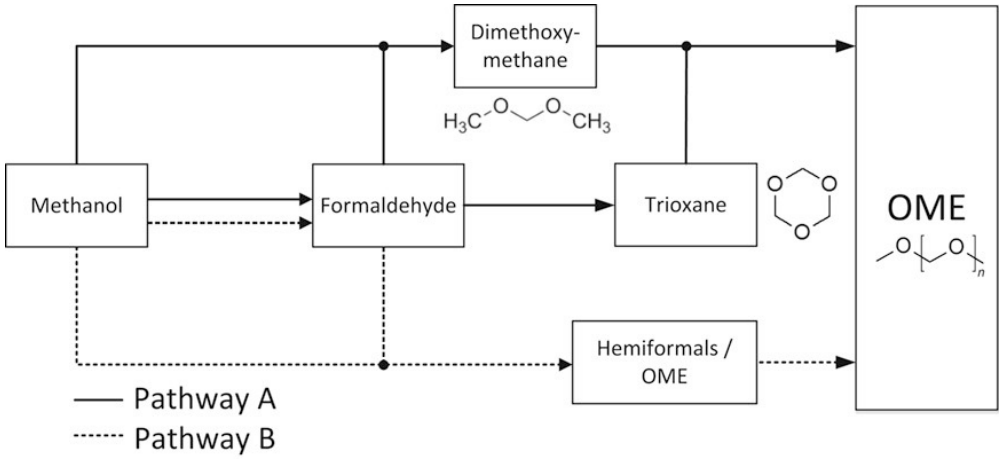

Figure 1.5: Block flow diagram of the main synthesis processes for OME [33].

Methanol is traditionally produced in a steam reforming process but, recently, more sustainable possibilities have opened. Converting biomass-derived synthesis gas is a viable option [34], but also using captured CO_2 with electricity. Those routes are the most promising in terms of carbon footprint and energy performances and have been studied in detail, together with a combined hybrid process [35]. DME can be obtained from methanol too, through a low cost dehydration step [36] or, more conveniently, in a direct route integrated in the OME synthesis [37].

A whole process from biomass (biological sources, including plants, foods and animal wastes) to OMEs has been recently proposed [38–40]. These sources are considered carbon-neutral since the CO_2 released using biomass can be absorbed during its lifetime, creating a closed carbon loop, differently from fossil fuels which release additional carbon into the atmosphere.

Another production route for OMEs that guarantees a closed carbon loop is its synthesis with CO_2 and renewable hydrogen [41, 42]. In Figure 1.6 two possibilities are reported. In both cases, methanol is produced via catalytic reduction of carbon dioxide with hydrogen. CO_2 can be captured from air or produced in bio-gas plants and H_2 ideally comes from water electrolysis through renewable power. In the first pathway OME_1 is obtained from a condensation reaction of methanol and formaldehyde but, since formaldehyde production involves an oxidation step, this route is red-ox inefficient. The second pathway, instead, follows a purely reductive route where methanol catalytically generates the central CH_2 unit of the OME [41, 43]. This anhydrous path also prevents the formation of the many side-products that the use of water inevitably produces. This means also that separation is not needed, which is a main factor in energy (and hence carbon) footprint.

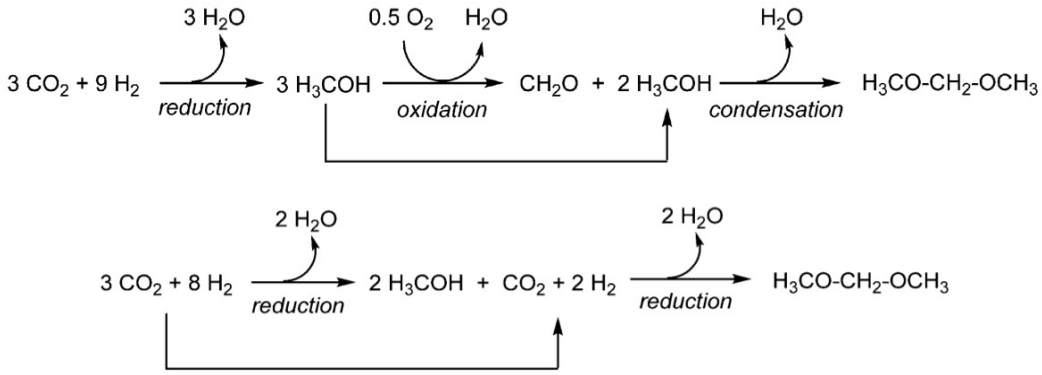

Figure 1.6: Two main possible pathways of DMM synthesis from CO_2 and hydrogen [44].

All the mentioned processes produce mixtures composed mainly of $OME_{1–5}$, with lower amounts of heavier ethers. If the goal is to obtain a single OME with uniform chain length, additional separation and purification steps are required. This inevitably increases costs and energy consumption, and for this reason a lot of research is focusing on using directly as fuel the mixtures with the synthesis composition.

1.2. Kinetic mechanisms

In order to improve engines efficiency and reduce consumptions and emissions, research on both engines and fuels must be done. It is inevitable that, to accomplish this, great knowledge of fluid dynamics and kinetics of the combustion process is required. With the increasing computational power available, the empirical approach has gradually been

replaced by a more systematic method, based on simulations. This implies that models are now built upon rational and predictive principles, and not only on the base of the experimental results. Kinetic parameters, for example, are derived from quantum chemistry calculations, or applying consolidated rate rules.

As a matter of fact, numerical modeling has defined the last decades of combustion research, with more and more complex models, whose predictions became more accurate. The main advantage of numerical simulation is its flexibility, while experiments are expensive and time consuming. On the other hand, though, a good kinetic mechanism is necessary to guarantee accurate results that follow the experimental behaviours.

It was in the 1970s that, thanks to the more accessible computational capability, studies on kinetic mechanisms began emerging, with hydrogen and methane being the first investigated fuels [45]. The understanding of the detailed chemistry of methane combustion anticipated further kinetic studies, but it was not until the mid 1990s that the computers were developed enough to handle detailed models of heavier fuels. The hierarchical approach has simplified the job greatly: in order to extend an already existing kinetic model to a new fuel, it is sufficient to add the subset of reactions that, from the new molecule, lead to the smaller ones, already completely described [46].

One major drawback of this method is that, even with the computational power currently available, detailed kinetic models in several cases cannot be used in Computational Fluid Dynamics (CFD) simulations. The limit is indeed imposed by the number of reactions and, especially, species, which increase computational times according to a power law with exponent between 2 and 3 [47]. This is due to the transport equation that must be added for each new species, which enlarge the Jacobian matrices required to solve steady-state or dynamic problems. Obtaining results in an acceptable time is, for this reason, often impossible with detailed mechanisms, and another approach is required. For example, the evaluation of the laminar burning velocity of a flame using a one-dimensional model and adopting a serial solver, would already require some weeks when about 400 species are involved [48]. A viable solution would be a simplification of the model with the lumping approach, which will be discussed in detail in the next Chapter.

Specifically regarding OMEs, a lot of research has been focused on DME (OME_0) and DMM (OME_1). Because of their smaller length, it is possible to estimate the rate constants of the elementary reaction pathways with more accurate calculations [49–51], and subsequently implement them in kinetic models [52–54]. For the larger molecules of the series, the available mechanisms are based on analogies with smaller ethers [55] or alkanes [56], or obtained optimizing other kinetic models on experimental results [57].

The majority of mechanisms so far has been using OME_3 as the only fuel, for which a broad range of experimental data are available. This is because, as already stated, it is considered among the most promising as diesel additives, if mixtures are excluded. A complete mechanism including all OMEs up to $n = 4$, though, has been recently developed by Cai et al. [58]: a reaction class based methodology was combined with the principle of hierarchy in order to obtain an automatic generation process for the reactions and their kinetic parameters. The reference for the reaction classes was the OME_1 mechanism by Jacobs et al. [51], schematically represented in Figure 1.7. The agreement with the experimental data was finally improved with an optimization of the pre-exponential factors based on reaction rate rules [59].

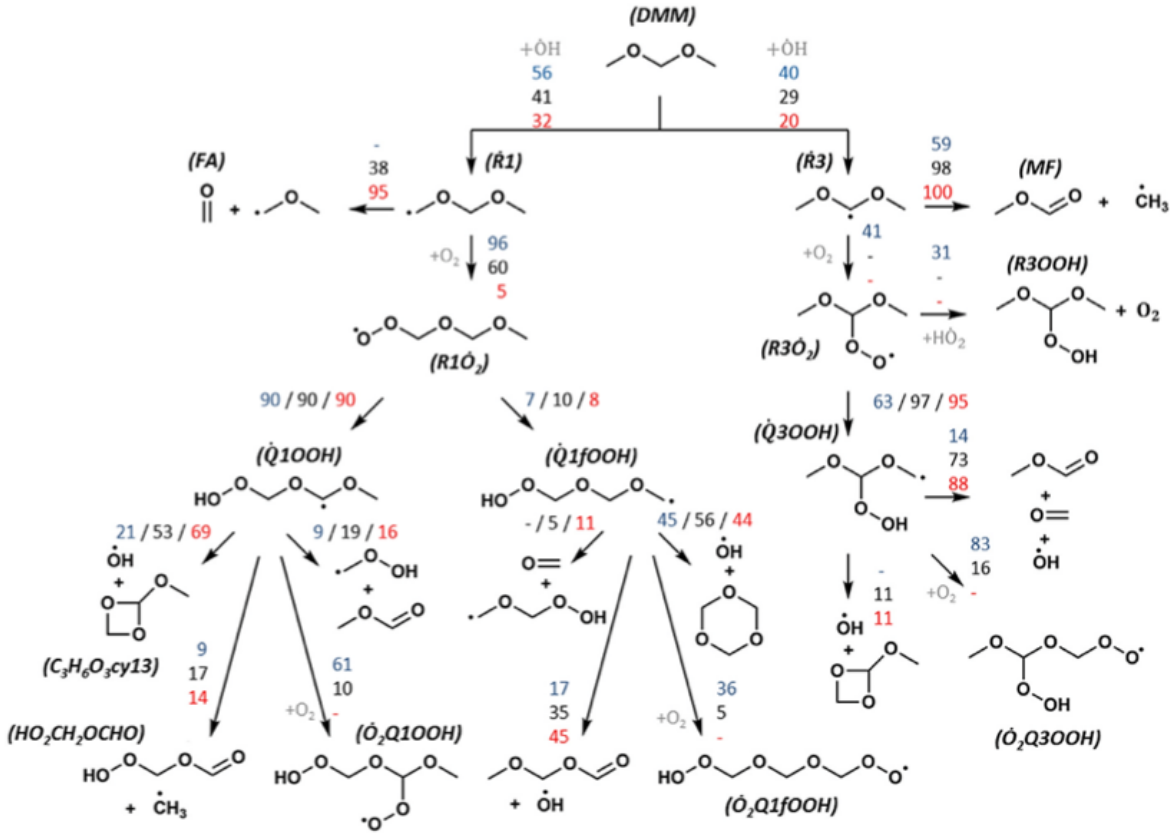

Figure 1.7: Representation of the low temperature kinetics of OME_1 combustion. The flux analysis is performed at $P = 20$ bar, under stoichiometric conditions, when the 20% of the initial concentration of fuel is consumed, at $T = 600$ K (blue), $T = 825$ K (black) and $T = 1150$ K (red) [51].

Since the number of species increases more than linearly with the chain length of the OME, a detailed mechanism rapidly reaches an unacceptable number for large CFD

simulations, and preliminary reduction techniques become essential [60]. Luckily, the regular structure of OMEs and their intrinsically hierarchical nature allow a simple enough lumped formulation of their kinetics. There are examples in literature [61] that shows the good results of the lumping approach in obtaining low and high temperature mechanisms for long-chain fuel, maintaining a good accuracy. Furthermore, this approach looks particularly suitable for a systematic downstream optimization of the reaction parameters in order to improve the agreement with the experimental data. The relatively small size of the lumped mechanism is, in fact, a big advantage in the optimization procedure, which can be faster and performed on a wider amount of data: not only Ignition Delay Times (IDTs) in Shock Tubes (STs) and speciations in Jet Stirred Reactors (JSRs), but also Laminar Flame Speeds (LFSs) which are more demanding of computational resources.

1.3. Aim and structure of the thesis

The ultimate purpose of this Thesis is to combine the lumping procedure and the subsequent mechanism optimization, in order to obtain a smaller comprehensive kinetic scheme for OME_{1-4}, validated for pyrolysis and combustion in a broad set of conditions. In Chapter 1 an overview of the subject is given, with the current state-of-the-art. Chapter 2 shows the methodology adopted for the construction of the mechanism, starting from pre-existing ones, and its successive lumping. The focus of Chapter 3 is the optimization of the lumped mechanism, which is illustrated in detail. All the validations performed on the mechanisms with the `OpenSMOKE++` suite [48] are collected in Chapter 4: sticking to the hierarchical approach, the mechanism was constantly validated (against both experimental data and previous mechanisms) for every new OME that was added and after its lumping. Also the final optimized mechanism was validated once more. Finally, in Chapter 5 the conclusions are drawn, and some possible future work is discussed.

2 | Construction and lumping of the kinetic mechanism

The detailed mechanism for $OME_{0–4}$ was set up by merging different sub-mechanisms from the literature, exploiting the hierarchy principle. Each of them was previously built by applying a reaction class based methodology. The modular approach also allowed the mechanism behaviour to be validated for each new sub-mechanism added, as it will be extensively shown in Chapter 4. The lumping procedure was finally performed on the complete detailed mechanism, resulting in the number of both species and reactions being greatly reduced. These operations will be discussed in detail in this Chapter.

2.1. Mechanism construction

The building blocks of the final detailed $OME_{0–4}$ mechanism are shown in Figure 2.1: the core is a high temperature C_1-C_3 mechanism from CRECK group [62–64], to which the ethers chemistry was gradually added.

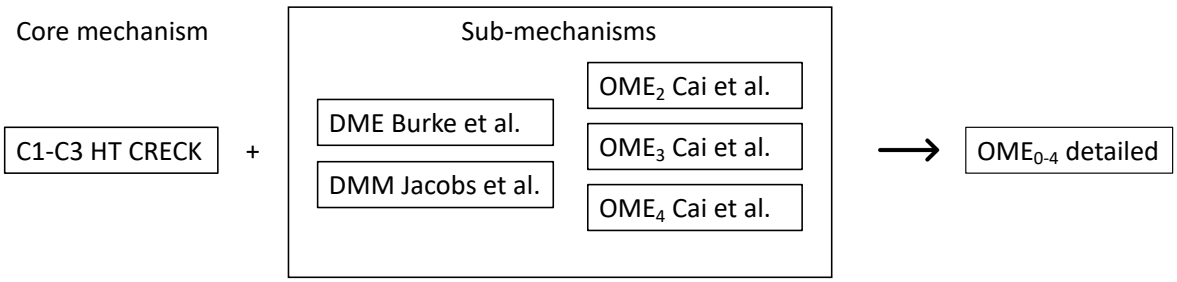

Figure 2.1: Structure of the OME kinetic mechanism: DME, DMM and OMEs sub-mechanisms were added to the core C_1-C_3 mechanism.

In the CRECK kinetic framework, the H_2/O_2 and C_1-C_2 modules had been adopted according to Metcalfe et al. [65] and improved with the work of Bagheri et al. [62]. On top of them, the C_3 model developed by Burke et al. [66] had been added. The DME low

and high temperature sub-mechanism was obtained from a work by Burke et al. [67], in which additional reaction pathways had been implemented [68] (see Figure 2.2) in order to predict more accurately the behaviour of intermediate species such as formic (HOCHO) and carbonic (HOCOOH) acids. Also H-abstractions by H, HO_2, $O(^3P)$ and CH_3 were updated according to studies by Cavallotti et al. [69]. The DMM sub-mechanism was integrated from Jacobs et al. [51] without major modifications. Heavier OMEs ($n = 2$–4) were finally taken into account with the sub-mechanisms proposed by Cai et al. [58], which, as already mentioned, was generated by an automated process using the DMM mechanism by Jacobs et al. as reference and subsequently optimized [59]. The final detailed mechanism included 282 species and 2657 reactions.

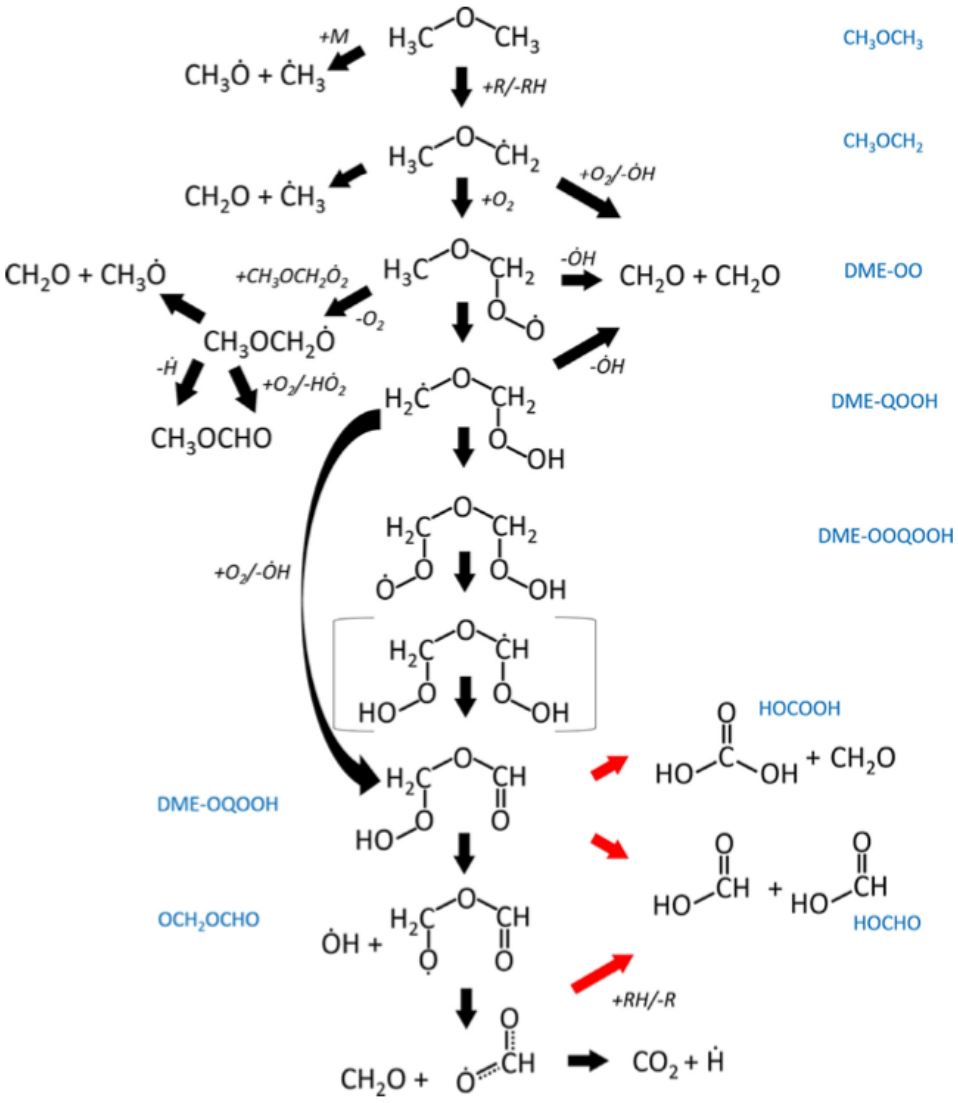

Figure 2.2: DME low-, medium- and high-temperature oxidation pathways. Red arrows highlight routes added to improve the original model [68].

2.1.1. Species nomenclature

A coherent species nomenclature system was adopted throughout the sub-mechanisms for clarity. Each species is labeled with its sub-mechanism name, its class and a number to identify the isomer. For example, alkyl radicals of the DMM are called DMM-R1 and DMM-R2, hydroperoxydes of the OME_2 are OME2-ROOH1 and OME2-ROOH2, and so on. Their respective lumped pseudospecies, defined in the next Section, maintain the same name, without the isomer label: DMM-R, OME2-ROOH, and so forth. An exhaustive list of all pseudospecies is in Appendix A.

2.1.2. Pressure dependence

Both DME and DMM sub-mechanisms involve pressure-dependent reactions for low-temperature chemistry, which increase their level of complexity. In the kinetic file, these reactions are modeled in a logarithmic format, known as PLOG [70], which is gradually replacing the Troe formulation [71] because of its potentially superior accuracy. PLOG reactions are expressed using multiple sets of Arrhenius parameters, each describing the temperature dependence at different constant pressures. For a pressure P between P_j and P_{j+1}, the kinetic constant k can be obtained through the logarithmic interpolation in Equation (2.1):

$$\ln k = \ln k_j + (\ln k_{j+1} - \ln k_j)\frac{\ln P - \ln P_j}{\ln P_{j+1} - \ln P_j} \tag{2.1}$$

Higher OMEs chemistry, on the other hand, is not pressure-dependent. This simplifies their lumping, as will be mentioned in the next Section.

2.1.3. Preliminary modifications

DMM and OME_{2-4} sub-mechanisms by Jacobs et al. [51] and Cai et al. [58] were slightly simplified before being adopted for the final OME_{0-4} mechanism. Specifically, they involved some duplicate reactions, such as DMM-O2QOOH1⇔DMM-OQOOH1+OH and its heavier homologues. Duplicate reactions are usually adopted to model reactions with non-Arrhenius behaviour, but in this case they were unnecessary. As a matter of fact, they were added together and refitted in a three parameters modified Arrhenius form, shown in Equation (2.2), maintaining a coefficient of determination R^2 above 0.99.

$$k(T) = AT^{\beta}e^{-\frac{E_a}{RT}} \tag{2.2}$$

Another modification was the removal of some fast decomposing species by making them react directly into their decomposition products. This means that if the species B produced in A⇒B+C subsequently decomposes in B⇒D+E, it can be skipped by assuming that A⇒D+E+C. Species removed were CH_2OCOOH, CH_3OCOOH, CH_3OCOO, OCHOCHO and CH_2O_2H, all from the DMM sub-mechanism. The mechanism behaviour was checked to be unaffected, confirming the assumption of instant decomposition.

2.2. Chemical lumping

The chemical lumping procedure has the ultimate purpose to reduce the number of species and reactions of a model, retaining as much accuracy as possible. In order to do that, different species are grouped together into single pseudospecies with averaged thermodynamics and transport properties. Subsequently, reaction rates need to be properly adjusted to take into account the merging of reactants and products. In this Thesis the lumping process was performed on each OME sub-mechanism individually, again according to the hierarchy principle. The more isomers and branchings a mechanism involves, the greater it is the advantage of its lumping. For this reason DME, not including isomers and branchings at all, did not need any work; OME_4, instead, benefited of the largest reduction.

For the sake of obtaining an automatic and efficient workflow, a Master Equation Lumping (MEL, available at `https://github.com/lpratalimaffei/MEL`) methodology [72] was exploited; MEL was initially designed to process and simplify multi-well master equation simulations, but was adapted successfully to the purpose of this Thesis. The approach, conceived to group together species with similar chemical behaviour and treat implicitly unstable intermediates reactivity, was extended to work on a complete mechanism. For the first time, MEL was applied successfully to the reduction of a detailed kinetic scheme. The five steps describing the procedure, repeated separately for each OME sub-mechanism, are the following:

1. all the pseudospecies are defined together with the various isomers they group. The chosen criterion was structural isomerism, so the classification was straightforward. Moreover, each pseudospecies maintained in most of the cases the same functional groups;

2. the complete detailed mechanism is divided into blocks, each characterized by reactions having the same global stoichiometry. For example, the combination reaction A+B⇒C and its subsequent isomerization C⇒D belong to the same block, contrarily to C+E⇒F, which involves more atoms and is included in a different block;

3. the equilibrium reactions of the detailed model are split into forward and backward ones, according to the thermodynamic equilibrium restrains. This is due to the fictitious nature of the pseudospecies: they cannot be included into equilibrium reactions without losing physical meaning;

4. zero-dimensional isothermal and isobaric simulations are performed to evaluate the compositions of each pseudospecies as function of pressure and temperature. DMM was the only exception for which the compositions were evaluated directly by MEL, as it will be remarked later;

5. the reactions parameters for each block are calculated, either manually or with MEL, and the lumped OME sub-mechanism is assembled.

For the final lumped mechanism to be obtained, these operations were performed on all four OMEs. Since the process was almost identical for each of them, with some minor exceptions for DMM, OME_2 will be mostly used as example to illustrate the steps. This is because it is a good trade-off between number of species and mechanism complexity.

2.2.1. Pseudospecies definition

One of the most crucial steps of the lumping procedure is the definition of the various pseudospecies and the selection of the isomers in their pools. In this Thesis, each pseudospecies includes all the species sharing structural isomerism. Figure 2.3 exemplifies the lumping process performed on the Cai et al. [58] OME_2 sub-mechanism. Green/dashed and red/dotted lines highlight the intermediate species that, in the detailed mechanism, are generated starting respectively from the primary and secondary radicals. Blue rectangles group the isomers included in the same pseudospecies.

The low temperature kinetics starts with the formation of an alkyl radical ($\dot{R}$), which, attacked by oxygen, forms a peroxy isomer ($R\dot{O}_2$). This can either react into an hydroperoxide (ROOH), an alkoxy radical ($R\dot{O}$) or isomerize into an hydroperoxy-alkyl radical ($\dot{Q}OOH$). $\dot{O}H$ elimination from $\dot{Q}OOH$ leads to cyclic ethers, while a second O_2 addition produces hydroperxy-alkyl-peroxy radicals ($\dot{O}_2QOOH$), which can react into keto-hydroperoxydes (OQOOH). The combustion proceeds with the β-scission products, which are involved in lower OME kinetics, until the oxidation is complete and mostly H_2O and CO_2 remain. Just by looking at Figure 2.3, the advantage of using a lumped scheme in terms of number of species and reactions is clear: not only the initial 29 isomers have been grouped into 10 pseudospecies, but also the multi-branched chemistry is now described by more linear pathways. A complete list of the pseudospecies defined for all OMEs can be found Appendix A.

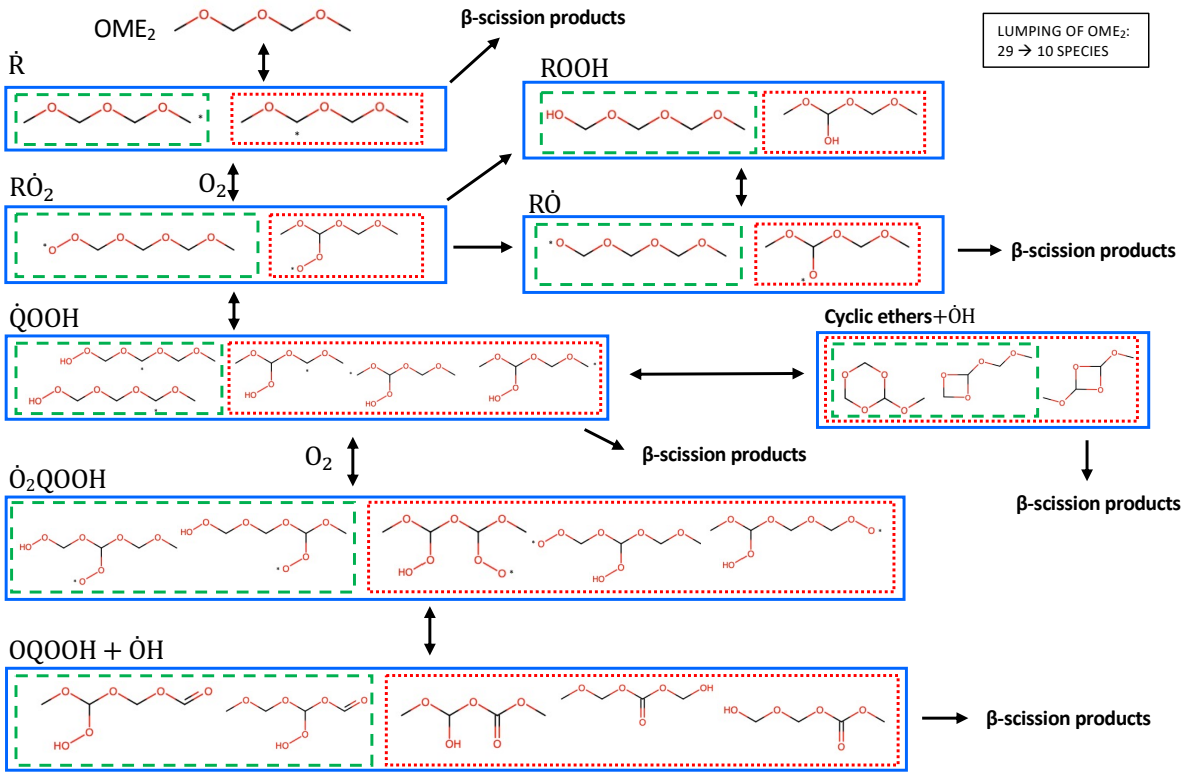

Figure 2.3: Schematic representation of OME_2 kinetics. Green/dashed and red/dotted lines highlight intermediate species originated respectively by primary and secondary radicals. Lumped isomers are grouped by blue rectangles.

2.2.2. Blocks separation

Every sub-mechanism needs to be divided into blocks of reactions sharing the same global stoichiometry, since MEL only handle kinetics respecting this characteristic. Table 2.1 reports, as example, the number of OME_2 blocks, classified by reaction type. For each of them, it is shown the comparison of the number of species and reactions before and after the lumping procedure. $\dot{R}+O_2$ and $\dot{Q}OOH+O_2$, being the largest blocks, benefited the most from the process.

Reaction type	N. of blocks	Species before/after lumping	Reactions before/after lumping
H-abstraction	11	3/2	4/2
$\dot{R}$ decomposition	1	5/4	8/6
$R\dot{O}$ formation	2	4/2	2/1
$\dot{R}+O_2$	1	12/4	24/6
ROOH formation	3	4/2	4/2
$R\dot{O}$ decomposition	1	6/6	5/4
$\dot{Q}OOH+O_2$	1	20/4	15/3

Table 2.1: OME_2 blocks of reactions with the same global stoichiometry, grouped by reaction type.

2.2.3. Equilibrium removal

All equilibrium reactions involving lumped species must be split into forward and backward ones in order to maintain the physical meaning of the system. This is because if the equilibrium reactions are treated as they are, the resulting lumped equilibrium reactions will not describe correctly the behaviour of the reverse ones. On the other hand, lumping separately forward and backward reactions guarantees that the behaviour of all the species is accounted for. `OpenSMOKE++` kinetic preprocessor [48] is able to evaluate the reverse kinetic constant k^b for each reaction, from the forward k^f and the equilibrium K^e constants as in Equations (2.3) and (2.4):

$$k^b = \frac{k^f}{K^e} \tag{2.3}$$

$$K^e = e^{\left(\frac{\Delta\tilde{S}^0}{R} - \frac{\Delta\tilde{H}}{RT}\right)} \left(\frac{P_{atm}}{RT}\right)^{\sum_i^{N_S}\left(\nu_i^b - \nu_i^f\right)} \tag{2.4}$$

where N_S is the total number of species involved in the reaction, and ν_i^f and ν_i^b the stoichiometric coefficients of the i^{th} species in the forward and backward reaction. Reaction entropy $\tilde{\Delta S}^0$ and and reaction enthalpy $\tilde{\Delta H}$ are evaluated according to Equations (2.5) and (2.6):

$$\Delta\tilde{S}^0 = \sum_i^{N_S}\left(\nu_i^b - \nu_i^f\right)\tilde{S}_i^{\,0} \tag{2.5}$$

$$\Delta\tilde{H} = \sum_{i}^{N_S} \left(\nu_i^b - \nu_i^f\right) \tilde{H}_i \tag{2.6}$$

in which $\tilde{S}_i^{\,0}$ and $\tilde{H}_i$ are the specific entropy and enthalpy of the i^{th} species, expressed in the thermodynamic properties file. Finally, the resulting backward kinetic constant is fitted into the three parameters modified Arrhenius form of Equation (2.2).

For the sake of completion, the thermodynamic and transport parameters of the pseudospecies should be an average of the ones of the isomers in their pool, weighted on the compositions evaluated as detailed in the next Subsection. However, since the lumped species do not take part into equilibrium reactions and the isomers parameters were similar enough, the properties of the most abundant isomer were selected to represent the pseudospecies. Concerning the transport parameters, they were identical among all the isomers of the same pseudospecies, and thus did not need any assumptions or modifications.

2.2.4. Composition selection

In order for the lumping to be accurate, the new reaction parameters must be calculated taking into account the isomers distribution in each pseudospecies. Using MEL, it is possible to determine the isomers pool of every pseudospecies, separately for each block of reactions; this is done performing a series of simulations with the various isomers in turn as reactants and all the others as products, applying an infinite sink approximation. Despite this being effective for lumping independent blocks, it presents a big limit when applied to a whole mechanism: the interactions between different blocks of reactions are ignored, inevitably losing information about isomers subsequent reactivity.

DMM was the only sub-mechanism which was lumped according to the composition selection performed by MEL, because the subsequent reactivity of its isomers did not play a relevant role. Since its mechanism contained pressure-dependent reactions, pressures of 0.01, 1, 2, 10, 20, 100 and 500 bar were selected for the simulation of reaction blocks involving them, in a wide temperature range of 500-2000 K. On the other hand, using isomer compositions calculated by MEL for OME_{2-4} lumping resulted in very poor models.

In order to account for the intrinsic interconnection among multiple blocks, which are more significant for heavier OMEs, a different strategy was exploited. `OpenSMOKE++` was adopted to perform zero-dimensional isothermal and isobaric simulations with the OME as reactant, in the same temperature range of 500-2000 K and using the detailed mechanism. The pressure chosen for the simulations was 20 bar: since OME_{2-4} sub-mechanisms did not

include pressure-dependent reactions, it was considered to be a good representative value for the experimental range of P = 1–40 bar. Lean conditions ($\Phi = 0.5$) were selected to better highlight low-temperature combustion kinetics. The averaged, temperature-dependent branching fractions (BFs) to be imposed in MEL for the parameters evaluation were then calculated from the simulations results. In particular, BF_i of each i^{th} isomer in a pseudospecies was determined according to Equation (2.7):

$$BF_i = \frac{\int_0^{t_{max}} X_i(t)dt}{t_{max}} \tag{2.7}$$

in which X_i is the i^{th} isomer fraction in the total isomers pool, defined in Equation (2.8):

$$X_i(t) = \frac{x_i(t)}{\sum_i^{N_S} x_i(t)} \tag{2.8}$$

where x_i is the mole fraction of the i^{th} isomer and N_S the total number of species in the pool. In Equation (2.7), t_{max} is the time of the simulation when the maximum mole fraction of total isomers is reached, after which it rapidly drops to zero because of the oxidation ending. Figure 2.4 shows, as example, the BFs of the five isomers of the OME2-QOOH pseudospecies in the low-temperature area.

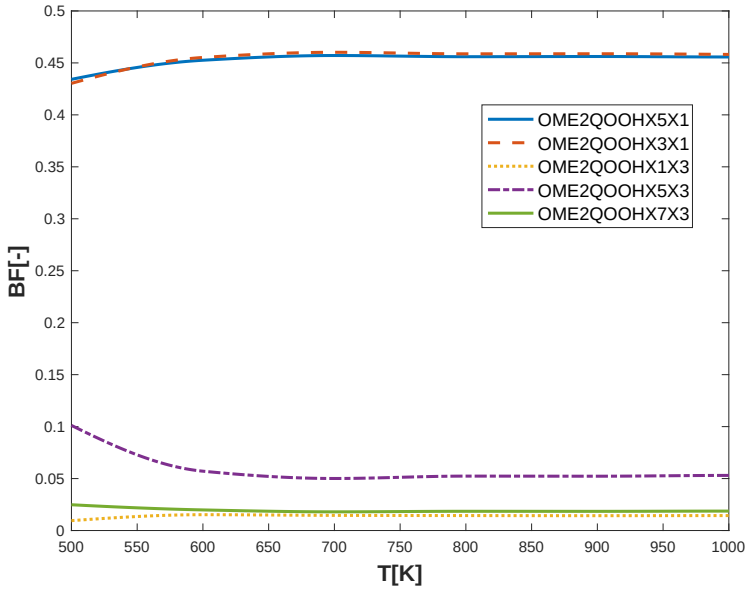

Figure 2.4: BFs of the OME2-QOOH pseudospecies in the 500-1000 K temperature range. The two main isomers (OMEQOOHX5X1 and OMEQOOHX3X1) constitute in this case about 90% of the total isomers pool, and effects of temperature are minimal.

2.2.5. Parameters evaluation

Most of the lumped reaction parameters were calculated with MEL, simulating separately each mechanism block. The procedure was described in detail in a recent work [72], and will be reported here briefly. To begin with, the set of $\tilde{N}$ pseudospecies is defined, specifying merged and unmerged species. Then, the ODE system $d\boldsymbol{c}/dt = \boldsymbol{K}\boldsymbol{c}$ describing the evolution of the initial set of N species ($\boldsymbol{K}$ is the rate constant matrix in the detailed model and $\boldsymbol{c}$ the species concentration vector) is reduced to the equivalent lumped system $d\tilde{\boldsymbol{c}}/dt = \tilde{\boldsymbol{K}}\tilde{\boldsymbol{c}}$. The system $d\boldsymbol{c}/dt = \boldsymbol{K}\boldsymbol{c}$ needs to be solved in $\tilde{N}$ sets of simulations: in each set, one of the $\tilde{N}$ pseudospecies is the reactant, and all the others are the products. The concentration of the products can only increase in time, because of the infinite sink approximation applied, resulting in an exponential decay of the reactant. This allows to approximate the lumped rate constants of the matrix $\tilde{\boldsymbol{K}}$ from a differential fit of the product concentration profiles produced by each pseudospecies. These concentration profiles of the lumped system $d\tilde{\boldsymbol{c}}/dt = \tilde{\boldsymbol{K}}\tilde{\boldsymbol{c}}$ are derived from the ones of the detailed system, solved using the BFs previously evaluated as initial conditions. Finally, the derived lumped mechanism is validated comparing its performances in zero-dimensional isothermal and isobaric simulations against those of the detailed mechanism.

The only reactions whose lumped parameters were evaluated manually were the ones yielding more than two products. The lumped rate constants in these cases were derived as in Equation (2.9):

$$k(T)_{L\to P} = \sum_i BF(T)_i \cdot k(T)_{i\to P} \tag{2.9}$$

where $i \to P$ represents the reaction of the i^{th} isomer to the set of products P, whereas $L \to P$ indicates the lumped reaction. The obtained values of $k(T)_{L\to P}$ were finally fitted in the modified Arrhenius form already shown in Equation (2.2).

2.2.6. Lumping results

The big advantage of the lumped mechanism over the detailed one, progressively growing with the chain length, is clearly shown in Figure 2.5. As a matter of fact, both the number of species and reactions in the lumped mechanism increase only linearly with every new OME included. Contrarily, the detailed mechanism size grows faster because of the larger number of structural isomers modeled. The final lumped OME_{0-4} mechanism counts 176 species and 2486 reactions, saving more than 100 species out of the 282 of the detailed

model. The usefulness of the lumped kinetics has been qualitatively confirmed by a great reduction of computational times for heavy simulations. The good accuracy retained will be confirmed by the validations in Chapter 4.

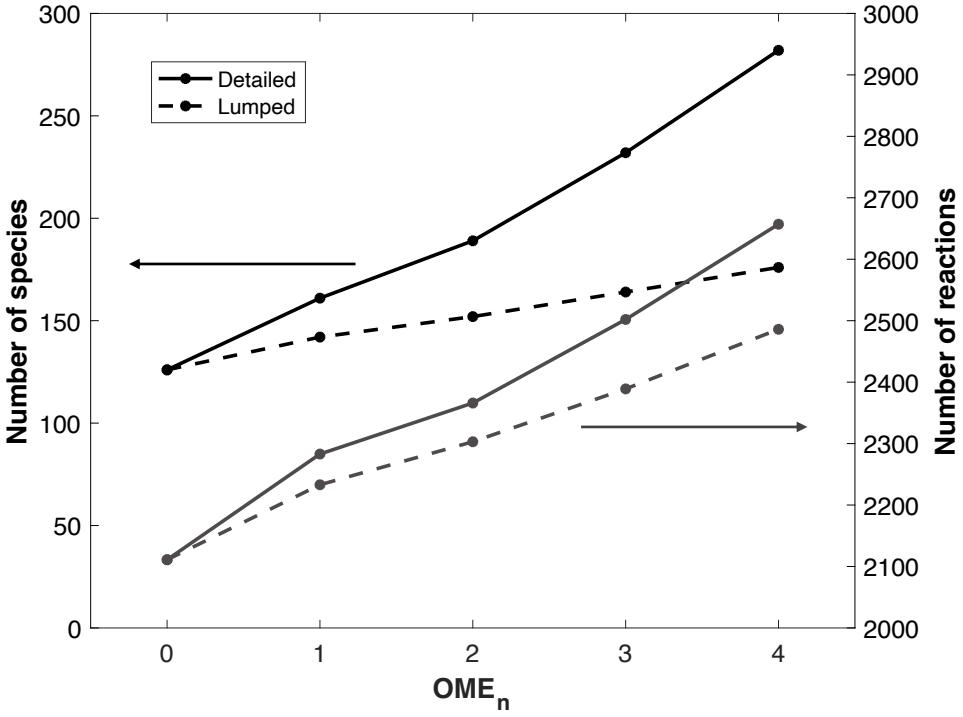

Figure 2.5: Comparison between detailed and lumped mechanisms number of species (black/left) and reactions (grey/right). These refer to the size of the whole mechanism, increasing with every new OME sub-mechanism added. DME does not present any difference between detailed and lumped mechanism because it could not be reduced any further.

3 | Optimization of lumped mechanism

The lumped OME_{0-4} mechanism underwent an optimization process to improve its agreement with the experimental measurements available in literature. The methodology presented by Bertolino et al. [73] was adopted to this purpose, applying it for the first time to a lumped mechanism using the `OptiSMOKE++` toolbox [74]. This approach is based on an evolutionary algorithm that optimizes the three parameters of the modified Arrhenius expression. The reactions to be optimized are identified by performing sensitivity analyses on the various cases. In this Chapter, after an overview of the toolbox, the workflow exploited to obtain the final optimized lumped OME_{0-4} mechanism will be described.

3.1. `OptiSMOKE++`

The `OptiSMOKE++` toolbox applies heuristic optimization strategies to refine uncertain kinetic parameters. The optimization targets can be experimental data from several ideal reactors, including IDTs in Batch reactors (adopted to simulate STs) and Rapid Compression Machines (RCMs), species concentrations in JSRs and Plug Flow Reactors (PFRs), and LFSs. The numerical simulations are performed on `OpenSMOKE++` [48], while the DAKOTA toolkit [75] handles the optimization. DAKOTA includes a variety of optimization algorithms, which can be selected by the user.

Figure 3.1 depicts an overview of the `OptiSMOKE++` workflow. After the input file is read, the code changes the chosen parameters of the kinetic scheme, and checks that all of them are within the uncertainty bounds, applying a non-linear constraint $k_{min} \leq k \leq k_{max}$. If at least one falls outside the bounds, a penalty function is applied and the simulations are skipped to save computational time, otherwise `OpenSMOKE++` runs the simulations, and the objective function is calculated from the results. At this point, DAKOTA suggests a new set of parameters, based on the value of the objective function, and the operation is repeated until at least one of the stopping criteria is reached.

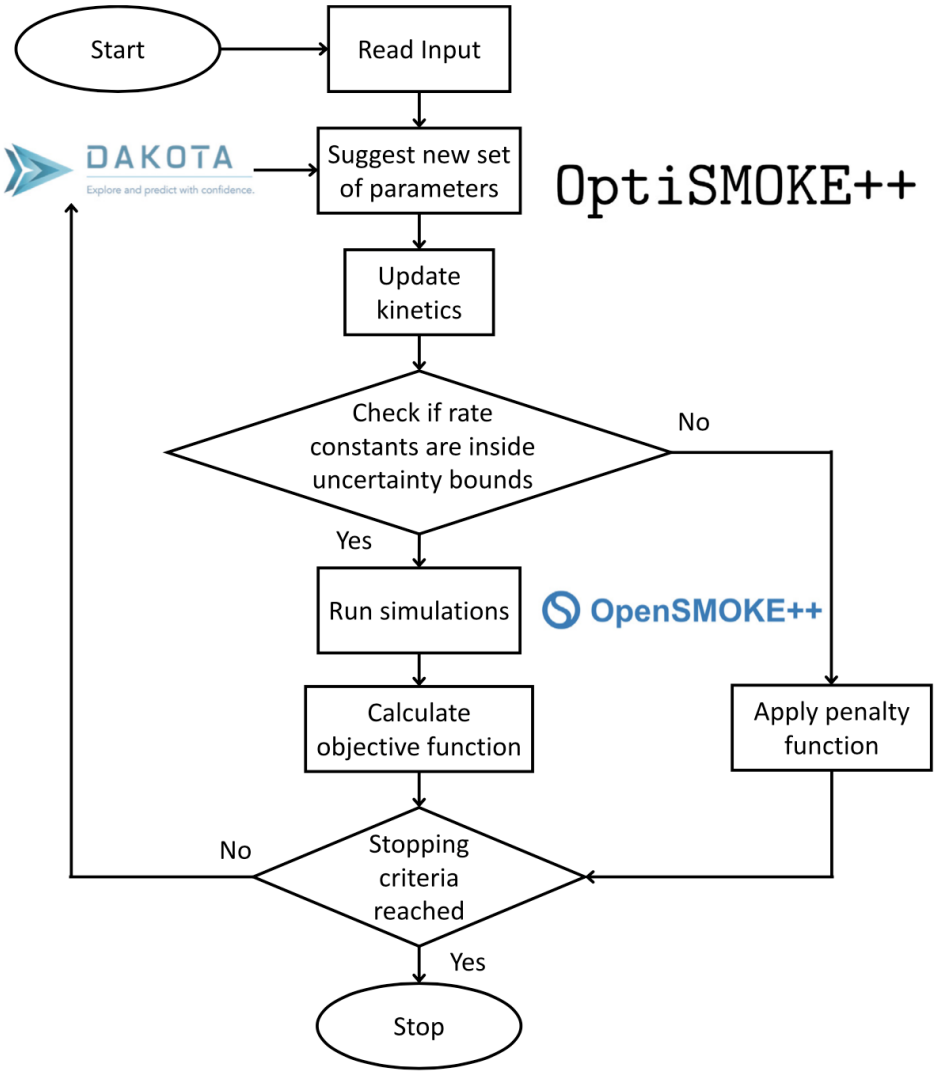

Figure 3.1: `OptiSMOKE++` schematic workflow [74].

3.1.1. Objective function

The solution of an optimization problem is determined based on the evaluation of an objective function, which models the difference between the current evaluation (Y^{sim}) and the experimental targets (Y^{exp}), and whose minimum value corresponds to the problem optimum. One of the most common definitions is the Least Squares, or L^2-norm, reported in Equation (3.1), where the residual is squared for each data point j in each dataset i. N is the total number of datasets and N_i the number of data points in dataset i.

$$Obj = \sum_{i}^{N} \sum_{j}^{N_i} (Y_{i,j}^{exp} - Y_{i,j}^{sim})^2 \tag{3.1}$$

In order to take into account the different uncertainties of each data point, the varying dimensions of each dataset and the number of datasets, the L^2-norm objective function used by `OptiSMOKE++` is adjusted as in Equation (3.2):

$$Obj = \frac{1}{N}\sum_{i}^{N}\frac{1}{N_i}\sum_{j}^{N_i}\left(\frac{Y_{i,j}^{exp} - Y_{i,j}^{sim}}{\sigma(Y_{i,j}^{exp})}\right)^2 \tag{3.2}$$

where σ is the standard deviation. To avoid numerical problems, experimental targets scattered proportionally to the experimental value itself, such as IDTs, are included in the objective function through their natural logarithm: $Y_{i,j}^{exp} = \ln(y_{i,j}^{exp})$ and $Y_{i,j}^{sim} = \ln(y_{i,j}^{sim})$, where $y_{i,j}^{exp}$ and $y_{i,j}^{sim}$ represent the experimental and simulated value for point j in dataset i. Without this, the objective function would not be evenly distributed between data points, and it would be harder to achieve a general improvement [76]. For other targets, as species concentrations and LFSs, the objective function is derived directly from the absolute value of the experimental and simulated results: $Y_{i,j}^{exp} = y_{i,j}^{exp}$ and $Y_{i,j}^{sim} = y_{i,j}^{sim}$.

Another possible definition of objective function is based on the Curve Matching (CM) index [77], first introduced by Bernardi et al. [78]. This approach compares functional estimations of experiments and models based on splines interpolation, smoothed by a roughness penalty on the second derivative. Also a cross-validation applied on the first derivative of the function is adopted [79]. For the CM index to be evaluated, the norm of a curve h in the L^2-space needs to be introduced, as in Equation (3.3):

$$||h|| = \sqrt{\int_D h(x)^2 dx} \tag{3.3}$$

The curves of the model m and of the experiments g, belonging to the dataset i are compared through the Pearson dissimilarity indices reported in Equations (3.4), (3.5), (3.6) and (3.7):

$$d_{i,L_2}^0 = \frac{1}{1 + \frac{||m-g||}{|D|}} \in (0,1) \tag{3.4}$$

$$d_{i,L_2}^1 = \frac{1}{1 + \frac{||m'-g'||}{|D|}} \in (0,1) \tag{3.5}$$

$$d_{i,P}^0 = 1 - \frac{1}{2}\left|\left|\frac{m}{||m||} - \frac{g}{||g||}\right|\right| \in (0,1) \tag{3.6}$$

$$d^0_{i,P} = 1 - \frac{1}{2}\left\| \frac{m'}{||m'||} - \frac{g'}{||g'||} \right\| \in (0,1) \tag{3.7}$$

where m' and g' are the first derivatives of the curves and D the intersection of their domains. The overall performance index of the model, with respect to the experimental dataset i, is computed as in Equation (3.8):

$$CM_i = \frac{d^0_{i,L_2} + d^1_{i,L_2} + d^0_{i,P} + d^1_{i,P}}{4} \in (0,1) \tag{3.8}$$

The more the index approaches 1, the more the two functions are similar, and thus the model better reproduces the experimental values of set i. The related objective function is reported in Equation (3.9), where N is again the number of datasets. It is also possible to introduce a number of bootstrap variations N_b, in which case the expression becomes the one in Equation (3.10):

$$Obj = \frac{1}{N}\sum_{i}^{N}(1 - CM_i) \tag{3.9}$$

$$Obj = \frac{1}{N}\sum_{i}^{N}\left(1 - \frac{1}{N_b}\sum_{j}^{N_b} CM_{i,j}\right) \tag{3.10}$$

Both L_2 and CM objective functions were tested on the DMM sub-mechanism optimization for this Thesis. It was assessed that the optimized mechanism derived with the CM approach behaved slightly better. The decision was then to adopt the CM objective function for the optimizations of all sub-mechanisms.

3.1.2. Uncertainty of kinetic parameters

The acceptance limits of the rate constants for each reaction are defined from the uncertainty factor f, as $k_{min} = k_0 \cdot 10^{-f}$ and $k_{max} = k_0 \cdot 10^{f}$, where k_0 is the nominal kinetic constant before the optimization. On its part, f can be estimated from the spread of the direct experimental data and theoretical estimation of a specific constant in the literature, as $f = 0.5 \cdot \log(k_{max}/k_{min})$. Specific uncertainty ranges of kinetic parameters A, β and E_a can also be evaluated from these limits, as previously done by Fürst et al. [80].

`OpenSMOKE++` uses the rate constant expression of Equation (3.11) in order to reduce time expensive calculations.

$$k = \exp\left(\ln(A) + \beta \ln(T) - \frac{E_a}{RT}\right) \tag{3.11}$$

OptiSMOKE++ employs therefore the same definition, where $\ln(A)$, β and E_a/R are the active parameters for the optimization. Even third body efficiencies can be used as uncertain parameters, as well as low and high pressure limits of fall-of reactions [81].

In the present Thesis, an uncertainty factor $f = 0.3$ was assumed. This was a conservative choice since, among all the values reviewed by Bertolino et al. [73], this was the smallest. The corresponding maximum variation of the optimized rate constant with respect to its original value is of about a factor 2. Figure 3.2 reports, as example, the kinetic constant of the reaction R2146, belonging to the DMM sub-mechanism, before and after optimization. The optimized rate constant falls inside the uncertainty region for the whole temperature range, respecting the limits imposed by k_{min} and k_{max}.

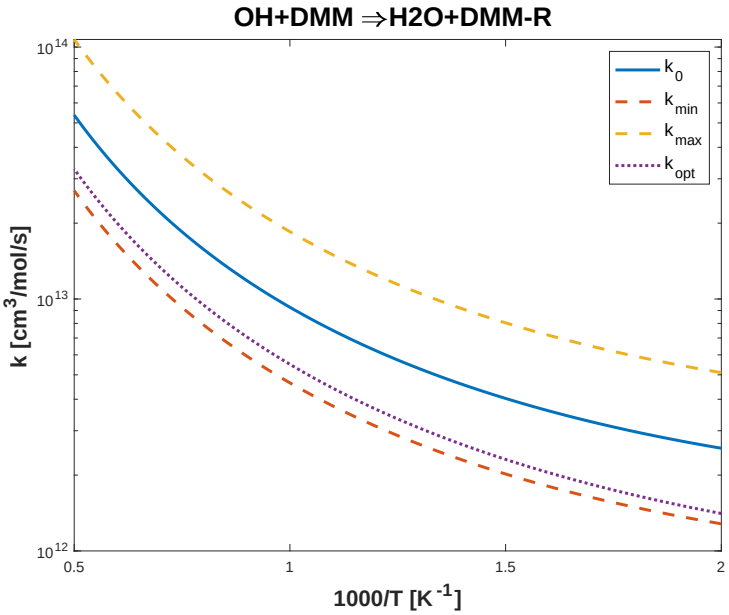

Figure 3.2: Rate coefficient for reaction R2146 of the OME_{0-4} mechanism. k_0 is the nominal kinetic rate of the lumped mechanism and k_{opt} the optimized one: it is demonstrated that it falls inside the uncertainty region between k_{min} and k_{max}, determined by an uncertainty coefficient f of 0.3.

3.1.3. PLOG optimization

OptiSMOKE++ allows to optimize pressure dependent reactions in PLOG format retaining their physical consistency. This could not be done optimizing all their parameters inde-

pendently, since it could lead to a non-monotonic behaviour without physical meaning. Moreover the number of parameters to handle for a single reaction rapidly rises if many pressures are defined. The problem is solved introducing three uniformly distributed random variables, listed in Equations (3.12), (3.13) and (3.14): X_1, X_2 and X_3 are used respectively to correct all A, β and E_a of the reaction simultaneously, so that the same parameters are modified of the same amount.

$$X_1 \in [-\ln(10^f), +\ln(10^f)] \tag{3.12}$$

$$X_2 \in \left[-\frac{f}{\log_{10}(T_{max})}, +\frac{f}{\log_{10}(T_{max})}\right] \tag{3.13}$$

$$X_3 \in [-fT_{min}\ln(10), +fT_{min}\ln(10)] \tag{3.14}$$

An example is reported in Figure 3.3, where the rate coefficient of the reaction R2146, from the DMM sub-mechanism, is represented for different temperatures and pressures. The optimized kinetic constant falls inside the uncertainty region delimited by k_{min} and k_{max} for the whole range of conditions. Despite the weak dependence on P, it is confirmed that the PLOG reaction maintains its monotonic behaviour even after the optimization, thanks to the adopted approach.

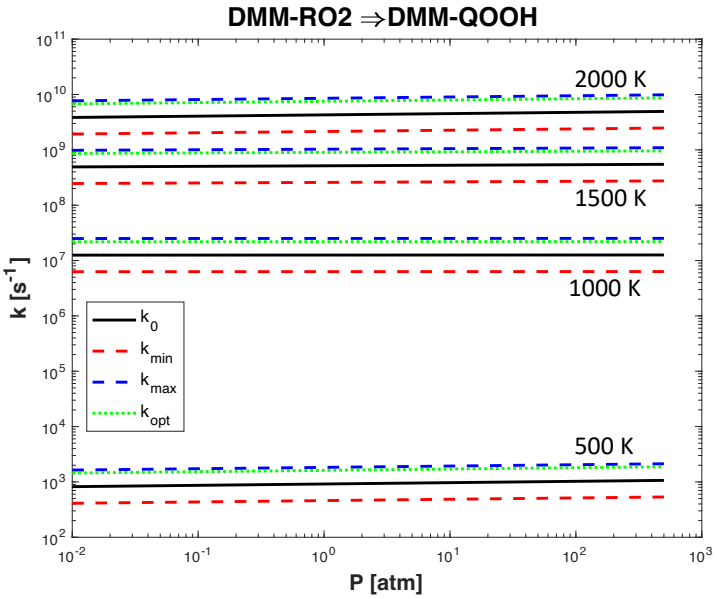

Figure 3.3: Rate coefficient for reaction R2146 of the $OME_{0\text{–}4}$ mechanism at different T and P. k_0 is the nominal kinetic rate of the lumped mechanism, and k_{opt} the optimized one.

3.2. Optimization methodology

The methodology followed to optimize the lumped mechanism can be described as:

1. selection of the datasets to use as optimization targets, among the whole experimental database;
2. choice of the reactions to optimize for each case and sub-mechanism, based on sensitivity analyses;
3. division of the datasets into different blocks of optimizations, depending on the eventual overlap of the sensitive reactions;
4. construction of the final mechanism, merging the optimized reactions from the various optimizations.

An important preliminary decision to be made was whether to optimize the lumped mechanism using the experimental values or the detailed mechanism results as targets. This was a conceptual assumption that would define the purpose of the whole operation: in the first case the optimized mechanism would better reproduce the experiments, but in the second would be more similar to the original detailed kinetics, respecting the philosophy of lumping. In the end, agreement with the experimental values was chosen for the sake of usefulness: since the initial detailed mechanism presented some modeling flaws, it was assumed to be better to improve the lumped optimized kinetics.

3.2.1. Optimization targets

The whole database of experimental results for $OME_{0–4}$ is reported in Chapter 4, and consists of 84 datasets divided into:

- IDTs in Batch reactors;
- speciations in JSRs and PFRs;
- LFSs in premixed laminar flames.

A selection process was performed to divide the datasets into optimization and validation targets. The 28 DME datasets were excluded since its already established mechanism was not involved in the optimization. PFRs results were used in validation for simplicity, hence only JSRs, LFSs and IDTs were evaluated as optimization targets.

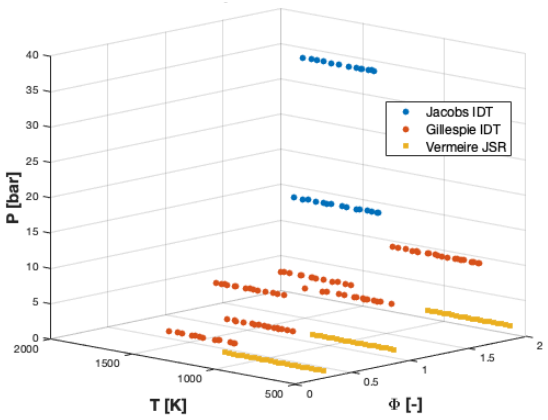

(a) DMM optimization database.

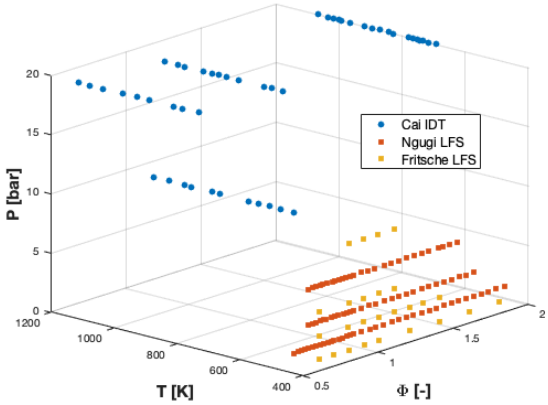

(b) OME_2 optimization database.

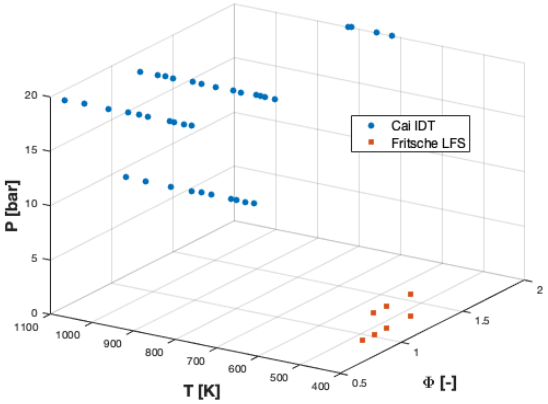

(c) OME_3 optimization database.

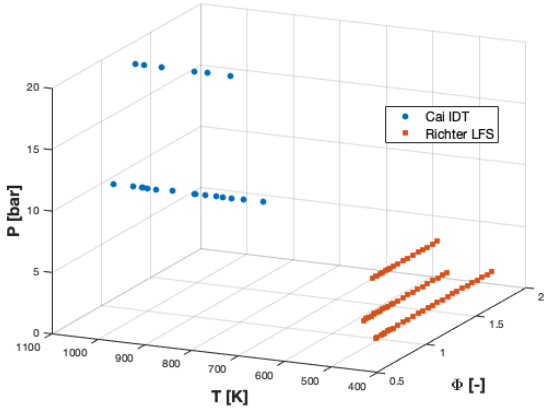

(d) OME_4 optimization database.

Figure 3.4: Experimental data on OMEs combustion adopted as optimization targets, in terms of temperature, pressure and equivalence ratio.

Among the DMM experiments, IDTs by Jacobs et al. [51] and Gillespie [82] were the selected optimization targets, covering a wide range of temperatures ($T \simeq$ 700–1800 K), pressures (P = 1–40 bar) and compositions (Φ = 0.5–2). Jacobs dataset at 9 bar and Gillespie datasets at 3.5 bar were kept for validation, since they covered an operating conditions space already densely populated. JSR optimization was performed on the experiments by Vermeire et al. [50] (low and medium temperature, atmospheric pressure and Φ = 0.25–2). Only DMM mole fractions were used as target, because optimizing on the concentrations of the intermediate species resulted in decreased overall performances of the optimized mechanism. Some experimental points above 1000 K had to be ruled out, for their simulations did not converge in a stationary solution but was oscillating: this is not a numerical issue, but a physical behaviour experimentally observed [83]. No LFS experiment was included in the DMM optimization, since the nominal lumped mechanism already well reproduced the experimental results, as shown in the next Chapter.

$OME_{2–4}$ sub-mechanisms were optimized simultaneously, for reasons that will be clarified in the next Section, therefore they will be here discussed together. They were optimized on all the IDT experiments by Cai et al. [58], performed at $T \simeq 600–1100$ K, $P = 10–20$ bar and $\Phi = 0.5–2$. Results by Ngugi et al. [84], Fritsche et al. [85] and Richter et al. [86], covering $T = 393–473$ K, $P = 1–10$ bar and $\Phi = 0.6–2$, were selected as optimization targets for LFS simulations. Two datasets ($P = 5$ bar and $P = 10$ bar) from Fritsche et al. were used for validation only, because they had one data point each and no reasonable optimization could be carried out.

Figure 3.4 summarizes all the 502 data points from 33 datasets chosen as optimization targets, represented in a temperature, pressure and equivalence ratio space. The whole range of experimental conditions was largely covered for the optimizations, so the remaining 56 $OME_{1–4}$ datasets were reserved for the subsequent validation of the optimized model. For every data entry, it was assumed a relative experimental uncertainty of 20%.

3.2.2. Reactions selection

The selection of the reactions to be optimized was performed evaluating the associated local sensitivity coefficients, normalized with respect to their maximum, along the whole range of operating conditions. The first order coefficient of the variable y with respect to the parameter α is defined in Equation (3.15):

$$s = \frac{\partial y}{\partial \alpha} \tag{3.15}$$

The coefficients were calculated using the `OpenSMOKE++` suite [48] from the lumped mechanism, in a specific way for each dataset according to the variable of interest (IDT, DMM mole fraction or LFS).

For each IDT zero-dimensional simulation, the sensitivity analyses were performed on the $\dot{O}H$ molar fraction, at the temperature corresponding to the inflection point of the ignition curve. Three different characteristic times were selected for each temperature, in order to cover for low-, intermediate- and high-temperature kinetics. An example of these times for OME_2 can be seen in Figure 3.5a: the considered pressures ranged between 1 and 40 bar, according to the experimental results available. The sensitivity coefficients from the example, shown in Figure 3.5b, underline the promoting role of the OME_2 radicals, produced through H-abstraction by $\dot{O}H$ and HO_2 and subsequently consumed in its recombination with O_2 and isomerization to $\dot{Q}OOH$. The decomposition of OME_2 $\dot{Q}OOH$ to the more stable DMM ketones slows down the combustion process instead,

since it reduces the number of radicals driving the ignition and it competes with the low-temperature branching pathways eventually leading to the production of ȮH radicals.

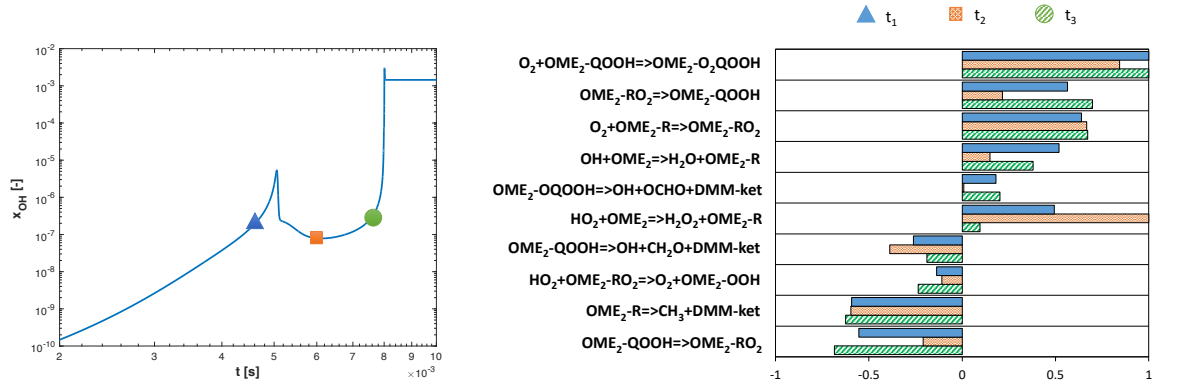

(a) ȮH molar fraction profile and characteristic times.

(b) Normalized sensitivity coefficients to ȮH mass fraction of the 10 most sensitive reactions for the selected times.

Figure 3.5: ȮH molar fraction profile in a zero-dimensional IDT simulation for OME_2 at $P = 9$ bar and $T = 660$ K with characteristic times. Also the 10 most sensitive reactions of the OME_2 sub-mechanism and their normalized sensitivity coefficients are reported.

JSR speciation was investigated with sensitivity analyses carried out on DMM concentration at lean ($\Phi = 0.25$), stoichiometric ($\Phi = 1$) and rich ($\Phi = 2$) conditions. For each, three temperatures were chosen, corresponding to local minimum, maximum and inflection point after the negative temperature coefficient (NTC) region. Figure 3.6 reports these temperatures for DMM at $\Phi = 0.25$. Atmospheric pressure was the only one considered, due to the lack of experimental data in different conditions.

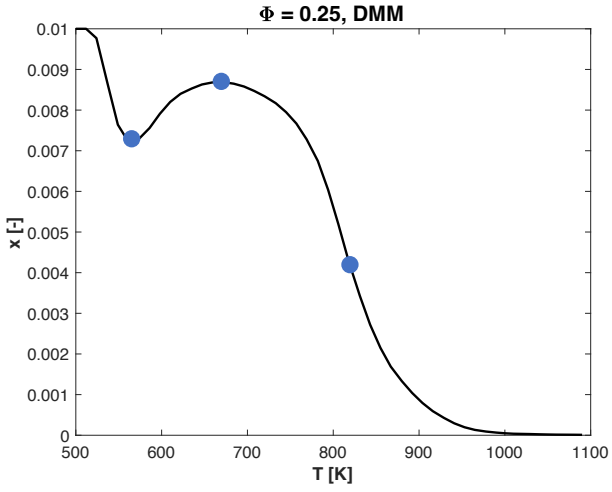

Figure 3.6: Temperatures selected for sensitivity analyses on DMM, in a JSR at $\Phi = 0.25$ and $P = 1.07$ bar.

Finally, the LFS controlling reactions were identified with a mass flow sensitivity analysis at three representative equivalence ratios: one corresponding to the maximum burning velocity ($\Phi \simeq 1.2$), one higher ($\Phi \simeq 1.6$) and one lower ($\Phi \simeq 0.9$). An example for OME_3 can be seen in Figure 3.7. Temperatures and pressures analyzed for each OME were the ones relevant for the experimental conditions.

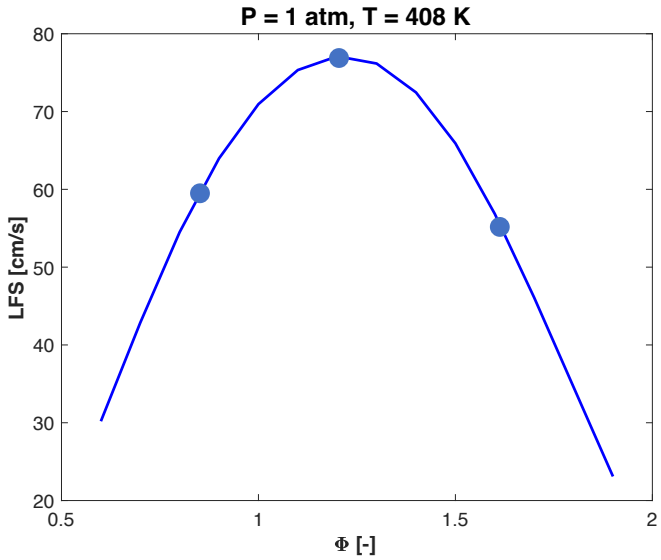

Figure 3.7: Chosen equivalence ratios for mass flow sensitivity analyses of OME_3 LFS, at $P = 1$ atm and $T = 408$ K.

After the analyses were completed, from the resulting reactions those belonging to the DME and C_1-C_3 sub-mechanisms were excluded. Since their parameters had not been modified in the lumping operation, avoiding to optimize them ensures that the original consistency of these sub-mechanism is preserved. From the remaining reactions, all belonging to the OME_{1-4} sub-mechanisms, the first ten from each simulation were selected to be optimized.

3.2.3. Optimization blocks

Having determined ten sensitive reactions for each simulation, in order to decide how to proceed with the optimization, a critical study on which reactions were shared among different simulations was performed. It resulted that all relevant reactions for DMM simulations did not appear in the OME_{2-4} analyses, hence its sub-mechanism could be optimized independently. DMM sensitive reactions for IDTs and JSRs, though, had many entries in common, therefore both optimizations were carried out together. Its LFSs were already very good, and only depended on one reaction that hence was decided

not to be adjusted. $OME_{2–4}$, on the other hand, shared many important reactions and their optimization could not be carried out separately. There were not however common reactions involved in IDTs and LFSs, so the two remained independent.

From this, three separate blocks of reactions, schematized in Figure 3.8, were defined:

- 11 reactions (5 of which in PLOG format) optimized on 8 sets of IDTs and 3 sets of JSR for DMM;
- 42 reactions optimized on 10 sets of IDTs for $OME_{2–4}$;
- 4 reactions optimized on 12 sets of LFSs for $OME_{2–4}$.

The reason for the small number of reactions for the LFSs is the fact that flame propagation is mainly controlled by the C_1-C_3 core reactions [46], however improvements were observed nonetheless and it was decided to include them. All the 53 reactions, with their parameters before and after optimization, can be found in Appendix B; they were finally updated in the lumped mechanism, obtaining the final optimized kinetics. Its modeling predictions are available in the next Chapter, compared to those of the detailed and lumped models and to the experimental data.

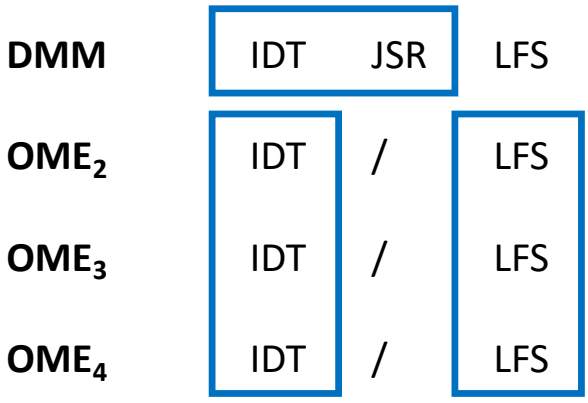

Figure 3.8: Graphical representation of the 3 optimizations performed: DMM sub-mechanism on IDTs and JSRs data, and $OME_{2–4}$ sub-mechanisms on IDTs and LFSs separately. DMM kinetics was not optimized on LFSs due to already good performances. JSRs results were not available except for DMM.

4 | Mechanism validation

In this Chapter the models results, validated against a wide experimental database, are collected and organized by fuel and simulation type. DME cases reports only experimental data and the results from the detailed model, since no lumping and optimization were performed on the DME sub-mechanism. OME_{1-4} Sections include a performance comparison between detailed, lumped and optimized model instead. For each OME except DME, a heat map is also reported, comparing the CM indices of the different mechanisms. In every plot, symbols represent experimental results while lines are for simulations. All simulations have been carried out in `OpenSMOKE++` [48]. IDTs measured in STs have been simulated in Batch reactors, using the same definition adopted in the corresponding paper.

4.1. DME

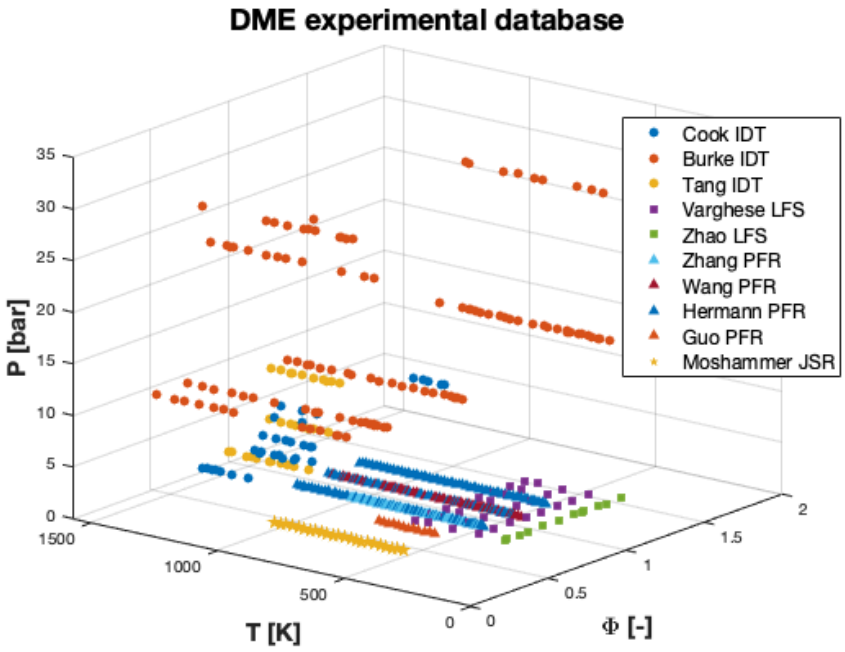

Figure 4.1: DME experimental database.

The experimental database analyzed for DME is the largest available among all OMEs. It consists of 28 sets of experiments, including IDTs measured in STs [66, 87, 88], LFSs, [89, 90] and speciations in JSRs [91] and PFRs [92–95]. All data, represented in a three-dimensional space in Figure 4.1, were used for validation only, since DME sub-mechanism was not optimized.

4.1.1. Ignition Delay Times

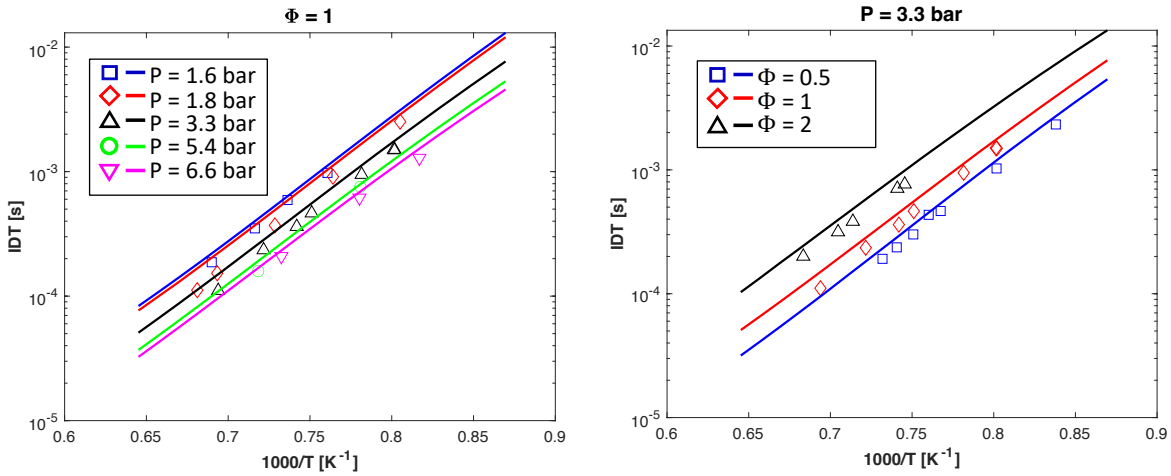

(a) DME IDTs at $\Phi = 1$ and $P = 1.6$–6.6 bar.

(b) DME IDTs at $\Phi = 0.5$–2 and $P = 3.3$ bar.

Figure 4.2: DME IDTs measured in a ST by Cook et al. [87] and model predictions. DME is diluted in 99% O_2 and Ar.

DME IDTs have been measured in a ST by Cook et al. [87], whose results are reported in Figure 4.2, for $T \simeq 1100$–1400, $\Phi = 0.5$–2 and $P = 1.6$–6.6 bar. The model well represents the data in the whole range of interest and no major discrepancies are detected. The same can be said for the results by Tang et al. [88] in Figure 4.4, for $T \simeq 1100$–1600, $\Phi = 0.5$–2 and $P = 1$–10 bar, which are perfectly reproduced by the model.

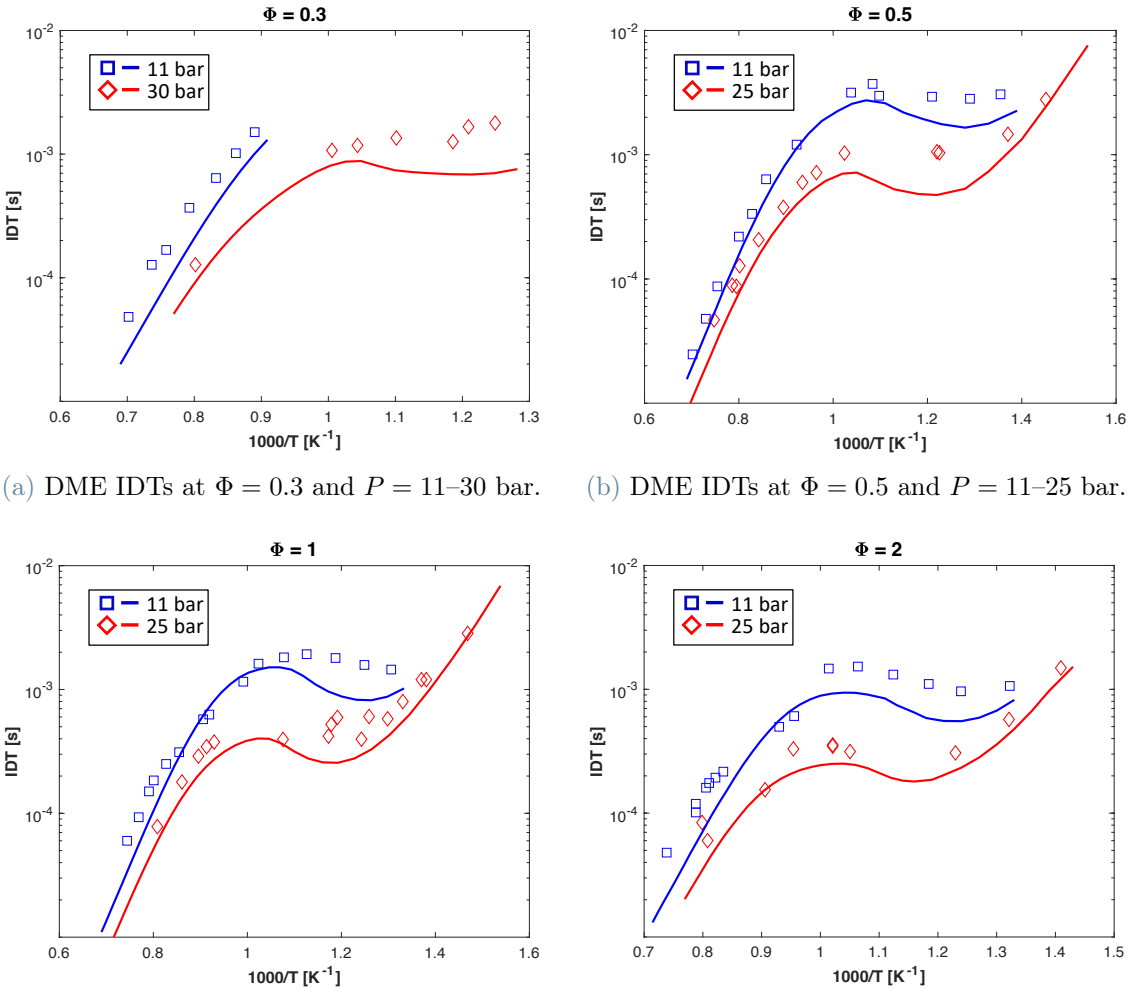

(a) DME IDTs at $\Phi = 0.3$ and $P = 11$–30 bar.

(b) DME IDTs at $\Phi = 0.5$ and $P = 11$–25 bar.

(c) DME IDTs at $\Phi = 1$ and $P = 11$–25 bar.

(d) DME IDTs at $\Phi = 2$ and $P = 11$–25 bar.

Figure 4.3: DME IDTs measured in a ST by Burke et al. [67] and model predictions. DME and O_2 are diluted in Ar as reported in the paper.

Figure 4.3 collects ST IDTs measured by Burke et al. [66] for $T \simeq 650$–1400, $\Phi = 0.3$–2 and $P = 11$–30 bar. It is evident in this case that the DME reactivity is over-estimated by a maximum factor of about 3 in the NTC area of the low temperature kinetics. The temperature at which the NTC behaviour begins increases with the equivalence ratio and the pressure. IDTs decrease for higher pressures because of the higher concentration of reactants.

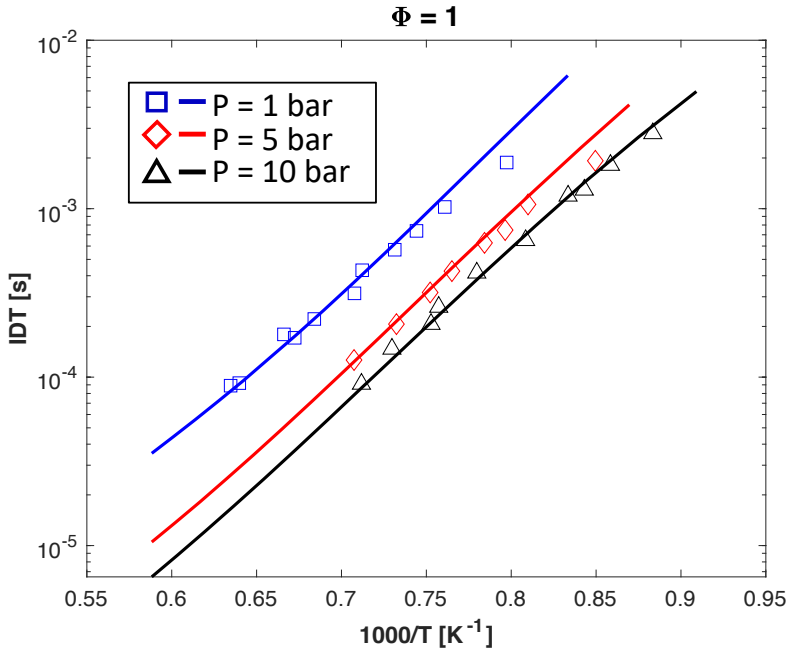

Figure 4.4: DME IDTs measured in a ST by Tang et al. [88] and model predictions. Experiments are conducted at $\Phi = 1$ and $P = 1$–10 bar. DME and O_2 are diluted in about 95% Ar.

4.1.2. Laminar Flame Speeds

LFSs has been measured at atmospheric pressure in a wide range of temperatures ($T = 298$–650 K) and equivalence ratios ($\Phi \simeq 0.7$–1.4) by Varghese et al. [89] and Zhao et al. [90]. The results are plotted together with the model predictions in Figure 4.5.

The kinetic scheme well reproduces the experimental behaviour at low T and Φ, but presents small over-estimations at $\Phi > 1.1$ for all temperatures. The difference is the largest for $T = 650$ K, where it is more than 20 cm/s and interests the whole Φ range. The LFSs for $T = 298$ K in Figure 4.5b, on the other hand, are under-estimated: this could confirm an error trend that follows the temperature, but may also be due to the different experimental setups of the two authors.

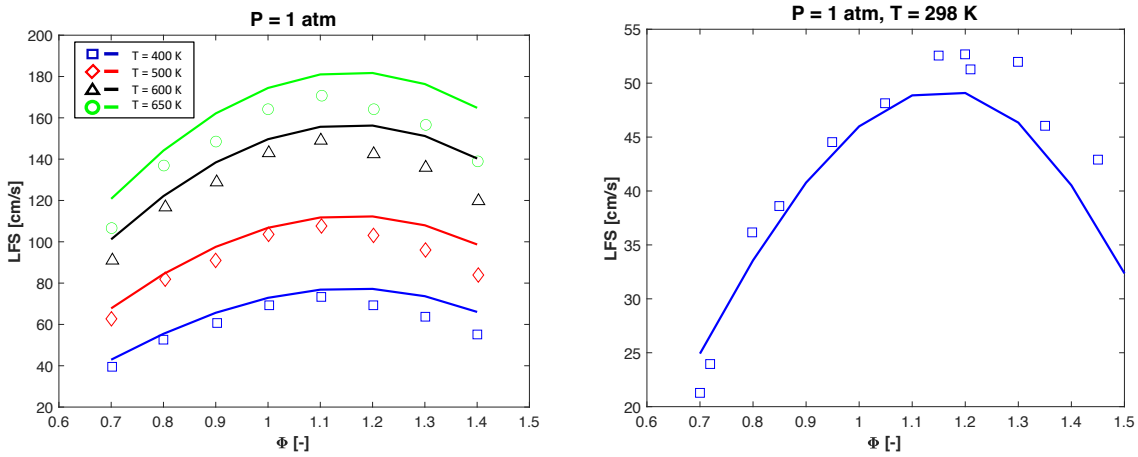

(a) DME LFSs at $T = 400$–650 K and $P = 1$ atm. (b) DME LFSs at $T = 298$ K and $P = 1$ atm.

Figure 4.5: DME LFSs measured by Varghese et al. [89] (a) and Zhao et al. [90] (b), and model predictions. DME is diluted in air.

4.1.3. Plug Flow Reactors

The species concentrations of DME combustion have been investigated in PFRs working around atmospheric pressure, in a small range of equivalence ratios ($\Phi = 0.6$–1.2) and temperatures ($T \simeq 400$–1200). The data collected by Zhang et al. [92], Wang et al. [93], Herrman et al. [94] and Guo et al. [95] are plotted respectively in Figures 4.6, 4.7, 4.8 and 4.9, together with the DME model predictions.

All the major species, such as DME, H_2, H_2O, O_2, CO and CO_2, are reproduced very well in all the cases, with only minor discrepancies at specific temperatures. Other species, like CH_3OCHO and CH_2O, present bigger differences between experiments and simulations in the whole range of conditions (Figures 4.7h, 4.8g, 4.8h and 4.9g). It must be considered, though, that the measured uncertainties for those species are also larger. H_2O_2 was only measured by Guo et al. (Figure 4.9c) and it is slightly over-predicted by the simulation.

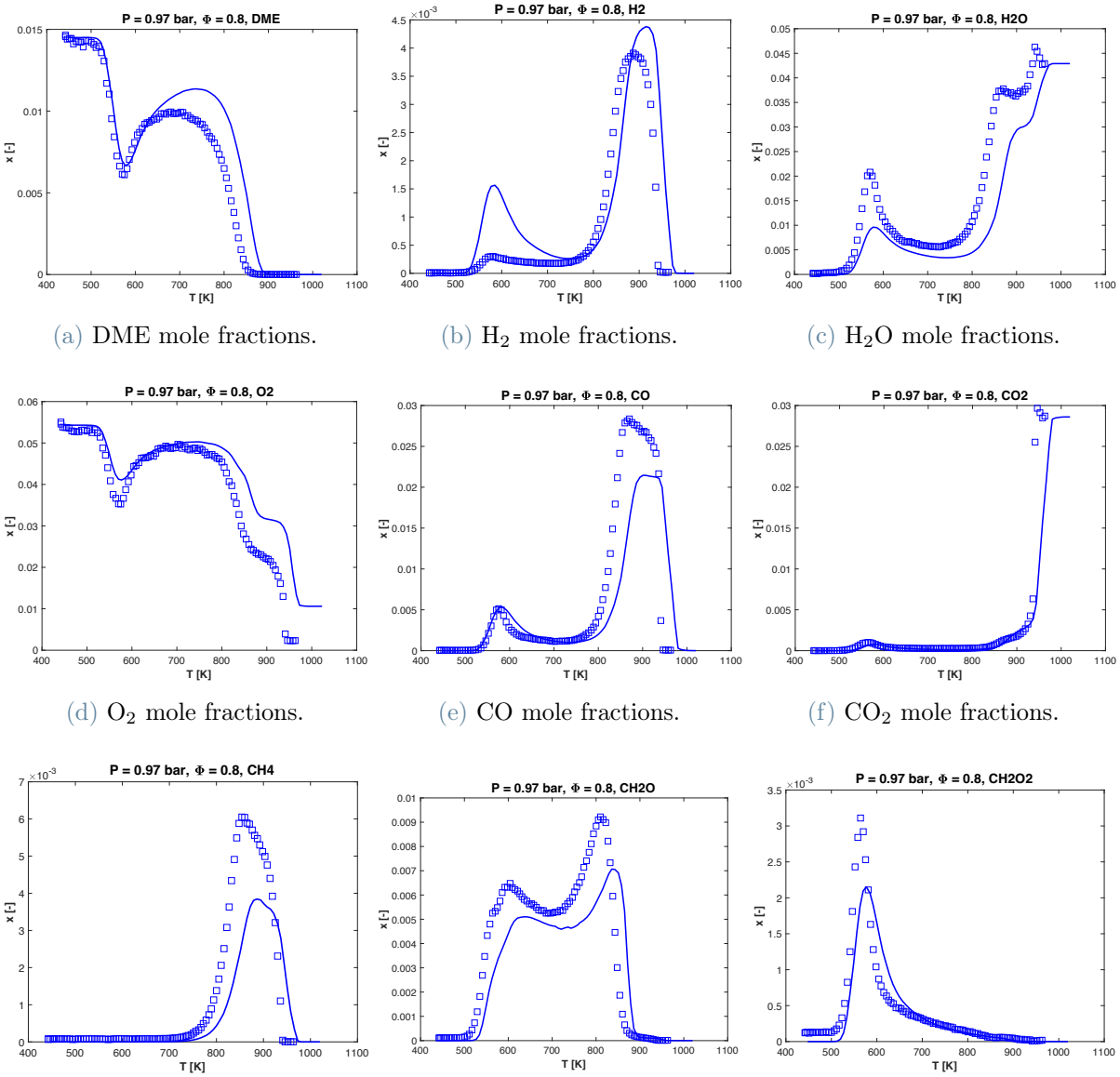

(a) DME mole fractions. (b) H_2 mole fractions. (c) H_2O mole fractions.

(d) O_2 mole fractions. (e) CO mole fractions. (f) CO_2 mole fractions.

(g) CH_4 mole fractions. (h) CH_2O mole fractions. (i) CH_2O_2 mole fractions.

Figure 4.6: Species mole fractions of DME combustion measured in a PFR by Zhang et al. [92] and model predictions. DME and O_2 are diluted in 93% Ar. Experiments are carried out at $\Phi = 0.8$ and $P = 0.97$ bar.

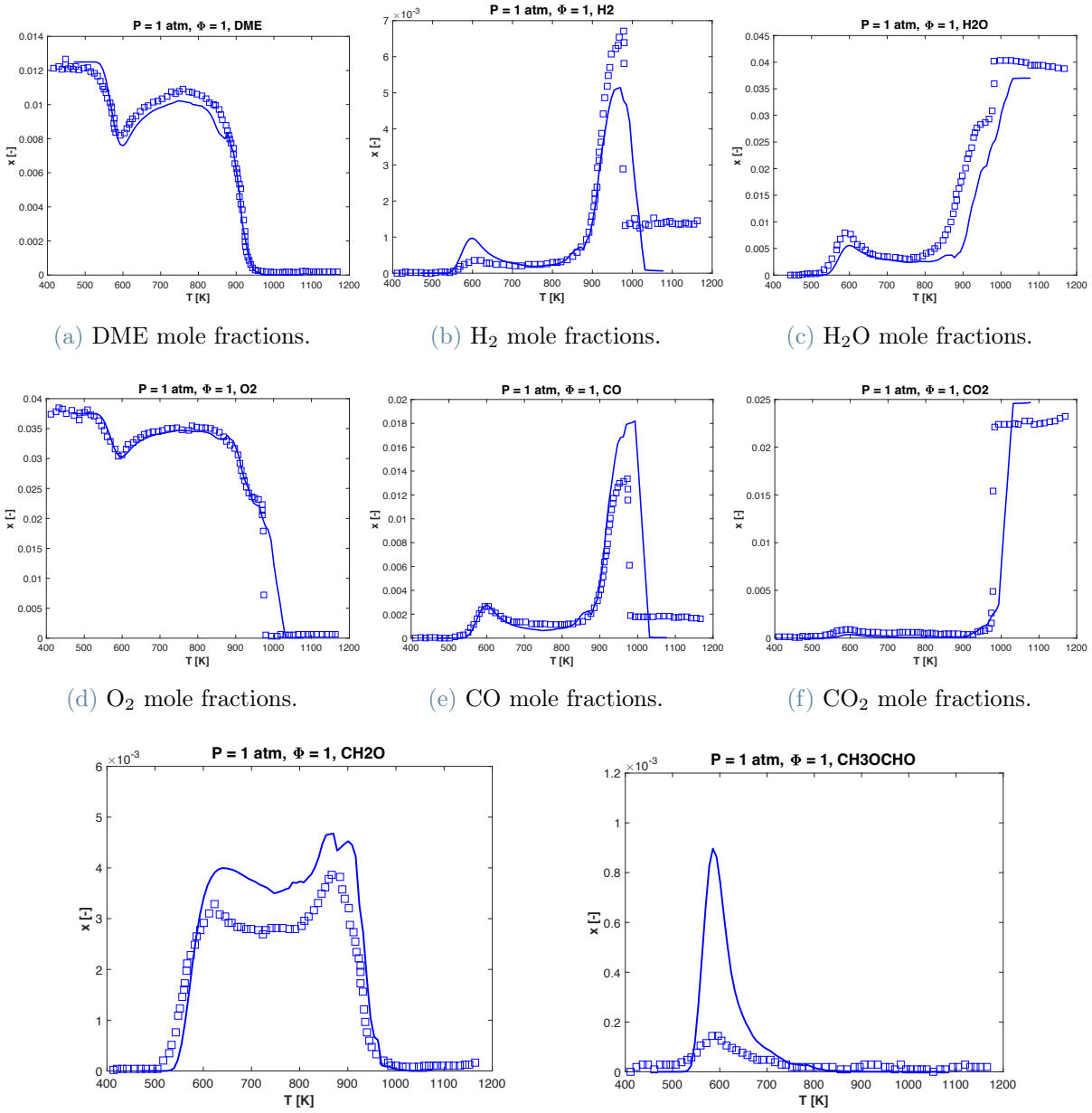

(a) DME mole fractions. (b) H_2 mole fractions. (c) H_2O mole fractions.

(d) O_2 mole fractions. (e) CO mole fractions. (f) CO_2 mole fractions.

(g) CH_2O mole fractions. (h) CH_3OCHO mole fractions.

Figure 4.7: Species mole fractions of DME combustion measured in a PFR by Wang et al. [93] and model predictions. DME and O_2 are diluted in 95% Ar. Experiments are carried out at $\Phi = 1$ and $P = 1$ atm.

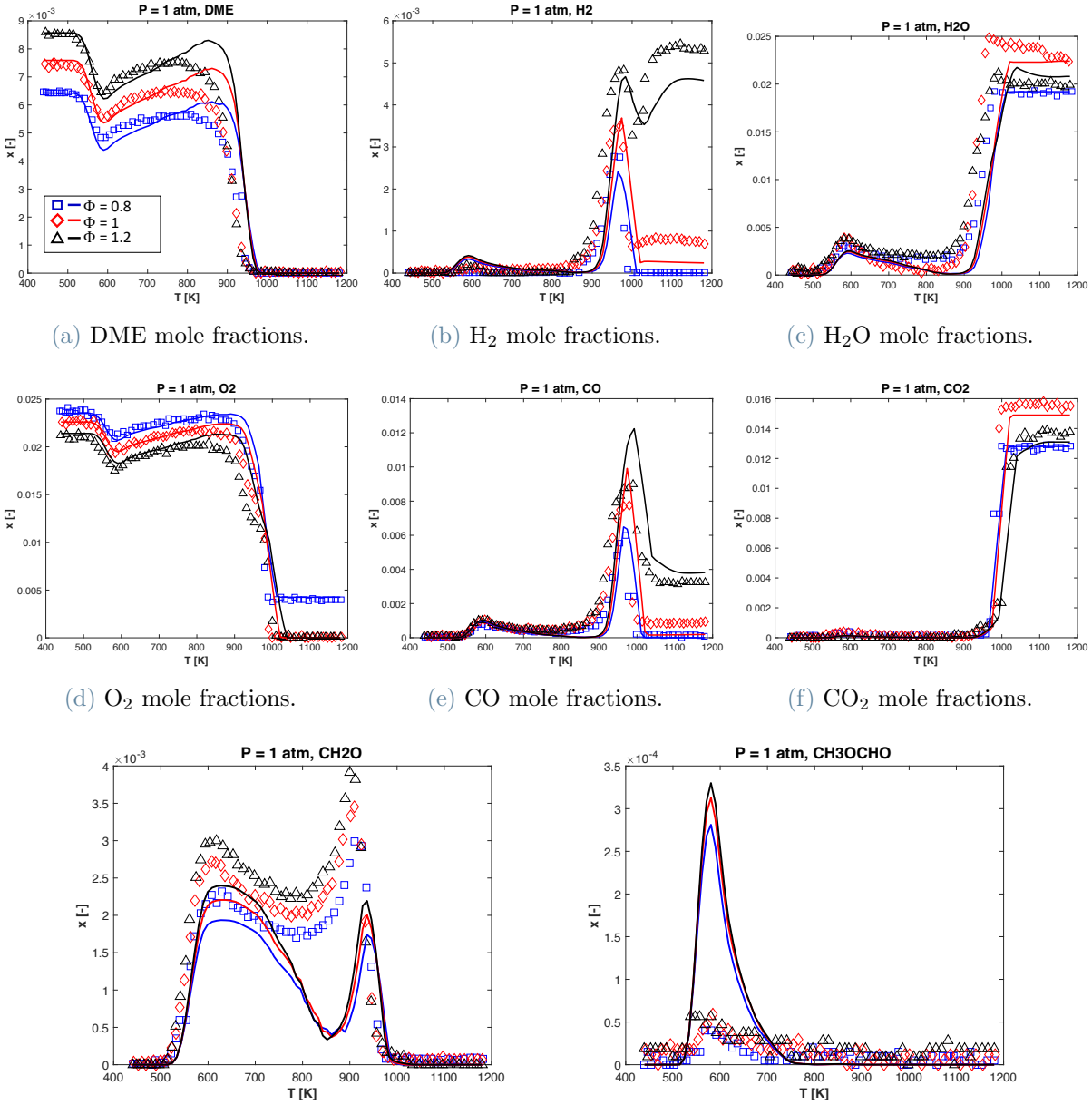

(a) DME mole fractions. (b) H_2 mole fractions. (c) H_2O mole fractions.

(d) O_2 mole fractions. (e) CO mole fractions. (f) CO_2 mole fractions.

(g) CH_2O mole fractions. (h) CH_3OCHO mole fractions.

Figure 4.8: Species mole fractions of DME combustion measured in a PFR by Herrman et al. [94] and model predictions. DME and O_2 are diluted in about 86% Ar. Experiments are carried out at $\Phi = 0.8$–1.2 and $P = 1$ atm.

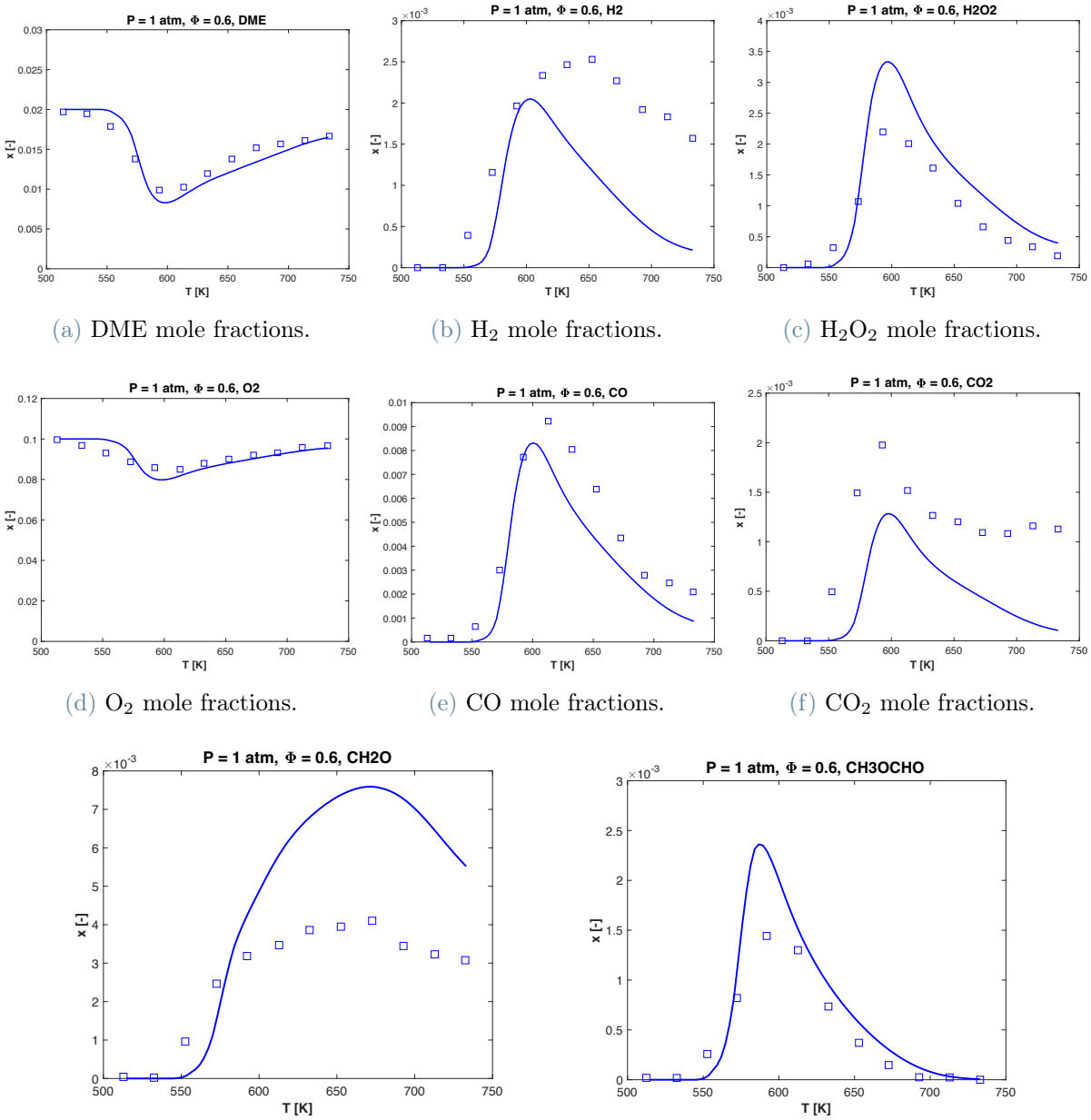

(a) DME mole fractions. (b) H_2 mole fractions. (c) H_2O_2 mole fractions.

(d) O_2 mole fractions. (e) CO mole fractions. (f) CO_2 mole fractions.

(g) CH_2O mole fractions. (h) CH_3OCHO mole fractions.

Figure 4.9: Species mole fractions of DME combustion measured in a PFR by Guo et al. [95] and model predictions. DME and O_2 are diluted in 88% He. Experiments are carried out at $\Phi = 0.6$ and $P = 1$ atm.

4.1.4. Jet Stirred Reactors

The concentrations of the DME combustion products and intermediates have also been measured in a JSR by Moshammer et al. [91] and collected in Figure 4.10. The reactor operated in a range of $T \simeq 500$–1000, in lean conditions ($\Phi = 0.35$) and near atmospheric pressure ($P = 0.933$ bar), and Ar was adopted as diluent.

DME reactivity is over-predicted for 500 K $< T <$ 700 K (Figure 4.10a), causing lower O_2 (Figure 4.10d) and higher H_2O, CO and CO_2 concentrations (Figures 4.10b, 4.10e and 4.10f). Also the higher presence of some intermediates, like DME-OQOOH, CH_3OCHO and CH_3O_2H (Figures 4.10i, 4.10j and 4.10k), confirm the reactivity error. H_2O_2 concentration (Figure 4.10c) is again over-predicted, reflecting the PFR results.

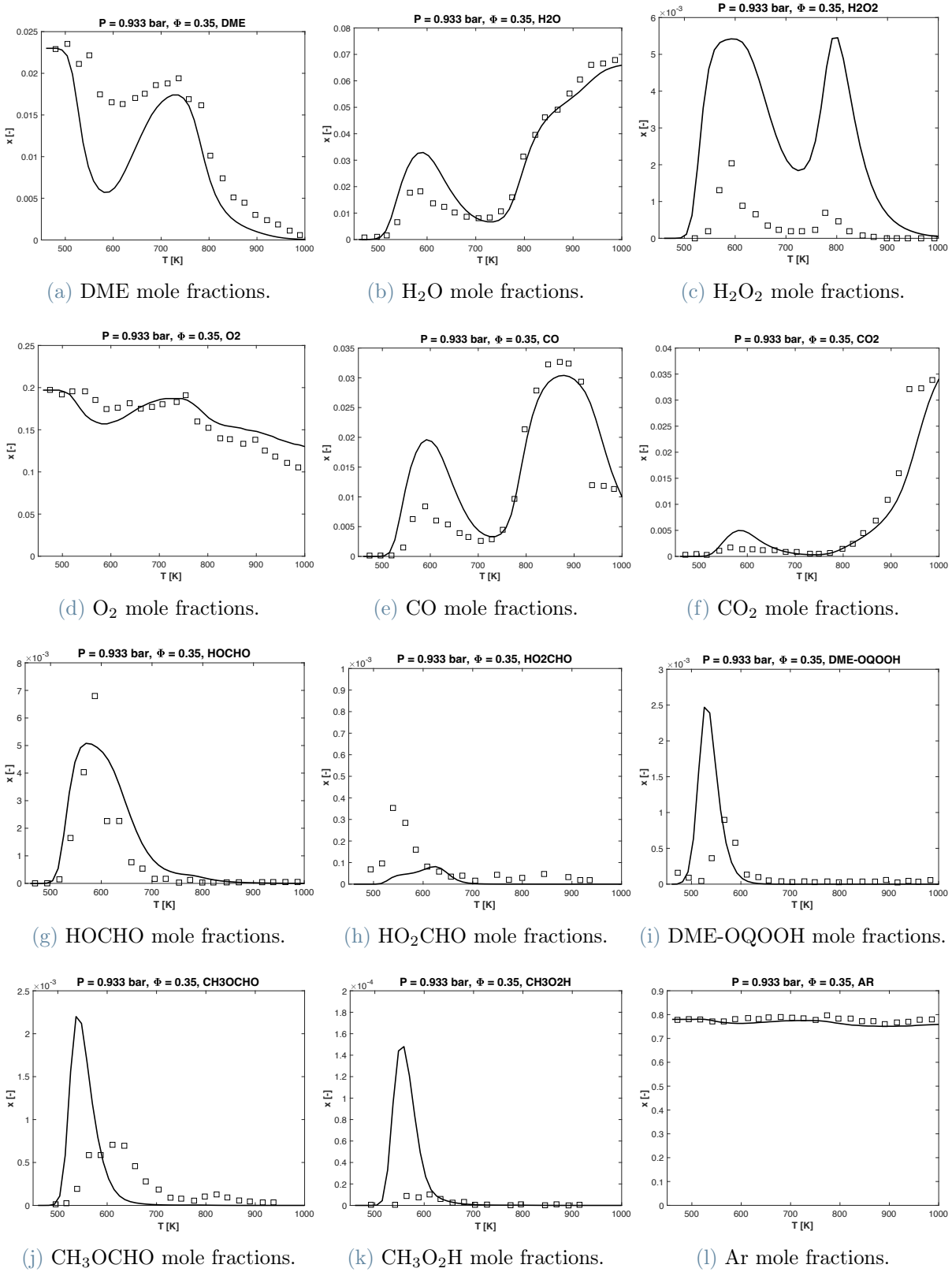

(a) DME mole fractions. (b) H_2O mole fractions. (c) H_2O_2 mole fractions.

(d) O_2 mole fractions. (e) CO mole fractions. (f) CO_2 mole fractions.

(g) HOCHO mole fractions. (h) HO_2CHO mole fractions. (i) DME-OQOOH mole fractions.

(j) CH_3OCHO mole fractions. (k) CH_3O_2H mole fractions. (l) Ar mole fractions.

Figure 4.10: Species mole fractions of DME combustion measured in a JSR by Moshammer et al. [91] and model predictions. DME and O_2 are diluted in 78% Ar. Experiments are carried out at $\Phi = 0.35$ and $P = 0.933$ bar.

4.1.5. Conclusions

The DME sub-mechanism adopted from Burke et al. [66], implemented in the mechanism and modified as explained in Chapter 2, well represents the data collected. Only minor differences are present but, considering that the experimental uncertainties are not reported, it cannot be concluded that errors in the estimation of the kinetic parameters are present. On the contrary, the consolidated nature of the mechanism suggests that the model is reliable. Since DME validation was only performed in order to start the OME_{1-4} lumping from a solid base, and its kinetics lies outside the scope of this Thesis, it was not investigated further. For the same reason, the curve matching indices were not evaluated for DME.

4.2. DMM

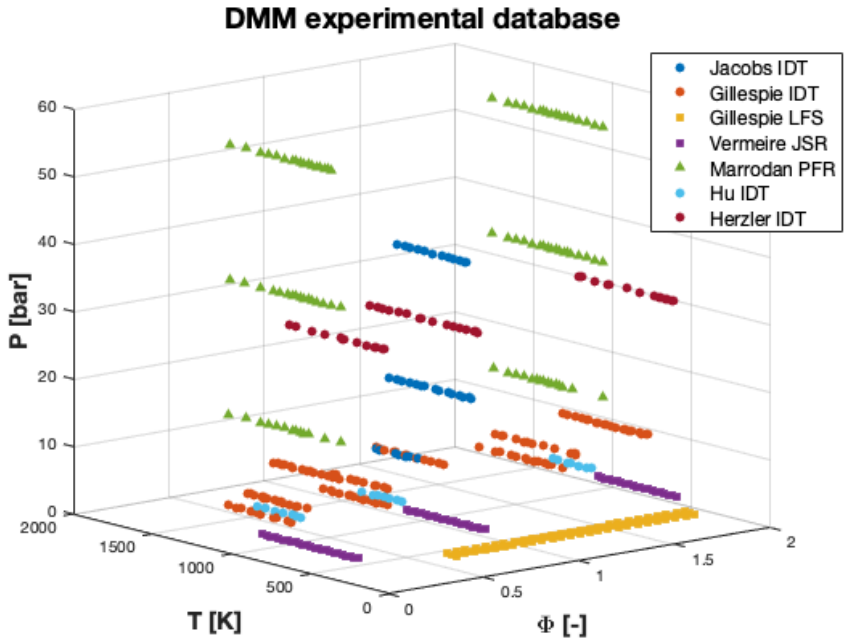

Figure 4.11: DMM experimental database.

The experimental database of DMM covers a wide range of operating conditions and it is schematized in Figure 4.11. It counts 29 datasets, including IDTs in STs [51, 82, 96, 97], LFSs [82] and speciations in PFRs [98] and JSRs [50]. Among those, 11 experimental datasets, specified in Chapter 3, were selected as optimization targets, while the remaining 18 served for performance validation only.

4.2.1. Ignition Delay Times

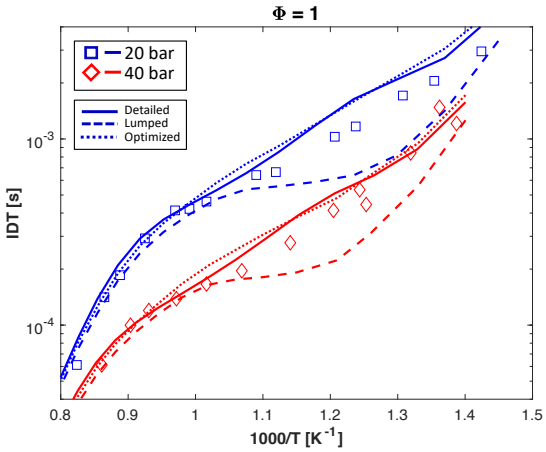

(a) DMM IDTs at $\Phi = 1$ and $P = 20$–40 bar. DMM is diluted in air.

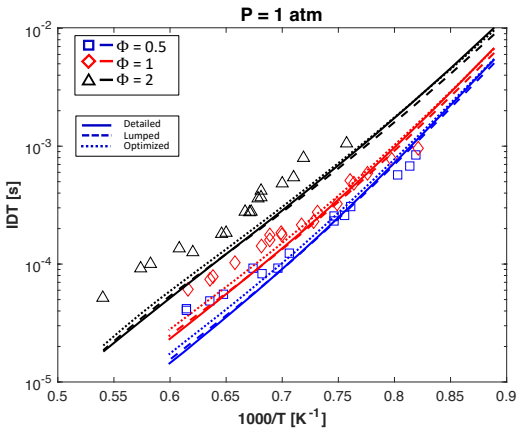

(b) DMM IDTs at $\Phi = 0.5$–2 and $P = 1$ atm. DMM and O_2 are diluted in 99% Ar.

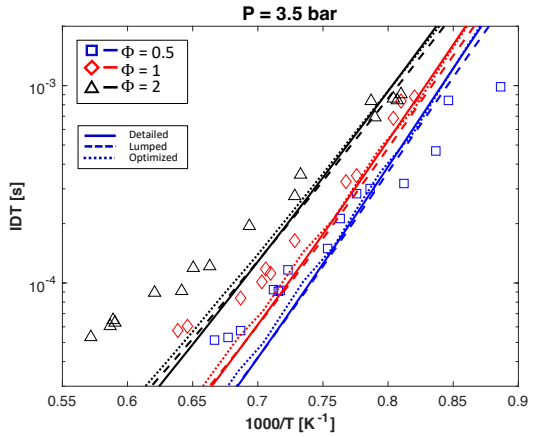

(c) DMM IDTs at $\Phi = 0.5$–2 and $P = 3.5$ bar. DMM and O_2 are diluted in 99% Ar.

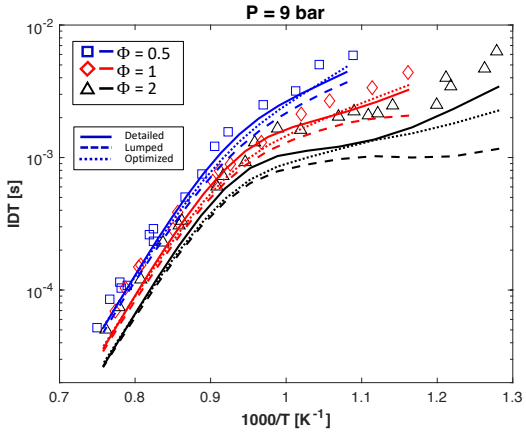

(d) DMM IDTs at $\Phi = 0.5$–2 and $P = 9$ bar. DMM is diluted in air.

Figure 4.12: DMM IDTs measured in a ST by Jacobs et al. [51] (a) and Gillespie [82] (b), (c) and (d), and model predictions.

Gillespie [82] collected DMM autoignition data for medium- and high-temperature combustion ($T \simeq 750$–1800 K) for $\Phi = 0.5 - 2$ and $P \simeq 1 - 9$ bar. Experiments at higher pressures ($P = 20$–40 bar, lower temperatures ($T \simeq 700$–1200) and stoichiometric conditions were conducted by Jacobs et al. [51]. Datasets from both works are reported in Figure 4.12.

From the low-pressure results by Gillespie (Figures 4.12b and 4.12c), it appears that the high-temperature reactivity is over-predicted, predominantly for rich conditions. This

is common to all three mechanisms, since the lumping process, and consequently the optimization, mainly affected the low-temperature kinetics. Similarly, also the NTC area at $P = 9$ bar (Figure 4.12d) is too reactive, but in this case the error is even increased in the lumped mechanism and reduced again in the optimized one. This remarks the impact of lumping in the low- and medium-temperature chemistry, and it is confirmed by the high-pressure, stoichiometric datasets by Jacobs et al. in Figure 4.12a. The gap between lumped simulations and experiments is completely closed after the optimization is performed.

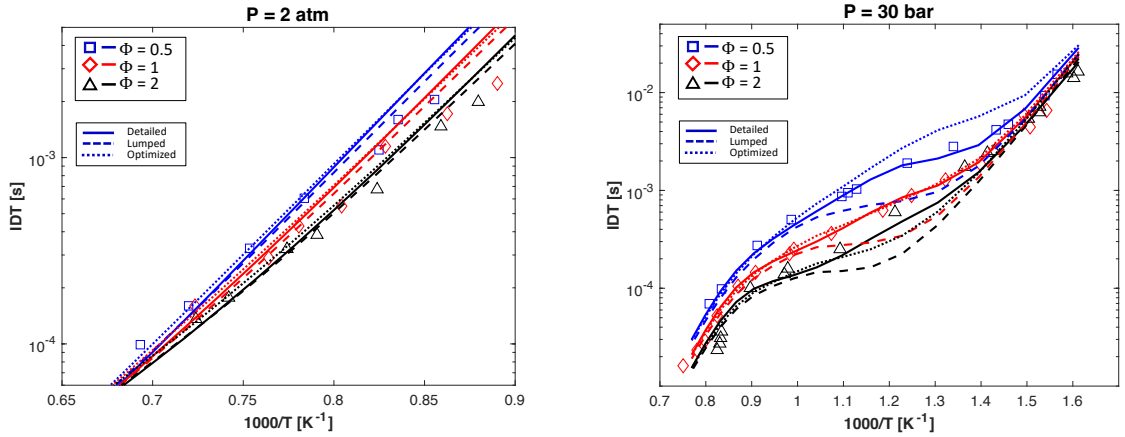

(a) DMM IDTs at $\Phi = 0.5$–2 and $P = 2$ atm. DMM and O_2 are diluted in about 95% Ar.

(b) DMM IDTs at $\Phi = 0.5$–2 and $P = 30$ bar. DMM is diluted in air.

Figure 4.13: DMM IDTs measured in a ST by Hu et al. [96] (a) and Herzler et al. [97] (b), and model predictions.

Figure 4.13 reports the results of the ST experiments performed by Hu et al. [96] and Herzler et al. [97], respectively at $T \simeq 1100$–1400 K and $P = 2$ atm, and $T \simeq 600$–1400 and $P = 30$ bar. Both authors investigated lean ($\Phi = 0.5$), stoichiometric ($\Phi = 1$) and rich ($\Phi = 2$) conditions.

It can be seen from Figure 4.13a that, as already stated, high-temperature reactivity is not affected by the lumping process, and the already good predictions of the initial model are retained in the other two. Conversely, the NTC behaviour in Figure 4.13b is enhanced in the lumped chemistry, and only partially recovers after optimization. Specifically, the optimized mechanism perfectly reproduces experiments in stoichiometric conditions, while under- and over-predicts IDTs respectively in rich and lean mixtures. The reason is that datasets by Herzler et al. were not adopted as optimization targets, hence the performances only improved indirectly by reconciling the IDTs by Jacobs et al [51].

4.2.2. Laminar Flame Speeds

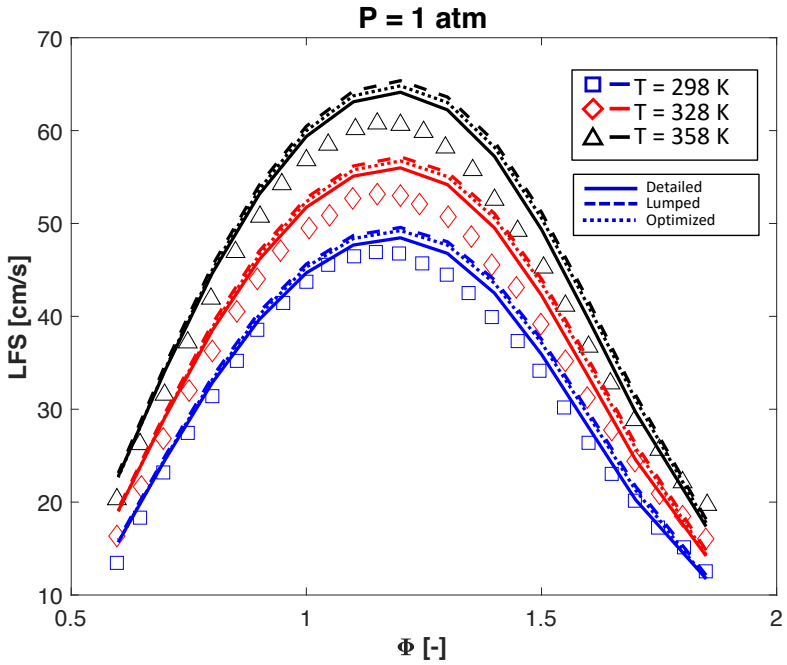

Figure 4.14: DMM LFSs measured by Gillespie [82] and models predictions. DMM is diluted in air. Experiments are carried out at $P = 1$ atm and $T = 298$–358 K.

The only LFS data available for DMM have been measured by Gillespie [82] at atmospheric pressure at three different temperatures (298 K, 328 K and 358 K), in an equivalence ratio range of $\Phi = 0.6$–1.8.

The results from the detailed mechanism well reproduce the experiments, only with a slight over-prediction increasing with temperature, in correspondence to the maximum velocity at $\Phi \simeq 1.2$. DMM LFS is controlled only by C_1-C_3 reactions, and for this reason the lumping process did not modify the model behaviour. Due to the good accordance between model and experiments, an optimization with this dataset as target was not necessary. It can be seen that neither the optimization on IDTs and speciations modified the LFS in a relevant way.

4.2.3. Plug Flow Reactors

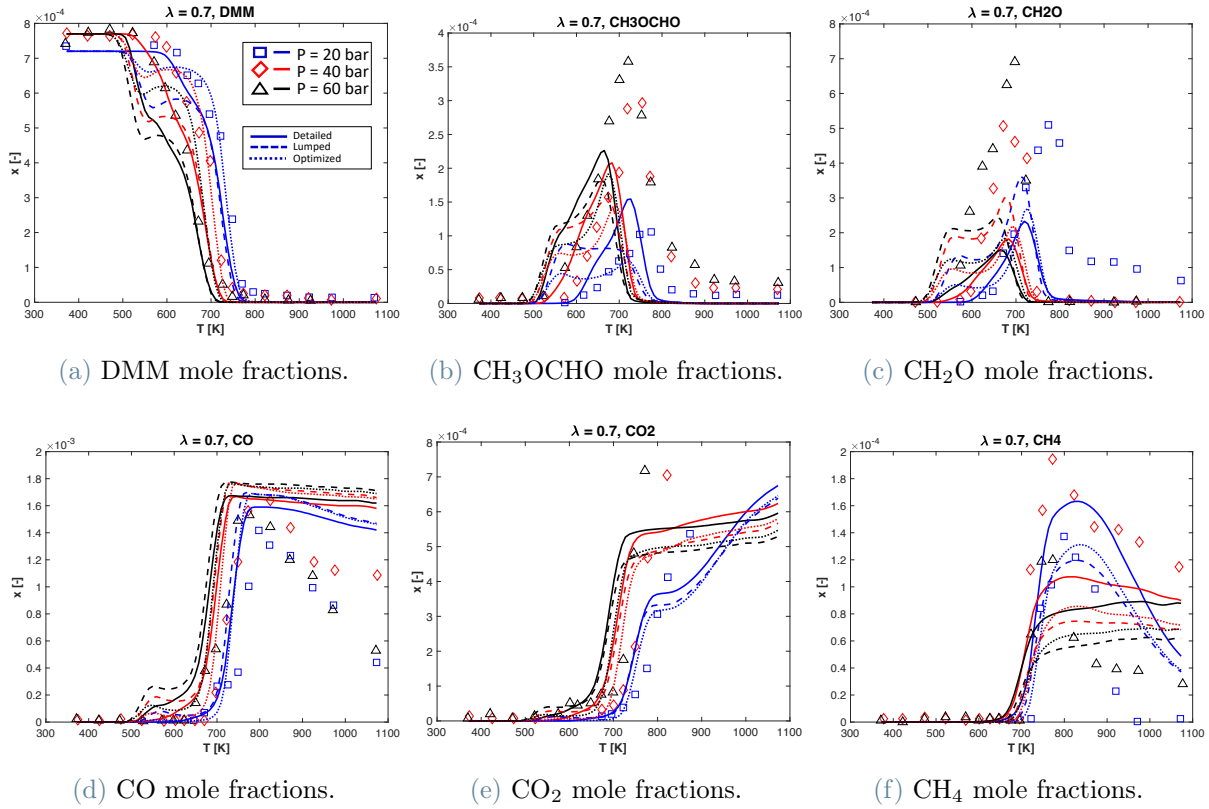

(a) DMM mole fractions. (b) CH_3OCHO mole fractions. (c) CH_2O mole fractions.

(d) CO mole fractions. (e) CO_2 mole fractions. (f) CH_4 mole fractions.

Figure 4.15: Species mole fractions of DMM combustion measured in a PFR by Marrodan et al. [98] and model predictions. DMM and O_2 are diluted in N_2 as reported in the paper. Experiments are carried out at $P = 20$–60 bar.

Figures 4.15 and 4.16 collect the species concentrations measured in a PFR by Marrodan et al. [98], respectively at $\lambda = 0.7$ and $\lambda = 20$. The experiments were carried out in a range of pressures $P = 20$–60 bar and temperatures $T = 800$–1100 K.

The DMM mole fraction is well represented by all three mechanisms, despite its reactivity being slightly exaggerated. This can be seen especially for high P and λ. The optimization performed on the JSR speciations has a positive impact also on PFR results, since the final model is better than the lumped one. CO and CO_2 present some discrepancies, especially at $T > 700$ K: the over-prediction of CO and the under-prediction of CO_2 suggest an incomplete combustion in the models.

The remaining species (CH_3OCHO, CH_2O and CH_4) were already poorly reproduced by the detailed model. The lumping process inevitably modified the simulation results, with no control on these combustion intermediate: it was an inevitable trade off to retain

accuracy for other relevant species. Since the optimization on the JSR was performed only on the DMM mole fraction, the final mechanism in some cases improved (CH_3OCHO and CH_4) and in others worsened (CH_2O) the performances.

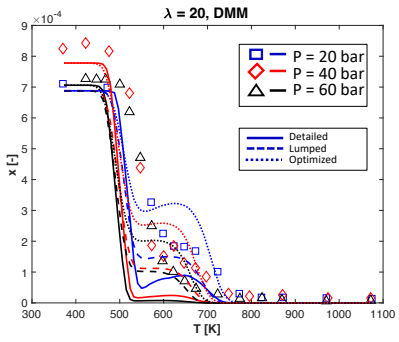

(a) DMM mole fractions.

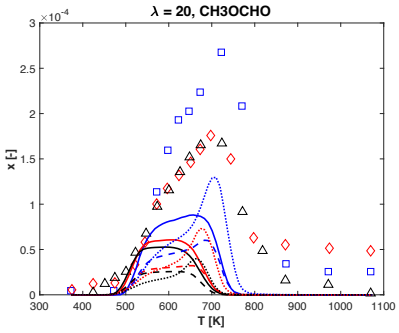

(b) CH_3OCHO mole fractions.

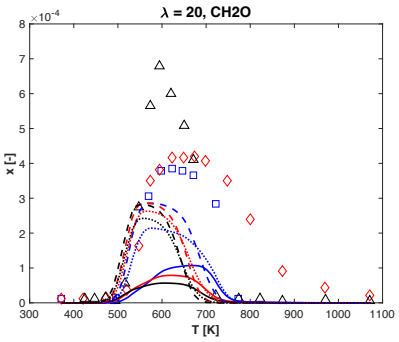

(c) CH_2O mole fractions.

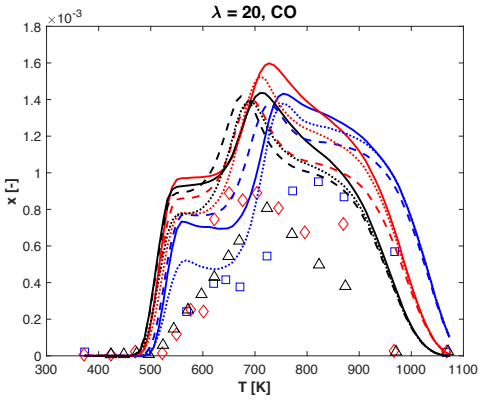

(d) CO mole fractions.

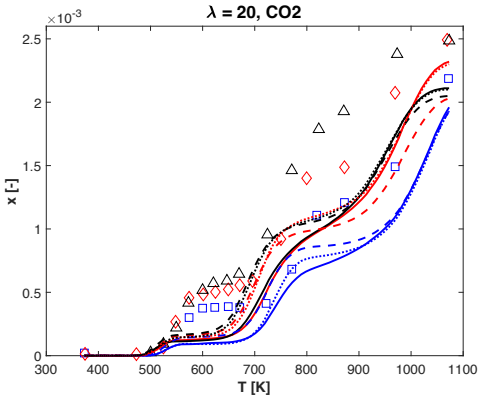

(e) CO_2 mole fractions.

Figure 4.16: Species mole fractions of DMM combustion measured in a PFR by Marrodan et al. [98] and model predictions. DMM and O_2 are diluted in N_2 as reported in the paper. Experiments are carried out at $P = 20$–60 bar.

4.2.4. Jet Stirred Reactors

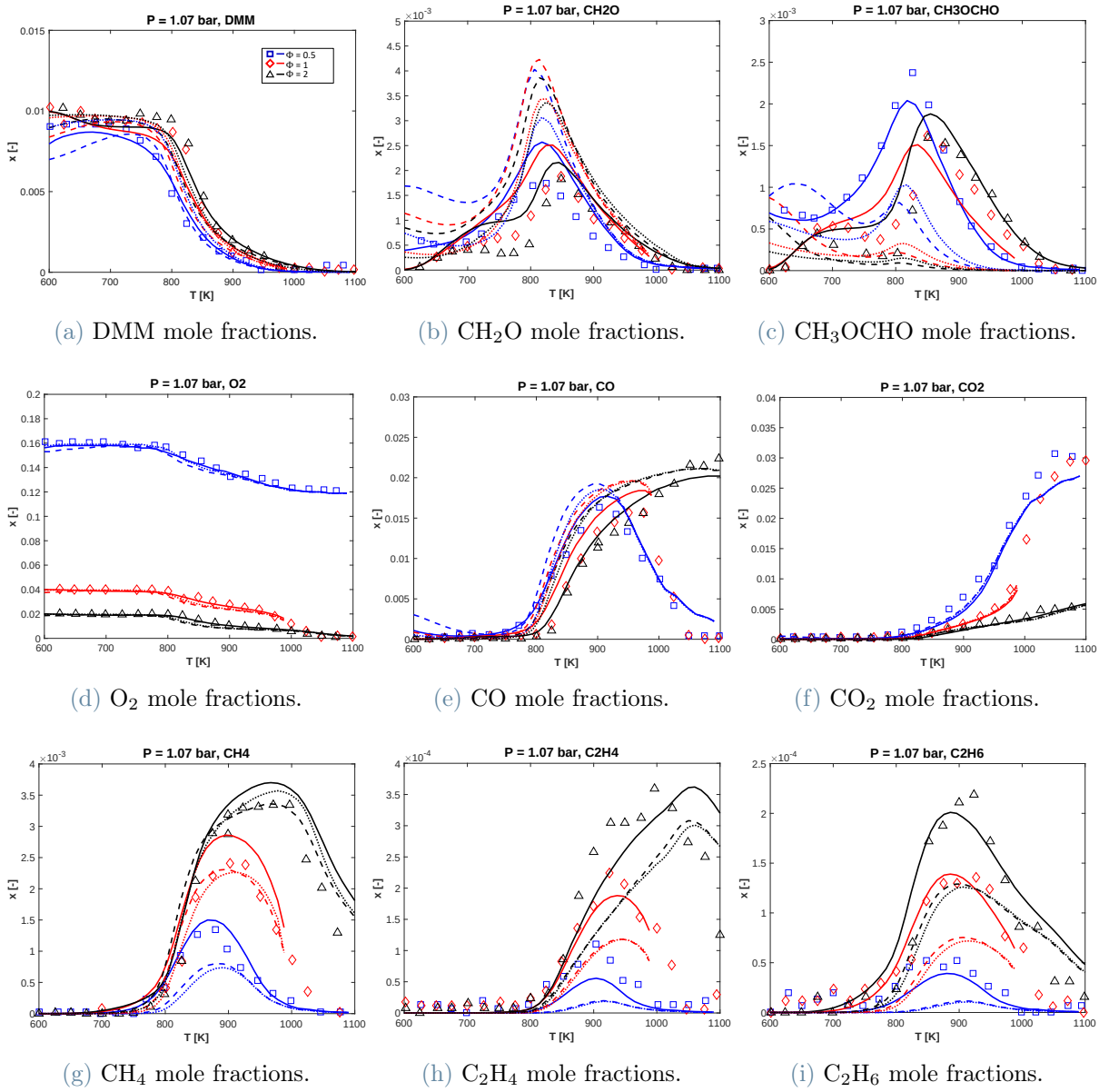

(a) DMM mole fractions. (b) CH_2O mole fractions. (c) CH_3OCHO mole fractions.

(d) O_2 mole fractions. (e) CO mole fractions. (f) CO_2 mole fractions.

(g) CH_4 mole fractions. (h) C_2H_4 mole fractions. (i) C_2H_6 mole fractions.

Figure 4.17: Species mole fractions of DMM combustion measured in a JSR by Vermeire et al. [50] and model predictions. DMM is diluted in 99% O_2 and Ar. Experiments are carried out at $\Phi = 0.5$–2 and $P = 1.07$ bar.

Species concentrations measured by Vermeire et al. [50] are reported in Figure 4.17 with their respective simulations. The JSR operated near atmospheric pressure at $T =$ 600–1100 and $\Phi = 0.5$–2. Simulations for $\Phi = 1$ are represented only in the range $T < 1000$ K, because no steady-state solution was found for higher temperatures [83].

Mole fractions of O_2, CO and CO_2 are very well reproduced by every model, whereas CH_4, C_2H_4 and C_2H_6 present minor errors, especially for the lumped and optimized mechanisms. Also the DMM data are well predicted, and the small errors of the lumped kinetics are completely removed in the optimization procedure. Indirect effects of the DMM optimization are evident also on the CH_2O and CH_3OCHO profiles, whose optimized results are better than the ones from the lumped model, but still not very accurate. Optimizing the mechanism using also these intermediates as targets was not an option, since DMM and other species predictions heavily worsened.

4.2.5. Conclusions

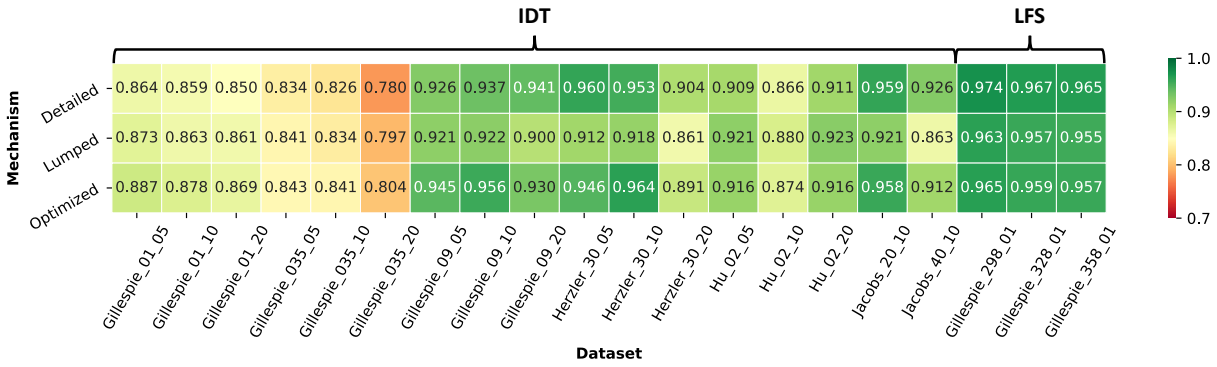

Figure 4.18: Heat map summarizing the CM indices of DMM IDTs and LFSs.

The heat map in Figure 4.18 collects the CM scores evaluated for IDTs and LFSs of DMM, organized by author and mechanism, in order to better compare their performances.

LFSs high indices confirm that the detailed kinetics very well reproduce the experimental results. Moreover, neither the lumping nor the optimization procedures had a big impact on the predictions, since the controlling reactions were not modified.

IDTs predicted by the detailed mechanism are very similar to the experiments at medium- and high-pressure conditions by Gillespie, Herzler et al. and Hu et al. On the contrary, the scores are lower for the low-pressure simulations of the data by Gillespie and Hu et al. This explains why the lumped mechanism, enhancing the low-temperature reactivity, brought about a general worsening for the former ones and an improvement for the latter ones. Nonetheless, almost all the indices of the optimized mechanism are higher than the ones of the detailed kinetics, suggesting that the adopted approach was succesful.

4.3. OME_2

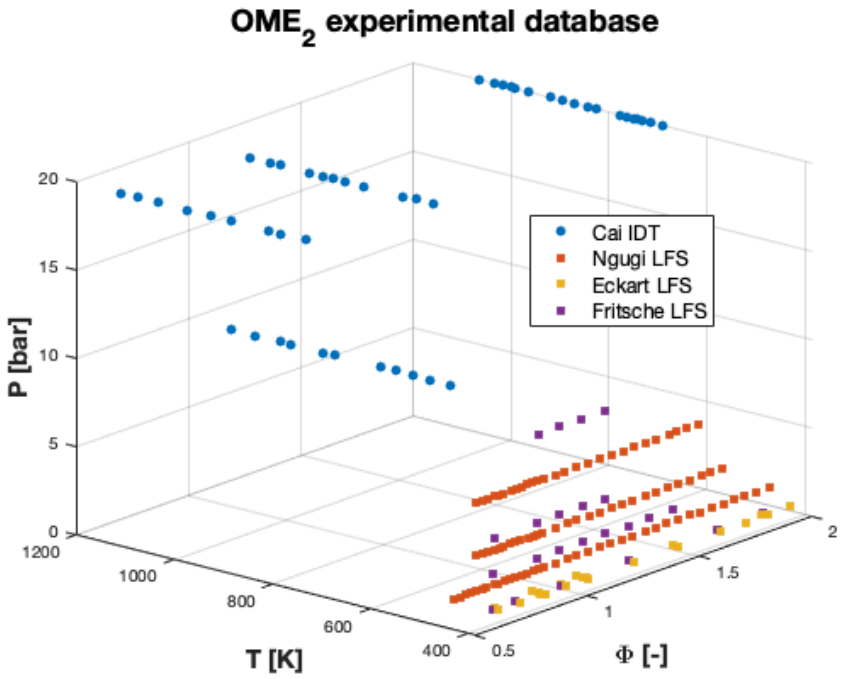

Figure 4.19: OME_2 experimental database.

The experimental database of OME_2 consists of 15 datasets, represented in Figure 4.19. It only includes IDTs measured in STs [58] and LFSs [84, 85, 99], since no speciations are available in literature yet. 11 of those datasets, listed in Chapter 3, served as optimization targets, while the remaining four contributed only to the final validation.

4.3.1. Ignition Delay Times

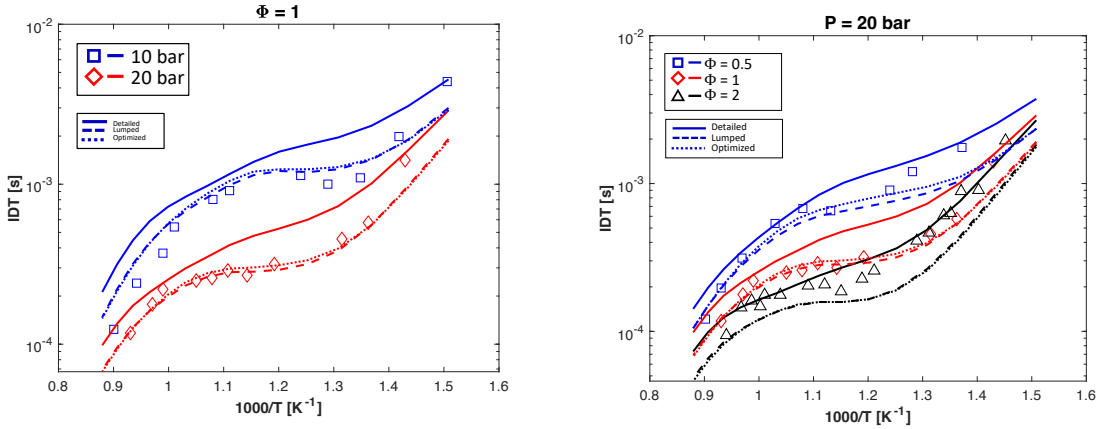

(a) OME_2 IDTs at $\Phi = 1$ and $P = 10$–20 bar. (b) OME_2 IDTs at $\Phi = 0.5$–2 and $P = 20$ bar.

Figure 4.20: OME_2 IDTs measured in a ST by Cai et al. [58] and models predictions. OME_2 is diluted in air.

OME_2 IDTs were measured by Cai et al. [58] in a ST at $T \simeq 650$–1100, $\Phi = 0.5$–2 and $P = 10$–20 bar. The results are collected in Figure 4.20 together with the models predictions.

The original detailed mechanism over-estimates IDTs in most of the operating conditions of interest, and does not present an NTC effect as strong as the one of the experimental data. The lumping procedure resulted in a general acceleration of the kinetics and in a more evident NTC, mostly improving the accuracy of the model. This cannot be said for $\Phi = 2$ and $P = 20$ bar, where the detailed model already well represented the experiments, and the lumped mechanism is too fast. The optimization, because of the already very good results, did not improve them much further.

4.3.2. Laminar Flame Speeds

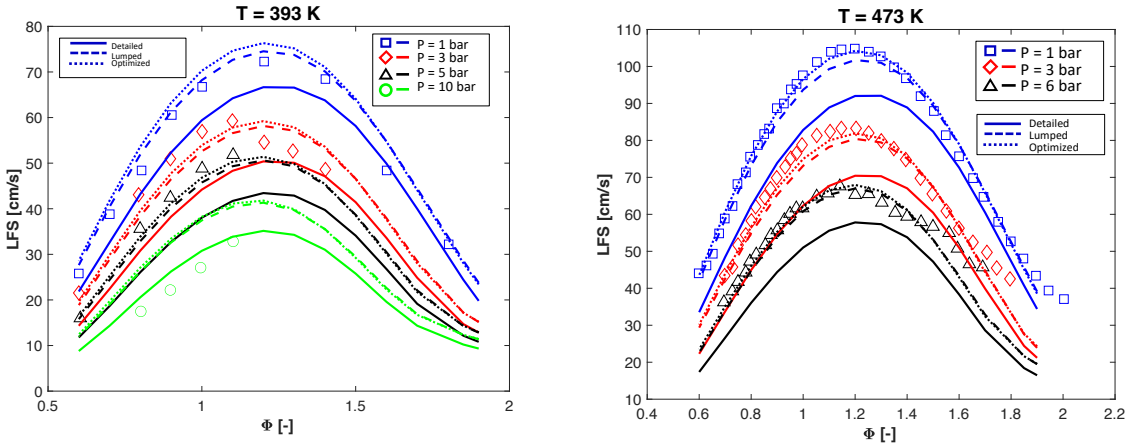

(a) OME_2 LFSs at $T = 393$ K and $P = 1$–10 bar. (b) OME_2 LFSs at $T = 473$ K and $P = 1$–6 bar.

Figure 4.21: OME_2 LFSs measured by Fritsche et al. [85] (a) and Ngugi et al. [84] (b), and models predictions. OME_2 is diluted in air.

OME_2 burning velocity was largely investigated by Fritsche et al. [85], Ngugi et al. [84] and Eckart et al. [99], in the following set of conditions: $T = 383$–473 K, $\Phi = 0.6$–2 and $P = 1$–10 bar.

Figure 4.21 represents the data by Fritsche et al. and Ngugi et al., compared with the results from the numerical simulations. The detailed model under-estimates the LFSs by up to 20 cm/s in every case, except for $T = 393$ K and $P = 10$ bar, where it predicts the experimental data more accurately. An evident and unexpected acceleration of the lumped mechanism can be noticed, leading to an improvement of all the predictions excluding the 10 bar dataset, now over-estimated.

The LFS is controlled mainly by the C_1-C_3 chemistry: this is the reason why the lumped kinetics was not expected to change behaviour significantly. However, analyses of the species profiles in the flame allowed to discover that, even though CH_3 predictions of the lumped mechanism are similar to the ones of the detailed model, a higher mole fraction of H is produced in the peak, as demonstrated by Figure 4.22. The larger amount of H in the lumped model (about 20% more) could indeed be responsible for the faster flame and required further study, since concentrations of small radicals, such as H and CH_3, can affect the burning speed.

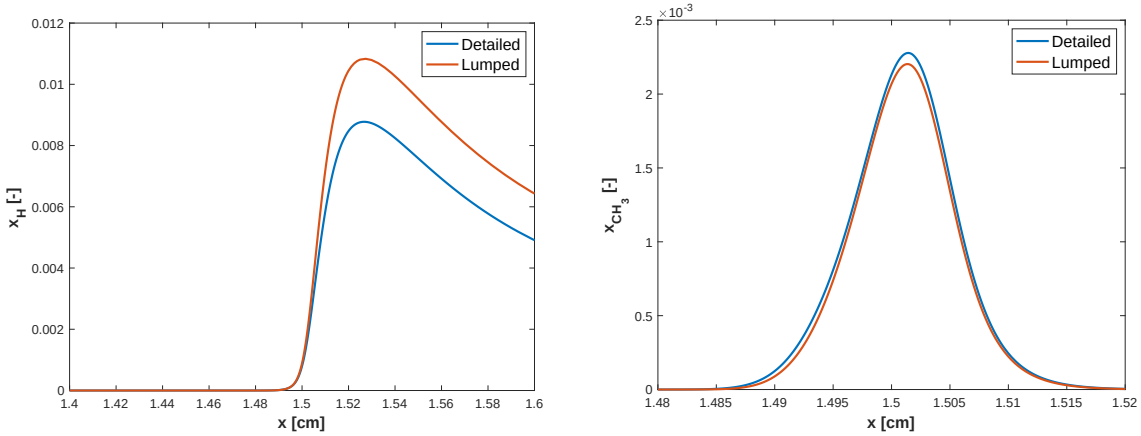

(a) H mole fractions. (b) CH_3 mole fractions.

Figure 4.22: Mole fractions of H (a) and CH_3 (b), simulated at $T = 473$ K, $\Phi = 1$ and $P = 1$ bar, using the detailed and lumped mechanisms. Only the middle section of the domain is reported, to highlight differences in the flame peak.

Sensitivity analyses were then performed in the middle section of the flame ($x \simeq 1.5$ cm) on both H mole fraction and mass flow-rate. The sensitive reactions identified by the two analyses, reported in Table 4.1, revealed the important role of the decompositions of the OME_2 and DMM alkyl radicals, and of the DMM ketones. These reactions were involved in the lumping procedure, justifying the differences between the two mechanisms.

Mass flow-rate sensitivity	H mole fraction sensitivity
OME2-R⇒CH2O+DMM-R	OME2-R⇒CH3+DMM-ket
OME2-R⇒CH3+DMM-ket	H+OME2⇒H2+OME2-R
DMM-ket⇒CH3O+CH2OCHO	OH+OME2⇒H2O+OME2-R
DMM-ket⇒CH3+OCH2OCHO	DMM-R⇒CH2O+CH3OCH2
H+DMM-R⇒DMM	DMM-ket⇒CH3+OCH2OCHO
DMM-R⇒CH2O+CH3OCH2	OME2-R⇒CH2O+DMM-R
OH+OME2⇒H2O+OME2-R	DMM-ket⇒CH3O+CH2OCHO

Table 4.1: Sensitive reactions for mass flow-rate (left) and H mole fraction (right) in LFS. Analyses were carried out at $T = 473$ K, $\Phi = 1$ and $P = 1$ bar, for $x = 1.52$ cm. Only the reactions belonging to the OME_{1-4} sub-mechanisms are reported, in order of descending sensitivity coefficient.

The optimized mechanism, finally, reflects the results of the lumped one, maintaining its good performances. Also the 10 bar dataset in Figure 4.21b retains its bad predictions without progress. This was inevitable because any improvement would have been antagonistic to the good reproduction of all the other LFSs, as highlighted also by the datasets by Eckart et al. in Figure 4.23.

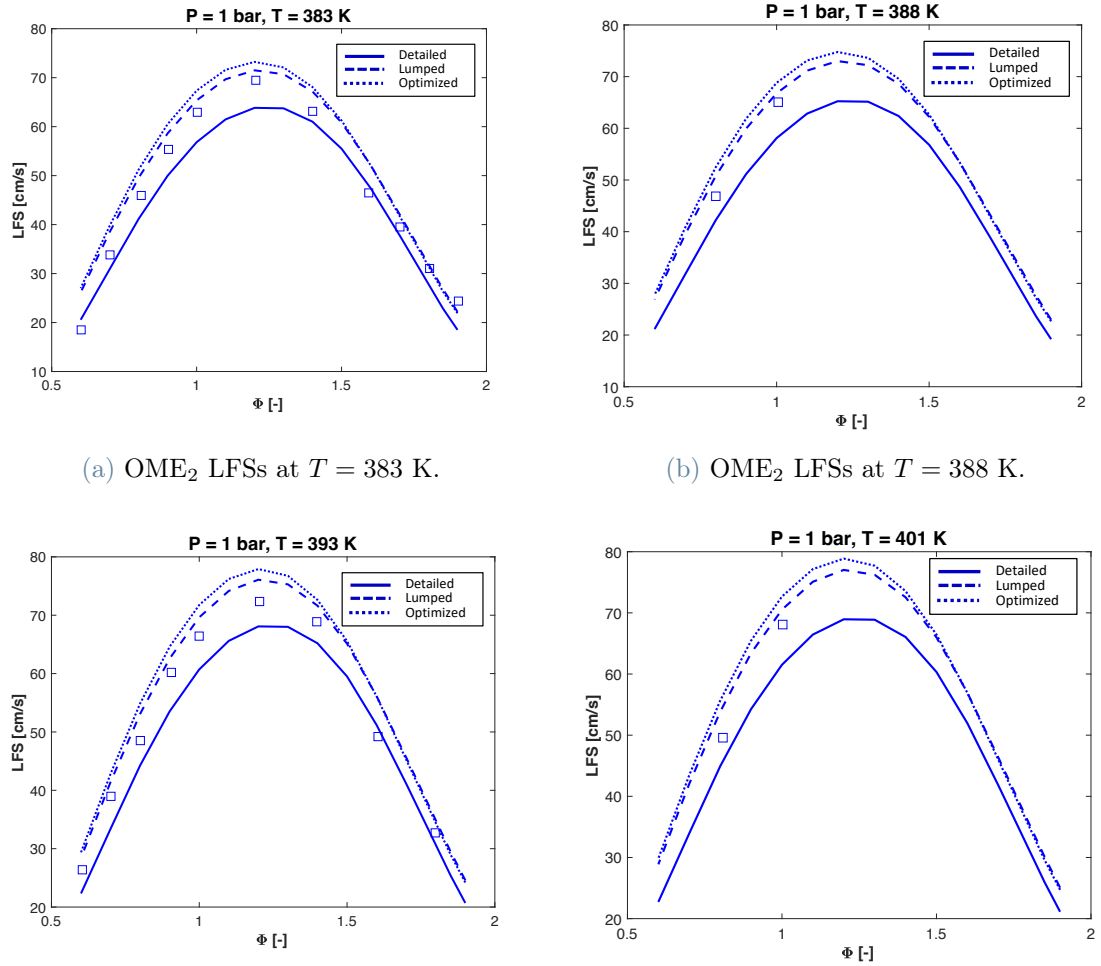

(a) OME_2 LFSs at $T = 383$ K.

(b) OME_2 LFSs at $T = 388$ K.

(c) OME_2 LFSs at $T = 393$ K.

(d) OME_2 LFSs at $T = 401$ K.

Figure 4.23: OME_2 LFSs measured by Eckart et al. [99] and models predictions. OME_2 is diluted in air. Experiments are carried out at $P = 1$ bar and $T = 383$–401 K.

4.3.3. Conclusions

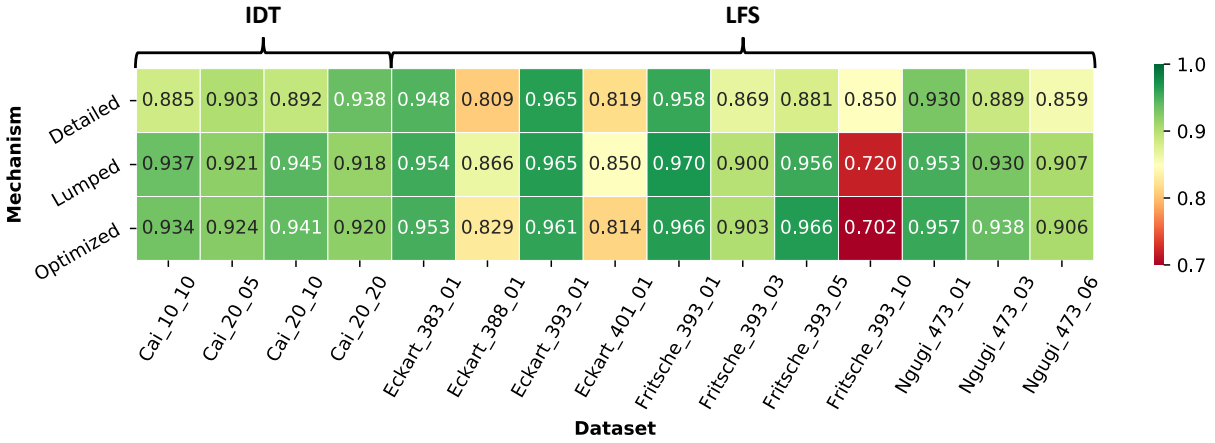

Figure 4.24: Heat map summarizing the CM indices of OME_2.

Figure 4.24 collects in a heat map all the CM indices that assess the OME_2 simulations performances against the experimental data, allowing a visual comparison between the models. Both IDTs and LFSs scores confirm what already said by qualitatively illustrating the plots.

IDTs are generally better reproduced by the lumped model, which hence it is not improved further with optimization. The $\Phi = 2$ and $P = 20$ bar case is the only one affected negatively by the increased lumped reactivity, and then partially recovered with the final mechanism.

LFSs, similarly, are less accurately predicted by the detailed model than by the lumped one. Also its optimization, despite being carried out together with the LFSs targets of OME_3 and OME_4, lead to further minor improvements. The 10 bar dataset by Fritsche et al. stands out for its particularly bad indices both for the lumped and optimized model: this, as already explained, is a direct consequence of its antagonistic nature with respect to all other datasets. Also two of the Eckart et al. datasets present lower scores, but this is only due to their very small number of data points (two each), which do not allow a satisfying estimation of the curve parameters.

4.4. OME_3

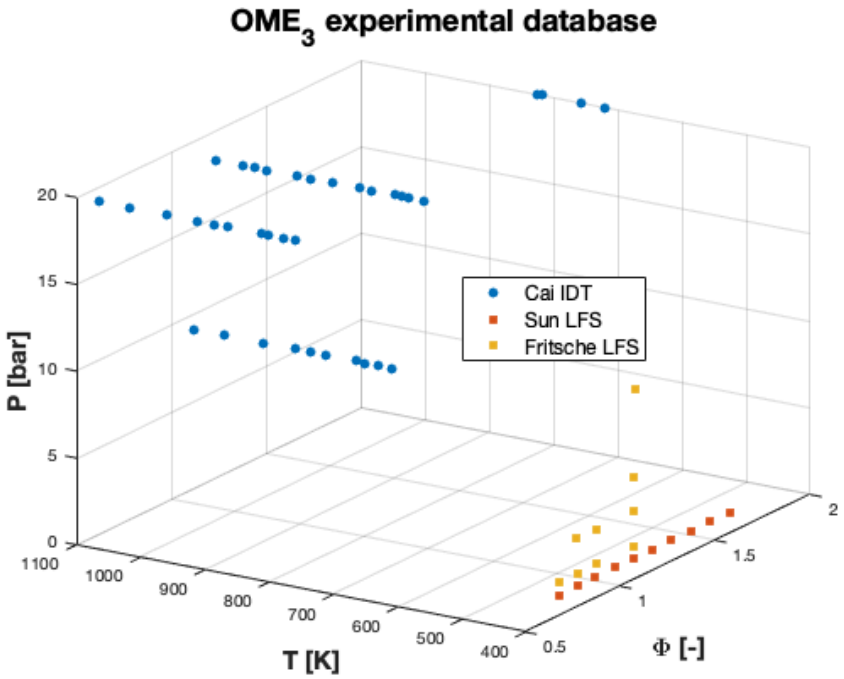

Figure 4.25: OME_3 experimental database.

The experimental database of OME_3 includes IDTs in STs [58] and LFSs [55], while speciations are still missing from the literature. Among its nine datasets, reported in Figure 4.25, six have been chosen as optimization targets, while the remaining three were kept only to validate the models. More details can be found in Chapter 3.

4.4.1. Ignition Delay Times

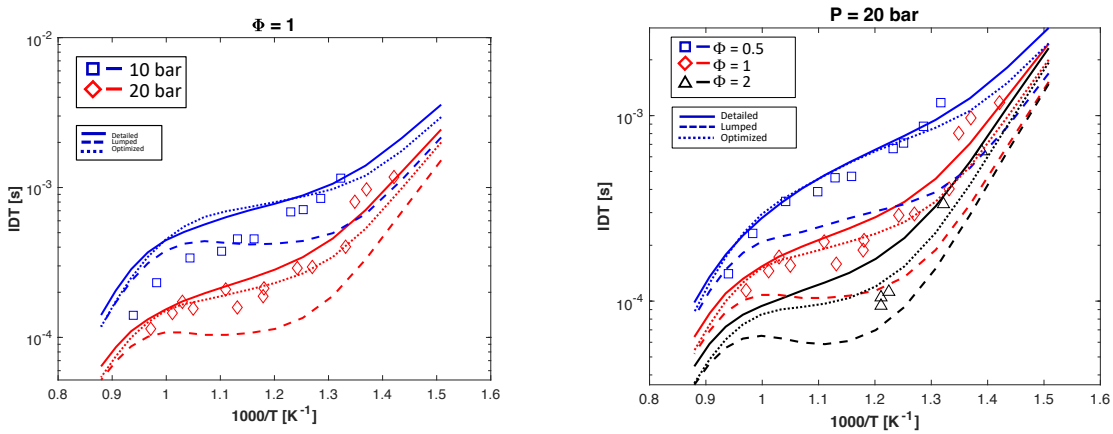

(a) OME_3 IDTs at $\Phi = 1$ and $P = 10$–20 bar. (b) OME_3 IDTs at $\Phi = 0.5$–2 and $P = 20$ bar.

Figure 4.26: OME_3 IDTs measured in a ST by Cai et al. [58] and models predictions. OME_3 is diluted in air.

Cai et al. [58] collected IDTs results in STs also for OME_3, at $T \simeq 700$–1100 K, $\Phi = 0.5$–2 and $P = 20$ bar. Figure 4.26 compares these experimental data with the models predictions.

Contrarily to OME_2, the detailed model reasonably reproduces the experiments in the conditions of interest. For this reason, the acceleration caused by the lumping procedure lead to a worsening of the behaviours. An exception is the simulation at $\Phi = 2$ and $P = 20$ bar, where the increased NTC effect results in a better accordance between model and data. The optimization process had a big impact on the OME_3 IDTs, reducing its low temperature reactivity and bringing the optimized curve near the original detailed one.

4.4.2. Laminar Flame Speeds

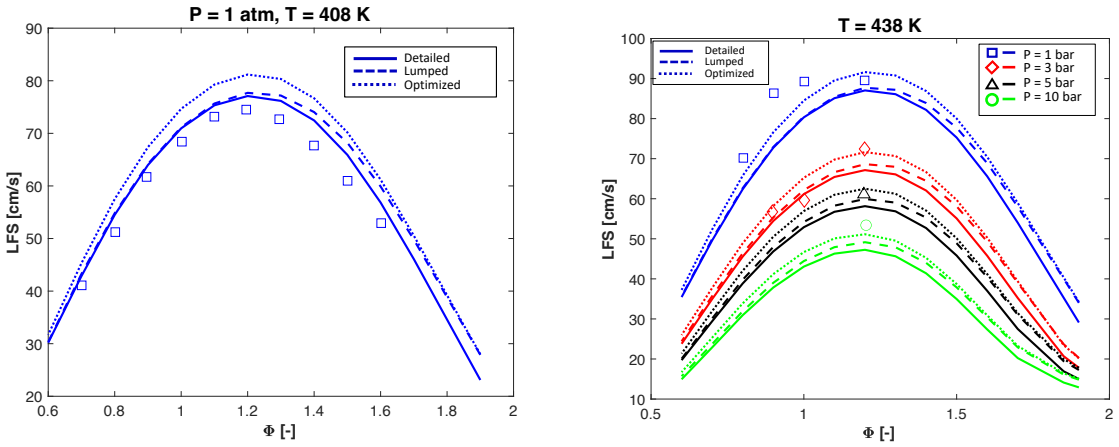

(a) OME_3 LFSs at $T = 408$ K and $P = 1$ atm. (b) OME_3 LFSs at $T = 438$ K and $P = 1$–10 bar.

Figure 4.27: OME_3 LFSs measured by Sun et al. [55] (a) and Fritsche et al. [85] (b), and models predictions. OME_3 is diluted in air.

Figure 4.27 reports the models simulation results compared to the LFSs measurements performed by Sun et al. [55] and Fritsche et al. [85]. Conditions of interest of the studies are $T = 408$–438 K, $\Phi = 0.7$–1.6 and $P = 1$–10 bar.

The detailed mechanism correctly predicts the dataset by Sun et al., only over-estimating results for rich conditions by less than 5 cm/s. Datasets by Fritsche et al., on the other hand, are under-predicted for all pressures, with only the $P = 3$ bar dataset well reproduced. It must be said, though, that the isolated data available for the higher pressures make the evaluation less reliable.

4.4.3. Conclusions

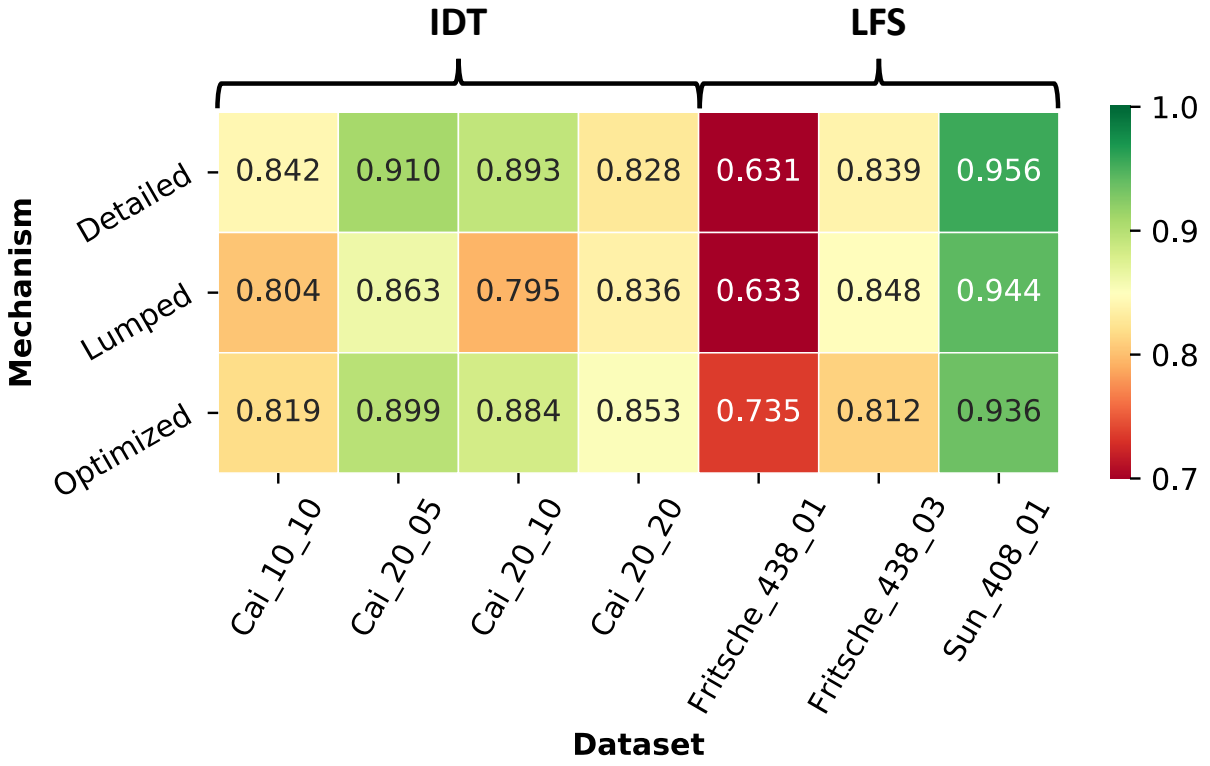

Figure 4.28: Heat map summarizing the CM indices of OME_3.

The CM indices calculated to quantitatively determine the performances of the models for OME_3 are collected in a heat map depicted in Figure 4.28.

It can be seen that IDTs worsened with the acceleration of the kinetics associated with the lumping process, with the only exception being the simulation at $\Phi = 2$ and $P = 20$ bar. Nonetheless, the final optimized model recovered most of the original accuracy.

CM indices of LFSs could not be computed for the high pressures datasets of Fritsche et al., due to the single data points present, and the ones which could be evaluated seem to perform very bad because of the small amounts of data entries. The scores for the experiments by Sun et al., instead, well reflect the good behaviours of the models in reproducing the data. The minor worsening of the optimized model is caused by the necessary trade-off to reconcile data from different authors into a single optimization.

4.5. OME_4

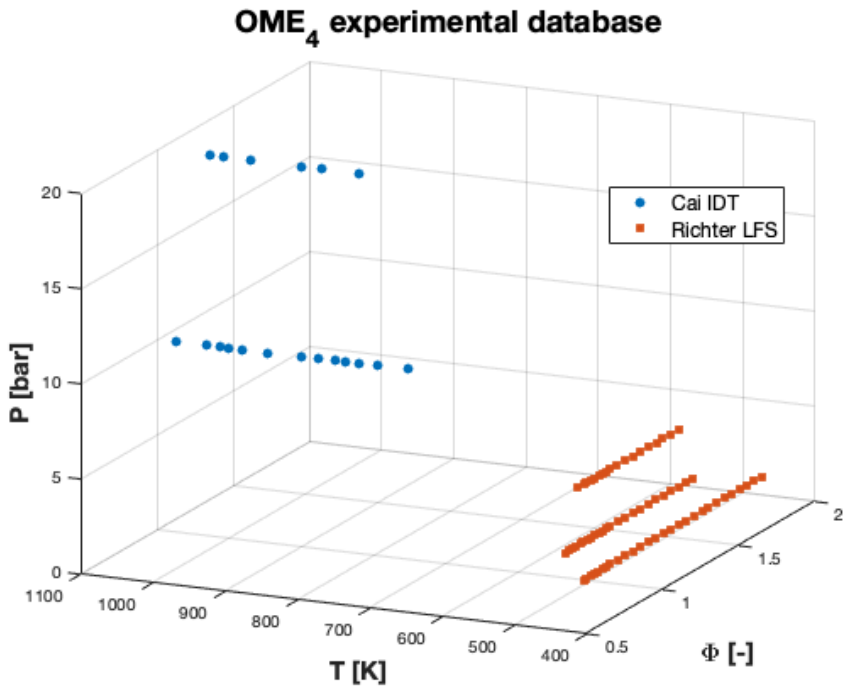

Figure 4.29: OME_4 experimental database.

In Figure 4.29 are schematized the five datasets of the OME_4 experimental database. They consist of IDTs in STs [58] and LFSs [86] since, as for OME_2 and OME_3, speciations are not available yet. Because of the small amount of data at hand, all five datasets were adopted as optimization targets.

4.5.1. Ignition Delay Times

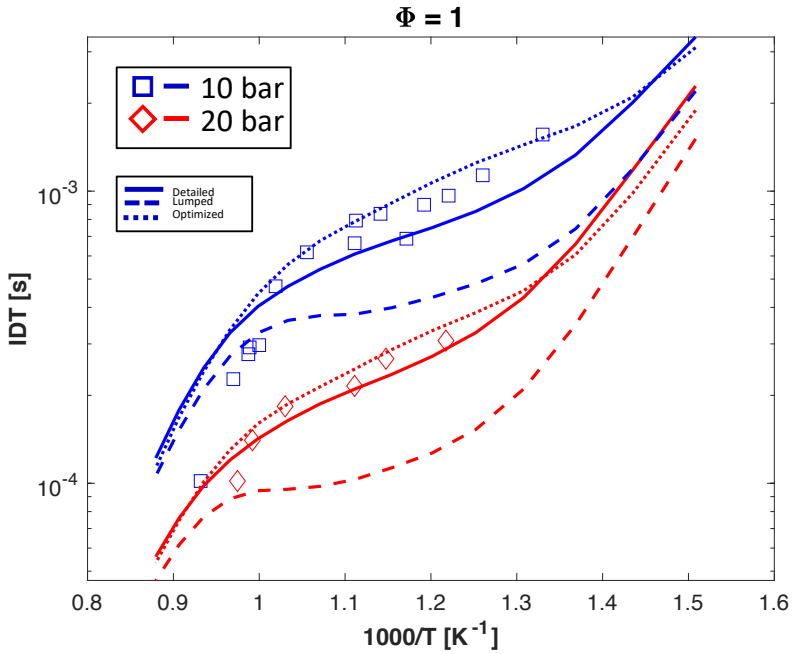

Figure 4.30: OME_4 IDTs measured in a ST by Cai et al. [58] and models predictions. OME_4 is diluted in air.

The only IDTs available for OME_4 are measured in a ST by Cai et al. [58] at $T \simeq 750$–1050 K, $\Phi = 1$ and $P = 10$–20 bar. The detailed mechanism well reproduces the experimental results, consequently, as for OME_3, the lumped model is too fast of about a factor 2, and its NTC behaviour too evident. The optimized kinetics is slightly less reactive than the original detailed one, but the performance is not affected negatively by this difference.

To analyze the reaction rates modified in the optimization step, the most sensitive reactions for OME_4 at $T = 870$ K, $\Phi = 1$ and $P = 10$–20 bar are listed in Figure 4.31. The sensitivity analyses were performed in the same zero-dimensional reactor at three different characteristic times, chosen as described in Chapter 3. For each reaction, it is also reported the ratio between its optimized and nominal lumped rates: all of them are inside the uncertainty limit of about 2, defined by the adopted uncertainty factor $f = 0.3$. $R\dot{O}_2$ and $\dot{O}_2QOOH$ formations via O_2 addition enhance the low temperature reactivity, henceforth their rates are reduced during the optimization. On the other hand, β-decomposition rates are increased, since they limit the number of reactive radicals in the branching path. It can also be noticed that the oxidation of the OME_3 $\dot{Q}OOH$ and alkyl radicals increase the fuel reactivity, confirming that there is a dependence of the

OME_4 chemistry on the kinetics of the smaller ethers. This proves the already mentioned interconnection between the $OME_{2–4}$ sub-mechanisms, which needed to be optimized all together.

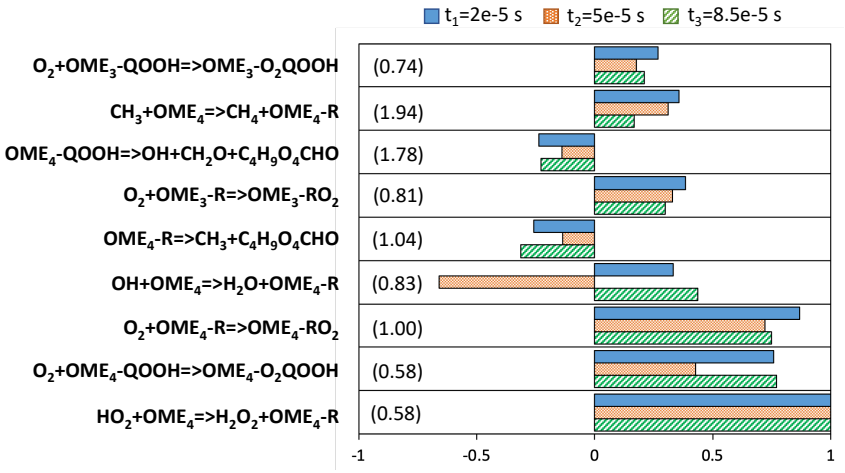

Figure 4.31: Sensitivity analyses to OH mass fraction in IDTs of OME_4. Investigated conditions are $T = 870$ K, $\Phi = 1$ and $P = 10–20$ bar. The three characteristic times have been selected as reported in Chapter 3. Values in brackets represents the ratio between optimized and nominal lumped rates.

4.5.2. Laminar Flame Speeds

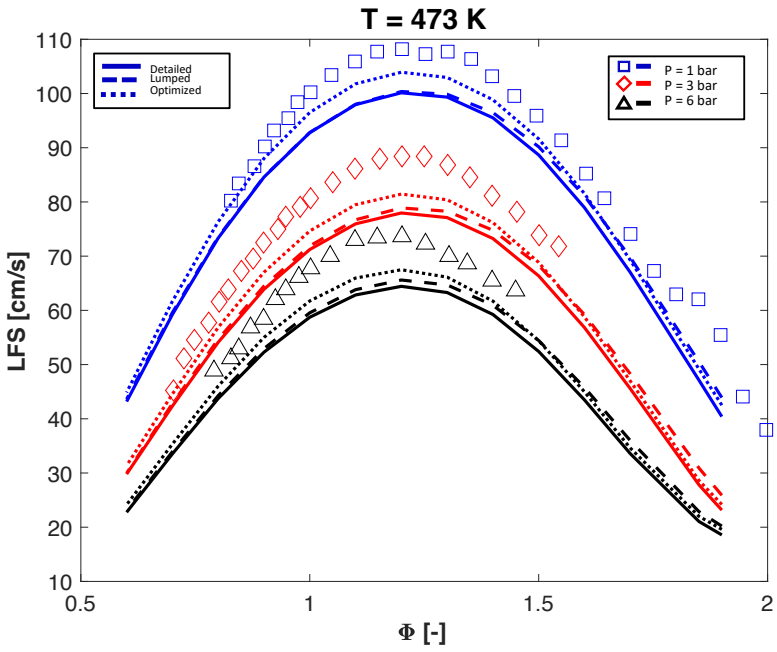

Figure 4.32: OME_4 LFSs measured by Richter et al. [86] and models predictions. OME_4 is diluted in air. Experiments are carried out at $P = 1$–6 bar and $T = 473$ K.

The LFS measurements available for OME_4 have been quantified by Richter et al. [86] and are plotted in Figure 4.32. The operating conditions of interest are $T = 473$ K, $\Phi = 0.7$–2 and $P = 1$–6 bar.

The detailed model, and the almost identical lumped one, under-estimate the flame velocity of about 15 cm/s, especially around the maximum value at $\Phi \simeq 1.2$. Even if the sensitive reactions for LFS are only four, the effect of their optimization can be seen in a reduction of the gap between experiments and predictions of about 5 cm/s.

4.5.3. Conclusions

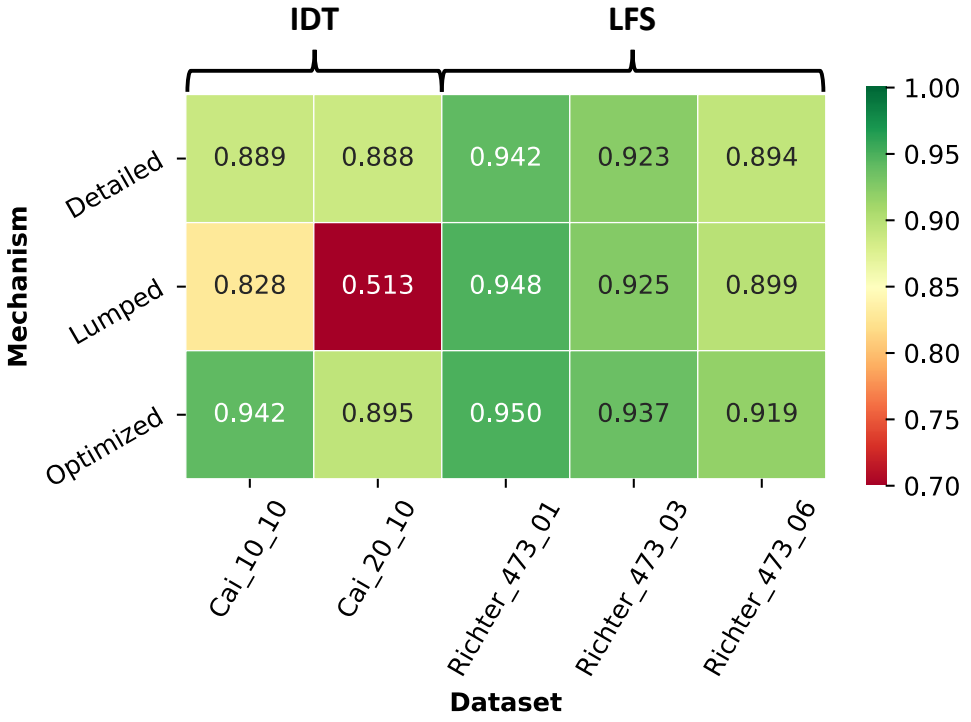

Figure 4.33: Heat map summarizing the CM indices of OME_4.

The CM scores for all five OME_4 datasets are summarized in Figure 4.33. The lumping process marginally improved the LFSs predictions by accelerating the fuel burning velocity, while performances for IDTs were negatively affected by the higher reactivity. Nevertheless, the optimized model performs better than the initial detailed one in every case considered. This suggests that the choice of reactions to optimize and experimental targets was optimal.

The score of the lumped model for IDTs at $\Phi = 1$ and $P = 20$ bar stands out for its particularly low value. This is partly due to the smaller amount of data available in these conditions, which negatively influence the curves comparison. As a matter of fact, by looking at Figure 4.30 it is clear that the qualitative behaviours of the lumped model in the two conditions are similar, hence the worsening of the index can be ascribed to the smaller domain of the experimental data at $P = 20$ bar.

5 | Final remarks

In the combustion field, it is common practice to exploit models in order to simulate experiments, saving time and resources. The importance of detailed kinetics in this context has been progressively acknowledged, and the current available computational power already allows its implementation in heavy simulations for small fuels. Its limits, though, become evident when involving more complex molecules: the number of species whose chemistry must be described rises quickly, and this increases the number of transport equations to solve. The consequence is the impossibility to use detailed models of these heavy molecules in demanding tasks, such as CFD applications, without the computational time to become unsustainable [48]. The research for reduced mechanisms assumes then a key role in the chemical kinetics, where finding a good trade-off between accuracy and size of the model is essential.

OMEs are a class of innovative fuels that is gaining the interest of the scientific community, mainly because of its soot- and NO_x-reducing properties as diesel additive [8, 11, 12]. As a matter of fact, its characteristics makes it suitable to be blended with diesel without substantially altering its combustion, and allowing it to be adopted even in current engines, with minor modifications at most [21]. The mechanisms describing OMEs currently available in literature are detailed, and suffer of the limitations discussed above: a reduced model is needed to accelerate CFD studies regarding combustion in engines.

5.1. Results

In this Thesis, a new methodology has been developed, successfully coupling the lumping of structural isomers with a data-driven optimization procedure, in order to obtain a reliable reduced kinetic model for $OME_{0–4}$. To build the detailed kinetics, the hierarchical approach was exploited, meaning that each new sub-mechanism was added to the others in a modular way. The core mechanism is the detailed chemistry of C_1-C_3 [62, 65, 66], already largely consolidated, on top of which the DME [67, 68], DMM [51] and $OME_{2–4}$ [58] sub-mechanisms from the literature were included.

The detailed model was lumped adopting a recent procedure (MEL) [72] based on the Master Equation. MEL was adapted to work on a macroscopic mechanism and properly reduce it, and it was then applied on each $OME_{1–4}$ sub-mechanism separately, in line with the hierarchy principle. The species were grouped into pseudospecies according to structural isomerism, greatly reducing their final number from 282 to 176.

As a final step, an optimization procedure that exploits evolutionary algorithms was performed [73] on the lumped mechanism. The optimization targets were selected from a large database of experimental results, covering a wide range of operating conditions and reactors. Through sensitivity analysis, a total of 57 reactions to optimize was identified, and three blocks of optimizations were defined, as described in Chapter 3.

Table 5.1 quantitatively summarizes the outcomes of the validations of the three mechanisms against the experimental data. Results are reported for each fuel in terms of CM scores [77], considering the whole experimental database adopted. These indices allow an objective evaluation of the agreement between models and experiments, where 1 stands for perfect accordance, and 0 for maximum disagreement. The scores of the lumped model reveal a general worsening of performances, especially for OME_4 and with the only exception of OME_2. Despite this, the final optimized mechanism provides a higher score for all fuels, even compared to the starting model, confirming that the data-driven optimization was successful.

Fuel	**Average Curve Matching index**		
	Detailed	**Lumped**	**Optimized**
DMM	0.906	0.894	0.911
OME_2	0.893	0.913	0.908
OME_3	0.843	0.818	0.848
OME_4	0.907	0.823	0.929
$OME_{1–4}$	0.892	0.881	0.902

Table 5.1: Average Curve Matching indices of the adopted mechanisms for each OME.

5.2. Future work

The results obtained from the application of the developed workflow are very satisfying: a detailed mechanism for $OME_{0–4}$ has been successfully lumped and subsequently optimized

to match experimental data in different conditions. Despite this, there is of course still room for improvement so, to conclude, the major points of possible future works will be here discussed.

5.2.1. Lumping

The lumping procedure can be performed more consistently with a separate evaluation of the pseudospecies BFs for each mechanism block. In this Thesis, for each OME a 0-dimensional simulation was carried out with the detailed model (more information can be found in Chapter 2.3), from which the BFs of the pseudospecies were calculated. If the simulations were instead performed using a single mechanism block at a time, with each pseudospecies in turn as reactant, the BFs could be tailored for every block to be lumped, and the results could improve. An example of this approach can be found in a work where MEL has been adopted to lump the low-temperature kinetics of n-pentane [100].

Another improvement to the lumping work would be the adjustment of the thermodynamic database. Pseudospecies, as already mentioned, are here assumed to maintain the properties of the most abundant isomer in their pool. This is clearly an approximation, since their properties should be averaged from those of their isomers, weighted on the respective BFs. Nevertheless this implementation is not expected to increase the mechanism precision, since all the equilibrium reactions involving the lumped species have been split into forward and backward ones. Heat transportation only would take benefit, but the very similar specific heats of the isomers in a pseudospecies would make the difference irrelevant.

5.2.2. Optimization

The biggest upgrade of the optimization procedure would be the implementation of an approach based on reaction classes. All reactions have been optimized independently in the present Thesis, meaning that the parameters of different reactions belonging to the same class could have been modified in an opposite way, reducing their physical consistency. A more solid method would treat these reactions together, similarly to how different pressures of a PLOG reaction are handled. This would guarantee that all the reactions of a class are optimized coherently, retaining the physical meaning of the various parameters.

The experimental uncertainties available in literature could be easily included in `OptiSMOKE++` [74] to make the data-driven optimization more consistent. Uncertainties

are accounted for in the bootstrap variations, and ensure that the parameters are not forced to change in order to better predict results that are not certain. The predictions of the model are not expected to improve noticeably with this inclusion, but the overall reliability of the workflow would undoubtedly benefit it.

5.2.3. Automation

The biggest advancement for the method presented in this Thesis would be an automatic workflow, that would allow to apply it rapidly to multiple mechanisms, without much work of the user. The modular approach makes automation not only very interesting, but also feasible. The steps of a possible algorithm are briefly reported here:

1. the pseudospecies are defined by the user, for example by structural isomerism, and the species pools are automatically identified;
2. the mechanism is automatically divided into blocks with the same global stoichiometry, for each one the BFs are calculated and the equilibrium reactions are split into forward and backward ones;
3. with the evaluated BFs each block is lumped separately, and the thermodynamic and transport properties of the pseudospecies are averaged from the ones of their isomers;
4. the user provides experimental datasets to adopt either as optimization targets and for validation;
5. suitable sensitivity analyses are performed on the lumped mechanism for the various datasets, and the reactions to be optimized are automatically selected;
6. the optimizations are carried out and the optimized mechanism is produced;
7. the optimized model is validated against all the datasets provided, and CM scores are calculated to assess the performances.

If a completely automated workflow were to be developed, the amount of time saved would be considerable and the applications numerous. For example, the same mechanism could be lumped and optimized in several different ways in parallel, and the best ranking resulting model picked out. Also heavier fuels models, where the computational advantages are expected to be even greater, could be lumped much more quickly. It is undeniable that an automatic consolidated methodology would accelerate the combustion research, by making the development of reduced kinetics faster.

Bibliography

[1] International Energy Agency. *World Energy Outlook 2021*. IEA, 2021.

[2] Pete Smith, Linda Beaumont, Carl J. Bernacchi, Maria Byrne, William Cheung, Richard T. Conant, Francesca Cotrufo, Xiaojuan Feng, Ivan Janssens, Hefin Jones, Miko U. F. Kirschbaum, Kazuhiko Kobayashi, Julie LaRoche, Yiqi Luo, Andrew McKechnie, Josep Penuelas, Shilong Piao, Sharon Robinson, Rowan F. Sage, David J. Sugget, Stephen J. Thackeray, Danielle Way, and Stephen P. Long. Essential outcomes for cop26. *Global Change Biology*, October 2021.

[3] Yee Van Fan, Simon Perry, Jiří Jaromír Klemeš, and Chew Tin Lee. A review on air emissions assessment: Transportation. *Journal of cleaner production*, 194:673–684, 2018.

[4] H Christopher Frey. Trends in onroad transportation energy and emissions. *Journal of the Air & Waste Management Association*, 68(6):514–563, 2018.

[5] European Commission. eurosat. `http://ec.europa.eu/eurostat/home`, 2021.

[6] Linda Ager-Wick Ellingsen, Guillaume Majeau-Bettez, Bhawna Singh, Akhilesh Kumar Srivastava, Lars Ole Valøen, and Anders Hammer Strømman. Life cycle assessment of a lithium-ion battery vehicle pack. *Journal of Industrial Ecology*, 18(1):113–124, 2014.

[7] International Energy Agency. Electricity information: Overview. `https://www.iea.org/reports/electricity-information-overview`, 2021.

[8] Ahmad Omari, Benedikt Heuser, Stefan Pischinger, and Christoph Rüdinger. Potential of long-chain oxymethylene ether and oxymethylene ether-diesel blends for ultra-low emission engines. *Applied energy*, 239:1242–1249, 2019.

[9] Bruna Alves. Global outlook on electricity generation by energy source 2018-2050. `https://www.statista.com/statistics/238610/projected-world-electricity-generation-by-energy-source/`, 2018.

[10] Patrick Dworschak, Vinicius Berger, Martin Härtl, and Georg Wachtmeister. Neat

oxymethylene ethers: Combustion performance and emissions of ome 2, ome 3, ome 4 and ome 5 in a single-cylinder diesel engine. Technical report, SAE Technical Paper, 2020.

[11] Jialin Liu, Hu Wang, Ying Li, Zunqing Zheng, Zhenzhen Xue, Hongyan Shang, and Mingfa Yao. Effects of diesel/pode (polyoxymethylene dimethyl ethers) blends on combustion and emission characteristics in a heavy duty diesel engine. *Fuel*, 177:206–216, 2016.

[12] Yong Ren Tan, Maurin Salamanca, Laura Pascazio, Jethro Akroyd, and Markus Kraft. The effect of poly (oxymethylene) dimethyl ethers (pode3) on soot formation in ethylene/pode3 laminar coflow diffusion flames. *Fuel*, 283:118769, 2021.

[13] Federica Ferraro, Carmela Russo, Robert Schmitz, Christian Hasse, and Mariano Sirignano. Experimental and numerical study on the effect of oxymethylene ether-3 (ome3) on soot particle formation. *Fuel*, 286:119353, 2021.

[14] Dominik Goeb, Marco Davidovic, Liming Cai, Pankaj Pancharia, Mathis Bode, Sascha Jacobs, Joachim Beeckmann, Werner Willems, Karl Alexander Heufer, and Heinz Pitsch. Oxymethylene ether–n-dodecane blend spray combustion: Experimental study and large-eddy simulations. *Proceedings of the Combustion Institute*, 38(2):3417–3425, 2021.

[15] Robert Schmitz, Mariano Sirignano, Christian Hasse, and Federica Ferraro. Numerical investigation on the effect of the oxymethylene ether-3 (ome3) blending ratio in premixed sooting ethylene flames. *Frontiers in Mechanical Engineering*, page 81, 2021.

[16] Daniel Himmel, Robin J. White, Eberhard Jacob, and Ingo Krossing. Highly correlated ab initio thermodynamics of oxymethylene dimethyl ethers (ome): formation and extension to the liquid phase. *Sustainable Energy Fuels*, 1:1177–1183, 2017.

[17] X Bao and Y Xu. Large-scale gas conversion through oxygenates: beyond. In *Natural Gas Conversion VII: Proceedings of the 7th Natural Gas Conversion Symposium, Dalian, China, 6-10 June 2004*, page 31. Elsevier, 2004.

[18] Wang Ying, Li Genbao, Zhu Wei, and Zhou Longbao. Study on the application of dme/diesel blends in a diesel engine. *Fuel processing technology*, 89(12):1272–1280, 2008.

[19] Xiaoming Zhao, Meifeng Ren, and Zhigang Liu. Critical solubility of dimethyl ether

(dme)+ diesel fuel and dimethyl carbonate (dmc)+ diesel fuel. *fuel*, 84(18):2380–2383, 2005.

[20] Keith D Vertin, James M Ohi, David W Naegeli, Kenneth H Childress, Gary P Hagen, Chris I McCarthy, Adelbert S Cheng, and Robert W Dibble. Methylal and methylal-diesel blended fuels for use in compression-ignition engines. Technical report, SAE Technical Paper, 1999.

[21] M Marchionna, R Patrini, D Sanfilippo, A Paggini, F Giavazzi, and L Pellegrini. From natural gas to oxygenates for cleaner diesel fuels. In *Studies in Surface Science and Catalysis*, volume 136, pages 489–494. Elsevier, 2001.

[22] Jakob Burger, Markus Siegert, Eckhard Ströfer, and Hans Hasse. Poly (oxymethylene) dimethyl ethers as components of tailored diesel fuel: Properties, synthesis and purification concepts. *Fuel*, 89(11):3315–3319, 2010.

[23] Dominik Pélerin, Kai Gaukel, Martin Härtl, and Georg Wachtmeister. Nitrogen oxide reduction potentials using dimethyl ether and oxymethylene ether in a heavy-duty diesel engine. Technical report, SAE Technical Paper, 2020.

[24] Gilles Prado, Jacques Lahaye, and Brian S Haynes. Soot particle nucleation and agglomeration. In *Soot in combustion systems and its toxic properties*, pages 145–161. Springer, 1983.

[25] Hussein I Abdel-Shafy and Mona SM Mansour. A review on polycyclic aromatic hydrocarbons: source, environmental impact, effect on human health and remediation. *Egyptian journal of petroleum*, 25(1):107–123, 2016.

[26] Kenth I Svensson, Michael J Richards, Andrew J Mackrory, and Dale R Tree. Fuel composition and molecular structure effects on soot formation in direct-injection flames under diesel engine conditions. *SAE transactions*, pages 594–604, 2005.

[27] Martin Härtl, Philipp Seidenspinner, Eberhard Jacob, and Georg Wachtmeister. Oxygenate screening on a heavy-duty diesel engine and emission characteristics of highly oxygenated oxymethylene ether fuel ome1. *Fuel*, 153:328–335, 2015.

[28] Hideyuki Ogawa, Md Nurun Nabi, Masahiro Minami, Noboru Miyamoto, and Kim Bong-Seock. Ultra low emissions and high performance diesel combustion with a combination of high egr, three-way catalyst, and a highly oxygenated fuel, dimethoxy methane (dmm). *SAE transactions*, pages 1019–1027, 2000.

[29] Jakob Burger, Eckhard Ströfer, and Hans Hasse. Chemical equilibrium and reaction kinetics of the heterogeneously catalyzed formation of poly (oxymethylene) dimethyl

ethers from methylal and trioxane. *Industrial & engineering chemistry research*, 51(39):12751–12761, 2012.

[30] Jakob Burger and Hans Hasse. Multi-objective optimization using reduced models in conceptual design of a fuel additive production process. *Chemical Engineering Science*, 99:118–126, 2013.

[31] Jakob Burger, Eckhard Ströfer, and Hans Hasse. Production process for diesel fuel components poly (oxymethylene) dimethyl ethers from methane-based products by hierarchical optimization with varying model depth. *Chemical Engineering Research and Design*, 91(12):2648–2662, 2013.

[32] Niklas Schmitz, Jakob Burger, Eckhard Ströfer, and Hans Hasse. From methanol to the oxygenated diesel fuel poly(oxymethylene) dimethyl ether: An assessment of the production costs. *Fuel*, 185:67–72, 2016.

[33] Diana Deutsch, Dorian Oestreich, Ludger Lautenschütz, Philipp Haltenort, Ulrich Arnold, and Jörg Sauer. High purity oligomeric oxymethylene ethers as diesel fuels. *Chemie Ingenieur Technik*, 89(4):486–489, 2017.

[34] Barbara Elvers et al. *Ullmann's encyclopedia of industrial chemistry*. Verlag Chemie, 1991.

[35] Pontus Bokinge, Stefan Heyne, and Simon Harvey. Renewable ome from biomass and electricity—evaluating carbon footprint and energy performance. *Energy Science & Engineering*, 8(7):2587–2598, 2020.

[36] George A Olah, Alain Goeppert, and GK Surya Prakash. Chemical recycling of carbon dioxide to methanol and dimethyl ether: from greenhouse gas to renewable, environmentally carbon neutral fuels and synthetic hydrocarbons. *The Journal of organic chemistry*, 74(2):487–498, 2009.

[37] PS Sai Prasad, Jong Wook Bae, Suk-Hwan Kang, Yun-Jo Lee, and Ki-Won Jun. Single-step synthesis of dme from syngas on cu–zno–al2o3/zeolite bifunctional catalysts: The superiority of ferrierite over the other zeolites. *Fuel Processing Technology*, 89(12):1281–1286, 2008.

[38] Johannes Liebl and Christian Beidl. *Internationaler Motorenkongress 2016: Mit Konferenz Nfz-Motorentechnologie*. Springer, 2016.

[39] Xiaolei Zhang, Amit Kumar, Ulrich Arnold, and Jörg Sauer. Biomass-derived oxymethylene ethers as diesel additives: A thermodynamic analysis. *Energy Procedia*, 61:1921–1924, 2014.

[40] Xiaolei Zhang, Adetoyese Olajire Oyedun, Amit Kumar, Dorian Oestreich, Ulrich Arnold, and Jörg Sauer. An optimized process design for oxymethylene ether production from woody-biomass-derived syngas. *Biomass and Bioenergy*, 90:7–14, 2016.

[41] Katharina Thenert, Kassem Beydoun, Jan Wiesenthal, Walter Leitner, and Jürgen Klankermayer. Ruthenium-catalyzed synthesis of dialkoxymethane ethers utilizing carbon dioxide and molecular hydrogen. *Angewandte Chemie*, 128(40):12454–12457, 2016.

[42] Qijun Zhang, Haoyan Zhao, Bin Lu, Jingxiang Zhao, and Qinghai Cai. A novel strategy for conversion of methanol and co2 into dimethoxymethane in a basic ionic liquid. *Journal of Molecular Catalysis A: Chemical*, 421:117–121, 2016.

[43] Benjamin G Schieweck and Jürgen Klankermayer. Tailor-made molecular cobalt catalyst system for the selective transformation of carbon dioxide to dialkoxymethane ethers. *Angewandte Chemie International Edition*, 56(36):10854–10857, 2017.

[44] Sarah Deutz, Dominik Bongartz, Benedikt Heuser, Arne Kätelhön, Luisa Schulze Langenhorst, Ahmad Omari, Marius Walters, Jürgen Klankermayer, Walter Leitner, Alexander Mitsos, et al. Cleaner production of cleaner fuels: wind-to-wheel–environmental assessment of co 2-based oxymethylene ether as a drop-in fuel. *Energy & Environmental Science*, 11(2):331–343, 2018.

[45] Charles K Westbrook, Yasuhiro Mizobuchi, Thierry J Poinsot, Phillip J Smith, and Jürgen Warnatz. Computational combustion. *Proceedings of the Combustion Institute*, 30(1):125–157, 2005.

[46] ELISEO Ranzi, Alessio Frassoldati, Roberto Grana, Alberto Cuoci, Tiziano Faravelli, AP Kelley, and Chung King Law. Hierarchical and comparative kinetic modeling of laminar flame speeds of hydrocarbon and oxygenated fuels. *Progress in Energy and Combustion Science*, 38(4):468–501, 2012.

[47] Gene H Golub and Charles F Van Loan. *Matrix computations*. JHU press, 2013.

[48] Alberto Cuoci, Alessio Frassoldati, Tiziano Faravelli, and Eliseo Ranzi. Opensmoke++: An object-oriented framework for the numerical modeling of reactive systems with detailed kinetic mechanisms. *Computer Physics Communications*, 192:237–264, 2015.

[49] Tanjin He, Hao-ye Liu, Yingdi Wang, Boyuan Wang, Hui Liu, and Zhi Wang. Development of surrogate model for oxygenated wide-distillation fuel with poly-

oxymethylene dimethyl ether. *SAE International Journal of Fuels and Lubricants*, 10(3):803–814, 2017.

[50] Florence H Vermeire, Hans-Heinrich Carstensen, Olivier Herbinet, Frédérique Battin-Leclerc, Guy B Marin, and Kevin M Van Geem. Experimental and modeling study of the pyrolysis and combustion of dimethoxymethane. *Combustion and Flame*, 190:270–283, 2018.

[51] Sascha Jacobs, Malte Döntgen, Awad BS Alquaity, Wassja A Kopp, Leif C Kröger, Ultan Burke, Heinz Pitsch, Kai Leonhard, Henry J Curran, and K Alexander Heufer. Detailed kinetic modeling of dimethoxymethane. part ii: Experimental and theoretical study of the kinetics and reaction mechanism. *Combustion and Flame*, 205:522–533, 2019.

[52] Wenyu Sun, Tao Tao, Maxence Lailliau, Nils Hansen, Bin Yang, and Philippe Dagaut. Exploration of the oxidation chemistry of dimethoxymethane: Jet-stirred reactor experiments and kinetic modeling. *Combustion and Flame*, 193:491–501, 2018.

[53] Krishna P Shrestha, Sven Eckart, Ayman M Elbaz, Binod R Giri, Chris Fritsche, Lars Seidel, William L Roberts, Hartmut Krause, and Fabian Mauss. A comprehensive kinetic model for dimethyl ether and dimethoxymethane oxidation and nox interaction utilizing experimental laminar flame speed measurements at elevated pressure and temperature. *Combustion and Flame*, 218:57–74, 2020.

[54] Ning Li, Wuchuan Sun, Shenghua Liu, Xiaokang Qin, Yuwei Zhao, Yanju Wei, and Yingjia Zhang. A comprehensive experimental and kinetic modeling study of dimethoxymethane combustion. *Combustion and Flame*, 233:111583, 2021.

[55] Wenyu Sun, Guoqing Wang, Shuang Li, Ruzheng Zhang, Bin Yang, Jiuzhong Yang, Yuyang Li, Charles K Westbrook, and Chung K Law. Speciation and the laminar burning velocities of poly (oxymethylene) dimethyl ether 3 (pomdme3) flames: An experimental and modeling study. *Proceedings of the Combustion Institute*, 36(1):1269–1278, 2017.

[56] Tanjin He, Zhi Wang, Xiaoqing You, Haoye Liu, Yingdi Wang, Xiaoyu Li, and Xin He. A chemical kinetic mechanism for the low-and intermediate-temperature combustion of polyoxymethylene dimethyl ether 3 (pode3). *Fuel*, 212:223–235, 2018.

[57] Jiaru Bai, Rory Geeson, Feroz Farazi, Sebastian Mosbach, Jethro Akroyd, Eric J Bringley, and Markus Kraft. Automated calibration of a poly (oxymethylene)

dimethyl ether oxidation mechanism using the knowledge graph technology. *Journal of chemical information and modeling*, 61(4):1701–1717, 2021.

[58] Liming Cai, Sascha Jacobs, Raymond Langer, Florian vom Lehn, Karl Alexander Heufer, and Heinz Pitsch. Auto-ignition of oxymethylene ethers (omen, n= 2–4) as promising synthetic e-fuels from renewable electricity: shock tube experiments and automatic mechanism generation. *Fuel*, 264:116711, 2020.

[59] Liming Cai and Heinz Pitsch. Mechanism optimization based on reaction rate rules. *Combustion and flame*, 161(2):405–415, 2014.

[60] Tianfeng Lu and Chung K Law. Toward accommodating realistic fuel chemistry in large-scale computations. *Progress in Energy and Combustion Science*, 35(2):192–215, 2009.

[61] Eliseo Ranzi, Alessio Frassoldati, Silvia Granata, and Tiziano Faravelli. Wide-range kinetic modeling study of the pyrolysis, partial oxidation, and combustion of heavy n-alkanes. *Industrial & engineering chemistry research*, 44(14):5170–5183, 2005.

[62] Ghobad Bagheri, Eliseo Ranzi, Matteo Pelucchi, Alessandro Parente, Alessio Frassoldati, and Tiziano Faravelli. Comprehensive kinetic study of combustion technologies for low environmental impact: Mild and oxy-fuel combustion of methane. *Combustion and Flame*, 212:142–155, 2020.

[63] Eliseo Ranzi, Carlo Cavallotti, Alberto Cuoci, Alessio Frassoldati, Matteo Pelucchi, and Tiziano Faravelli. New reaction classes in the kinetic modeling of low temperature oxidation of n-alkanes. *Combustion and Flame*, 162(5):1679–1691, 2015.

[64] Eliseo Ranzi, Alessio Frassoldati, Alessandro Stagni, Matteo Pelucchi, Alberto Cuoci, and Tiziano Faravelli. Reduced kinetic schemes of complex reaction systems: fossil and biomass-derived transportation fuels. *International Journal of Chemical Kinetics*, 46(9):512–542, 2014.

[65] Wayne K Metcalfe, Sinéad M Burke, Syed S Ahmed, and Henry J Curran. A hierarchical and comparative kinetic modeling study of c1- c2 hydrocarbon and oxygenated fuels. *International Journal of Chemical Kinetics*, 45(10):638–675, 2013.

[66] Sinéad M Burke, Ultan Burke, Reuben Mc Donagh, Olivier Mathieu, Irmis Osorio, Charles Keesee, Anibal Morones, Eric L Petersen, Weijing Wang, Trent A DeVerter, et al. An experimental and modeling study of propene oxidation. part 2: Ignition delay time and flame speed measurements. *Combustion and Flame*, 162(2):296–314, 2015.

[67] Ultan Burke, Kieran P Somers, Peter O'Toole, Chis M Zinner, Nicolas Marquet, Gilles Bourque, Eric L Petersen, Wayne K Metcalfe, Zeynep Serinyel, and Henry J Curran. An ignition delay and kinetic modeling study of methane, dimethyl ether, and their mixtures at high pressures. *Combustion and Flame*, 162(2):315–330, 2015.

[68] Alessandro Stagni, Steffen Schmitt, Matteo Pelucchi, Alessio Frassoldati, Katharina Kohse-Höinghaus, and Tiziano Faravelli. Dimethyl ether oxidation analyzed in a given flow reactor: Experimental and modeling uncertainties. *Combustion and Flame*, 240:111998, 2022.

[69] C Cavallotti, M Pelucchi, Y Georgievskii, and SJ Klippenstein. Estoktp: Electronic structure to temperature-and pressure-dependent rate constants—a code for automatically predicting the thermal kinetics of reactions. *Journal of chemical theory and computation*, 15(2):1122–1145, 2018.

[70] Reaction Design. Chemkin theory manual. *San Diego, CA*, 2007.

[71] CJ Cobos, H Hippler, and J Troe. High-pressure falloff curves and specific rate constants for the reactions atomic hydrogen+ molecular oxygen. dblharw. perhydroxyl. dblharw. hydroxyl+ atomic oxygen. *The Journal of Physical Chemistry*, 89(2):342–349, 1985.

[72] Luna Pratali Maffei, Matteo Pelucchi, Carlo Cavallotti, Andrea Bertolino, and Tiziano Faravelli. Master equation lumping for multi-well potential energy surfaces: a bridge between ab initio based rate constant calculations and large kinetic mechanisms. *Chemical Engineering Journal*, 422:129954, 2021.

[73] Andrea Bertolino, Magnus Fürst, Alessandro Stagni, Alessio Frassoldati, Matteo Pelucchi, C Cavallotti, T Faravelli, and Alessandro Parente. An evolutionary, data-driven approach for mechanism optimization: theory and application to ammonia combustion. *Combustion and Flame*, 229:111366, 2021.

[74] Magnus Fürst, Andrea Bertolino, Alberto Cuoci, Tiziano Faravelli, Alessio Frassoldati, and Alessandro Parente. Optismoke++: A toolbox for optimization of chemical kinetic mechanisms. *Computer Physics Communications*, 264:107940, 2021.

[75] Brian Adams, William Bohnhoff, Keith Dalbey, Mohamed Ebeida, John Eddy, Michael Eldred, Russell Hooper, Patricia Hough, Kenneth Hu, John Jakeman, et al. Dakota, a multilevel parallel object-oriented framework for design optimization, parameter estimation, uncertainty quantification, and sensitivity analysis: Version 6.13 user's manual. Technical report, Sandia National Lab.(SNL-NM), Albuquerque, NM (United States), 2020.

[76] Carsten Olm, István Gy Zsély, Tamás Varga, Henry J Curran, and Tamás Turányi. Comparison of the performance of several recent syngas combustion mechanisms. *Combustion and Flame*, 162(5):1793–1812, 2015.

[77] Matteo Pelucchi, Alessandro Stagni, and Tiziano Faravelli. Addressing the complexity of combustion kinetics: Data management and automatic model validation. In *Computer Aided Chemical Engineering*, volume 45, pages 763–798. Elsevier, 2019.

[78] Mara Sabina Bernardi, Matteo Pelucchi, Alessandro Stagni, Laura Maria Sangalli, Alberto Cuoci, Alessio Frassoldati, Piercesare Secchi, and Tiziano Faravelli. Curve matching, a generalized framework for models/experiments comparison: An application to n-heptane combustion kinetic mechanisms. *Combustion and Flame*, 168:186–203, 2016.

[79] James O Ramsay and CJ Dalzell. Some tools for functional data analysis. *Journal of the Royal Statistical Society: Series B (Methodological)*, 53(3):539–561, 1991.

[80] Magnus Fürst, Pino Sabia, Marco Lubrano Lavadera, Gianmarco Aversano, Mara De Joannon, Alessio Frassoldati, and Alessandro Parente. Optimization of chemical kinetics for methane and biomass pyrolysis products in moderate or intense low-oxygen dilution combustion. *Energy & fuels*, 32(10):10194–10201, 2018.

[81] RG Gilbert, K_ Luther, and J Troe. Theory of thermal unimolecular reactions in the fall-off range. ii. weak collision rate constants. *Berichte der Bunsengesellschaft für physikalische Chemie*, 87(2):169–177, 1983.

[82] Fiona Rita Gillespie. *An experimental and modelling study of the combustion of oxygenated hydrocarbons*. PhD thesis, National University of Ireland–Galway, 2014.

[83] Alessandro Stagni, Yu Song, Laurien A Vandewalle, Kevin M Van Geem, Guy B Marin, Olivier Herbinet, Frederique Battin-Leclerc, and Tiziano Faravelli. The role of chemistry in the oscillating combustion of hydrocarbons: An experimental and theoretical study. *Chemical Engineering Journal*, 385:123401, 2020.

[84] John M Ngugi, Sandra Richter, Marina Braun-Unkhoff, Clemens Naumann, Markus Köhler, and Uwe Riedel. A study on fundamental combustion properties of oxymethylene ether-2. *Journal of Engineering for Gas Turbines and Power*, 144(1), 2022.

[85] Chris Fritsche, Krishna Prasad Shrestha, Sven Eckart, Fabian Mauss, and Hartmut Krause. Temperature and pressure dependency of the burning velocity in laminar

premixed methanol and polyoxymethylene dimethyl ether (ome1, ome2, and ome3) flames. *Proceedings*, 2021.

[86] Sandra Richter, Trupti Kathrotia, Marina Braun-Unkhoff, Clemens Naumann, and Markus Köhler. Study on the influence of oxymethylene ethers (omen) blending a diesel surrogate. In *Proceedings*, 2021.

[87] RD Cook, DF Davidson, and RK Hanson. Shock tube measurements of ignition delay times and oh time-histories in dimethyl ether oxidation. *Proceedings of the Combustion Institute*, 32(1):189–196, 2009.

[88] Chenglong Tang, Liangjie Wei, Jiaxiang Zhang, Xingjia Man, and Zuohua Huang. Shock tube measurements and kinetic investigation on the ignition delay times of methane/dimethyl ether mixtures. *Energy & fuels*, 26(11):6720–6728, 2012.

[89] Robin John Varghese, V Ratna Kishore, M Akram, Y Yoon, and Sudarshan Kumar. Burning velocities of dme (dimethyl ether)-air premixed flames at elevated temperatures. *Energy*, 126:34–41, 2017.

[90] Z Zhao, A Kazakov, and FL Dryer. Measurements of dimethyl ether/air mixture burning velocities by using particle image velocimetry. *Combustion and Flame*, 139(1-2):52–60, 2004.

[91] Kai Moshammer, Ahren W Jasper, Denisia M Popolan-Vaida, Zhandong Wang, Vijai Shankar Bhavani Shankar, Lena Ruwe, Craig A Taatjes, Philippe Dagaut, and Nils Hansen. Quantification of the keto-hydroperoxide (hooch2ocho) and other elusive intermediates during low-temperature oxidation of dimethyl ether. *The Journal of Physical Chemistry A*, 120(40):7890–7901, 2016.

[92] Hao Zhang, Steffen Schmitt, Lena Ruwe, and Katharina Kohse-Höinghaus. Inhibiting and promoting effects of no on dimethyl ether and dimethoxymethane oxidation in a plug-flow reactor. *Combustion and Flame*, 224:94–107, 2021.

[93] Zhandong Wang, Xiaoyuan Zhang, Lili Xing, Lidong Zhang, Friederike Herrmann, Kai Moshammer, Fei Qi, and Katharina Kohse-Höinghaus. Experimental and kinetic modeling study of the low-and intermediate-temperature oxidation of dimethyl ether. *Combustion and Flame*, 162(4):1113–1125, 2015.

[94] Friederike Herrmann, Patrick Oßwald, and Katharina Kohse-Höinghaus. Mass spectrometric investigation of the low-temperature dimethyl ether oxidation in an atmospheric pressure laminar flow reactor. *Proceedings of the Combustion Institute*, 34(1):771–778, 2013.

[95] Huijun Guo, Wenting Sun, Francis M Haas, Tanvir Farouk, Frederick L Dryer, and Yiguang Ju. Measurements of h2o2 in low temperature dimethyl ether oxidation. *Proceedings of the Combustion Institute*, 34(1):573–581, 2013.

[96] Erjiang Hu, Zhenhua Gao, Yang Liu, Geyuan Yin, and Zuohua Huang. Experimental and modeling study on ignition delay times of dimethoxy methane/n-heptane blends. *Fuel*, 189:350–357, 2017.

[97] J Herzler, Y Sakai, M Fikri, and C Schulz. Shock-tube study of the ignition and product formation of fuel-rich ch4/air and ch4/additive/air mixtures at high pressure. *Proceedings of the Combustion Institute*, 37(4):5705–5713, 2019.

[98] Lorena Marrodán, Eduardo Royo, Ángela Millera, Rafael Bilbao, and María U Alzueta. High pressure oxidation of dimethoxymethane. *Energy & Fuels*, 29(5):3507–3517, 2015.

[99] Sven Eckart, Liming Cai, Chris Fritsche, Florian vom Lehn, Heinz Pitsch, and Hartmut Krause. Laminar burning velocities, co, and nox emissions of premixed polyoxymethylene dimethyl ether flames. *Fuel*, 293:120321, 2021.

[100] L Pratali Maffei, M Pelucchi, and T Faravelli. Lumping of the low temperature oxidation of n-pentane: application of mel. In *10th European Combustion Meeting 2021*, pages 171–176, 2021.

A | Species dictionary

Pseudospecies CHEMKIN name	Isomers description	Isomers N. in Pseudospecies
DMM	Dimetoxymethane (OME1)	1
DMM-R	DMM alkyl radicals	2
DMM-RO2	DMM peroxy radicals	2
DMM-ROOH	DMM hydroperoxides	2
DMM-RO	DMM alkoxy radicals	2
DMM-ket	DMM ketones	2
DMM-ketR	DMM ketone radicals	4
DMM-cycleth	DMM cyclic ethers	2
DMM-QOOH	DMM hydroperoxy-alkyl radicals	3
DMM-O2QOOH	DMM hydroperoxy-alkyl-peroxy radicals	3
DMM-OQOOH	DMM keto-hydroperoxide	3
CH3OCOOH	DME carboxylic acid	1
DMM-R2OOH	DMM dihydroperoxyl-alkyl radicals	2
DMM-ketRO	DMM keto-alkoxy radicals	2
DMM-cyclethOOH	DMM hydroperoxy cyclic ether	2
CH2OCHO	DME ketone radical	1
OME2	Oxymethilene ether 2	1
OME2-R	OME2 alkyl radicals	2
OME2-RO2	OME2 peroxy radicals	2
OME2-RO	OME2 alkoxy radicals	2
OME2-QOOH	OME2 hydroperoxy-alkyl radicals	5
OME2-ROOH	OME2 hydroperoxides	2
OME2-cycleth	OME2 cyclic ethers	3
OME2-O2QOOH	OME2 hydroperoxy-alkyl-peroxy radicals	5
OME2-OQOOH	OME2 keto-hydroperoxide	5
CH3OCH2OCOO	DMM keto-alkoxy radical	1

Pseudospecies CHEMKIN name	Isomers description	Isomers N. in Pseudospecies
OME3	Oxymethilene ether 3	1
OME3-R	OME3 alkyl radicals	3
OME3-RO2	OME3 peroxy radicals	3
OME3-RO	OME3 alkoxy radicals	3
OME3-QOOH	OME3 hydroperoxy-alkyl radicals	7
OME3-ROOH	OME3 hydroperoxides	3
OME3-cycleth	OME3 cyclic ethers	5
OME3-O2QOOH	OME3 hydroperoxy-alkyl-peroxy radicals	7
OME3-OQOOH	OME3 keto-hydroperoxide	7
OME2-ketRO	OME2 keto-alkoxy radicals	2
CH3OCH2OCH2OCHO	OME2 ketone	1
OME2-ketR	OME2 ketone radicals	2
OME4	Oxymethilene ether 4	1
OME4-R	OME4 alkyl radicals	3
OME4-RO2	OME4 peroxy radicals	3
OME4-RO	OME4 alkoxy radicals	3
OME4-QOOH	OME4 hydroperoxy-alkyl radicals	9
OME4-ROOH	OME4 hydroperoxides	3
OME4-cycleth	OME4 cyclic ethers	5
OME4-O2QOOH	OME4 hydroperoxy-alkyl-peroxy radicals	9
OME4-OQOOH	OME4 keto-hydroperoxide	9
OME3-ketRO	OME3 keto-alkoxy radicals	2
OME3-ketR	OME3 ketone radicals	2
C4H9O4CHO	OME3 ketone	1

B | Optimized reactions

Listed parameters refer to the modified Arrhenius equation $k = AT^{\beta}e^{-\frac{E_a}{RT}}$. Units are cm, cal, mol, K. For each reaction, the former set of parameters is the nominal one from the lumped mechanism, the latter is the optimized one.

Reaction	A	β	E_a
HO2+DMM⇒H2O+DMM-R	3.690E-02	3.480	11741
	1.987E-02	3.496	11463
H+DMM⇒H2+DMM-R	1.300E+03	2.440	4826
	2.594E+03	2.489	4920
OH+DMM⇒H2O+DMM-R	8.520E-01	3.210	-1861
	6.732E-01	3.182	-1673
HO2+DMM-RO2⇒O2+DMM-ROOH	1.520E-02	2.100	-11473
	1.100E-02	2.020	-11410
2DMM-RO2⇒O2+2DMM-RO	1.547E+20	-4.500	0
	1.299E+20	-4.459	-238
DMM-RO⇒CH2O+CH3OCH2O	1.050E+19	-1.740	17622
	1.254E+19	-1.791	17769
DMM-RO⇒H+DMM-ket	3.230E+13	0.010	26133
	4.089E+13	-0.003	25868
DMM-ket⇒CH3+OCH2OCHO	9.680E-21	10.370	55182
	1.048E-20	10.480	55122
DMM-ket⇒CH3O+CH2OCHO	1.240E+72	-15.550	120140
	1.131E+72	-15.661	120194
DMM-OQOOH⇒OH+DMM-ketRO	1.970E+16	0.000	41997
	1.083E+16	-0.005	41772
O2+OME2⇒HO2+OME2-R	5.350E+04	2.080	40249
	6.403E+04	2.118	40517
HO2+OME2⇒H2O2+OME2-R	4.790E-01	3.380	11703
	4.594E-01	3.327	11658

Reaction	A	β	E_a
OH+OME2⇒H2O+OME2-R	2.910E-01	3.330	-2003
	2.497E-01	3.367	-1724
OME2-R⇒CH2O+DMM-R	2.670E+35	-6.830	33770
	1.338E+35	-6.802	33868
OME2-R⇒CH3+DMM-ket	3.190E+15	-1.820	11633
	2.157E+15	-1.823	11714
O2+OME2-R⇒OME2-RO2	2.570E+19	-3.210	3620
	1.775E+19	-3.203	3422
OME2-RO2⇒OME2-QOOH	6.260E+06	1.300	12840
	4.641E+06	1.332	12839
OME2-QOOH⇒OME2-RO2	1.560E+11	-0.450	1062
	1.418E+11	-0.472	1154
OME2-QOOH⇒OH+OME2-cycleth	5.360E+13	-0.630	16588
	3.194E+13	-0.633	16524
OME2-QOOH⇒OH+CH2O+DMM-ket	2.289E+12	0.144	19398
	2.139E+12	0.156	19529
OME2-QOOH⇒OH+2CH3OCHO	1.678E+08	0.897	16081
	1.883E+08	0.900	15856
O2+OME2-QOOH⇒OME2-O2QOOH	4.320E+14	-1.730	2184
	2.934E+14	-1.732	1772
OME2-O2QOOH⇒OH+OME2-OQOOH	3.610E+09	0.700	18147
	2.672E+09	0.698	18158
HO2+OME3⇒H2O2+OME3-R	9.690E-01	3.330	11704
	1.077E+00	3.251	11664
OH+OME3⇒H2O+OME3-R	5.200E-01	3.270	-1926
	3.068E-01	3.257	-1702
OME3-R⇒CH3+CH3OCH2OCH2OCHO	1.570E-05	3.900	553
	1.214E-05	3.905	515
OME3-R⇒CH2O+OME2-R	4.310E+34	-6.640	33112
	4.637E+34	-6.628	33219
OME3-R⇒CH3OCH2+DMM-ket	1.400E+41	-8.580	39092
	7.017E+40	-8.600	38946
O2+OME3-R⇒OME3-RO2	6.250E+19	-3.280	4089
	5.560E+19	-3.266	4163

Reaction	A	β	E_a
OME3-RO2⇒OME3-QOOH	1.080E+07	1.270	13092
	1.713E+07	1.215	13063
OME3-QOOH⇒OME3-RO2	1.900E+06	0.950	-1670
	2.220E+06	0.961	-1941
OME3-QOOH⇒OH+OME3-cycleth	2.130E+12	-0.240	15688
	1.810E+12	-0.241	16100
OME3-QOOH⇒OH+CH2O+CH3OCH2OCH2OCHO	2.443E+09	0.918	17392
	2.688E+09	0.848	17391
OME3-QOOH⇒OH+CH3OCHO+DMM-ket	1.076E+12	0.147	20149
	1.285E+12	0.121	20230
O2+OME3-QOOH⇒OME3-O2QOOH	2.140E+16	-2.120	3792
	2.113E+16	-2.186	3734
O2+OME4⇒HO2+OME4-R	1.430E+05	2.040	40293
	1.420E+05	2.052	40413
HO2+OME4⇒H2O2+OME4-R	1.570E+00	3.290	11710
	1.063E+00	3.253	11897
CH3O2+OME4⇒CH3O2H+OME4-R	2.440E-02	3.580	11887
	1.950E-02	3.581	11613
CH3+OME4⇒CH4+OME4-R	7.340E-01	3.270	7840
	1.170E+00	3.264	8155
OH+OME4⇒H2O+OME4-R	8.220E-01	3.220	-1870
	8.081E-01	3.184	-1525
OME4-R⇒CH3OCH2+CH3OCH2OCH2OCHO	1.270E+41	-8.620	38058
	1.230E+41	-8.561	38469
OME4-R⇒DMM-R+DMM-ket	1.270E+41	-8.620	38058
	2.534E+41	-8.590	37978
OME4-R⇒CH3+C4H9O4CHO	2.610E-07	4.450	-51
	2.812E-07	4.446	-135
OME4-R⇒CH2O+OME3-R	1.160E+34	-6.470	32929
	1.155E+34	-6.497	32811
O2+OME4-R⇒OME4-RO2	1.790E+20	-3.410	4254
	1.482E+20	-3.367	4665
OME4-RO2⇒O2+OME4-R	8.830E+26	-3.930	39822
	4.937E+26	-3.923	39916

Reaction		A	β	E_a
OME4-RO2⇒OME4-QOOH		3.710E+07	1.100	13195
		3.492E+07	1.188	13184
OME4-QOOH⇒OME4-RO2		5.720E+10	-0.440	23
		9.760E+10	-0.417	-219
OME4-QOOH⇒OH+OME4-cycleth		5.980E+14	-0.970	16804
		6.575E+14	-0.959	16988
OME4-QOOH⇒OH+2DMM-ket		1.799E+20	-2.385	24028
		1.439E+20	-2.364	23957
OME4-QOOH⇒OH+CH2O+C4H9O4CHO		5.881E+09	0.777	17538
		7.745E+09	0.841	17595
O2+OME4-QOOH⇒OME4-O2QOOH		9.290E+12	-1.130	2191
		8.790E+12	-1.116	2264
DMM-RO2⇒DMM-QOOH	0.01 atm	3.98E+02	2.630	15520
		4.79E+02	2.680	15431
	1 atm	9.37E+09	0.620	20432
		1.13E+10	0.670	20344
	2 atm	4.87E+02	2.700	16379
		5.86E+02	2.750	16290
	10 atm	9.68E-01	3.470	14751
		1.16E+00	3.520	14662
	20 atm	3.49E-01	3.590	14461
		4.20E-01	3.640	14372
	100 atm	9.74E-03	4.000	13274
		1.17E-02	4.050	13185
	500 atm	9.12E-02	3.700	13539
		1.10E-01	3.750	13450
DMM-QOOH⇒DMM-RO2	0.01 atm	1.32E+23	-3.760	13271
		1.15E+23	-3.740	13369
	1 atm	1.09E+23	-3.740	13200
		9.53E+22	-3.720	13299
	2 atm	1.48E+23	-3.780	13252
		1.29E+23	-3.760	13350
	10 atm	3.05E+23	-3.880	13325
		2.67E+23	-3.860	13423

Reaction		A	β	E_a
DMM-QOOH⇒DMM-RO2	20 atm	7.79E+23	-4.000	13491
		6.81E+23	-3.980	13590
	100 atm	3.19E+24	-4.200	13668
		2.79E+24	-4.180	13766
	500 atm	4.80E+24	-4.270	13660
		4.20E+24	-4.250	13758
O2+DMM-QOOH⇒DMM-O2QOOH	0.01 atm	1.93E+27	-5.560	1138
		9.67E+26	-5.570	967
	1 atm	6.66E+30	-5.770	8549
		3.34E+30	-5.780	8377
	2 atm	3.73E+23	-3.560	5543
		1.87E+23	-3.570	5372
	10 atm	4.83E+12	-0.320	430
		2.42E+12	-0.330	258
	20 atm	4.79E+12	-0.320	428
		2.40E+12	-0.330	256
	100 atm	4.71E+12	-0.320	426
		2.36E+12	-0.330	255
DMM-QOOH⇒OH+CH2O+CH3OCHO	0.01 atm	5.73E+17	-1.810	18601
		8.65E+17	-1.740	18692
	1 atm	2.84E+18	-2.020	18933
		4.28E+18	-1.950	19024
	2 atm	3.98E+16	-1.480	17955
		6.00E+16	-1.410	18047
	10 atm	3.69E+21	-2.910	20605
		5.57E+21	-2.840	20696
	20 atm	3.69E+22	-3.190	21168
		5.57E+22	-3.120	21260
	100 atm	2.08E+21	-2.840	20481
		3.14E+21	-2.770	20572
	500 atm	2.63E+21	-2.870	20538
		3.97E+21	-2.800	20629

Reaction		A	β	E_a
DMM-QOOH⇒OH+DMM-cycleth	0.01 atm	6.60E+26	-4.190	27216
		4.86E+26	-4.170	27087
	1 atm	1.98E+26	-4.040	26932
		1.46E+26	-4.020	26804
	2 atm	6.15E+26	-4.180	27190
		4.53E+26	-4.160	27062
	10 atm	7.26E+23	-3.340	25605
		5.35E+23	-3.320	25477
	20 atm	7.89E+24	-3.640	26136
		5.81E+24	-3.620	26008
	100 atm	2.37E+24	-3.500	25816
		1.75E+24	-3.480	25687
	500 atm	4.56E+23	-3.300	25404
		3.36E+23	-3.280	25275